NASA/TM—2014-218862

Acoustic Measurements from Wind Tunnel Test of AMELIA - Advanced Model for Extreme Lift and Improved Aeroacoustics

Nathan J. Burnside
Ames Research Center, Moffett Field, California

William C Horne
Ames Research Center, Moffett Field, California

Robert K Fong
Ames Research Center, Moffett Field, California

October 2014

NASA STI Program ... in Profile

Since its founding, NASA has been dedicated to the advancement of aeronautics and space science. The NASA scientific and technical information (STI) program plays a key part in helping NASA maintain this important role.

The NASA STI program operates under the auspices of the Agency Chief Information Officer. It collects, organizes, provides for archiving, and disseminates NASA's STI. The NASA STI program provides access to the NTRS Registered and its public interface, the NASA Technical Reports Server, thus providing one of the largest collections of aeronautical and space science STI in the world. Results are published in both non-NASA channels and by NASA in the NASA STI Report Series, which includes the following report types:

- TECHNICAL PUBLICATION. Reports of completed research or a major significant phase of research that present the results of NASA Programs and include extensive data or theoretical analysis. Includes compilations of significant scientific and technical data and information deemed to be of continuing reference value. NASA counterpart of peer-reviewed formal professional papers but has less stringent limitations on manuscript length and extent of graphic presentations.

- TECHNICAL MEMORANDUM. Scientific and technical findings that are preliminary or of specialized interest, e.g., quick release reports, working papers, and bibliographies that contain minimal annotation. Does not contain extensive analysis.

- CONTRACTOR REPORT. Scientific and technical findings by NASA-sponsored contractors and grantees.

- CONFERENCE PUBLICATION. Collected papers from scientific and technical conferences, symposia, seminars, or other meetings sponsored or co-sponsored by NASA.

- SPECIAL PUBLICATION. Scientific, technical, or historical information from NASA programs, projects, and missions, often concerned with subjects having substantial public interest.

- TECHNICAL TRANSLATION. English-language translations of foreign scientific and technical material pertinent to NASA's mission.

Specialized services also include organizing and publishing research results, distributing specialized research announcements and feeds, providing information desk and personal search support, and enabling data exchange services.

For more information about the NASA STI program, see the following:

- Access the NASA STI program home page at http://www.sti.nasa.gov

- E-mail your question to help@sti.nasa.gov

- Phone the NASA STI Information Desk at 757-864-9658

- Write to:
  NASA STI Information Desk
  Mail Stop 148
  NASA Langley Research Center
  Hampton, VA 23681-2199

NASA/TM—2014–218862

Acoustic Measurements from Wind Tunnel Test of AMELIA - Advanced Model for Extreme Lift and Improved Aeroacoustics

Nathan J. Burnside
Ames Research Center, Moffett Field, California

William C. Horne
Ames Research Center, Moffett Field, California

Robert K Fong
Ames Research Center, Moffett Field, California

Prepared for
NASA Subsonic Fixed Wing Program

National Aeronautics and
Space Administration

Ames Research Center
Moffett Field, CA 94035-1000

October 2014

Acknowledgments

The AMELIA CESTOL aerodynamic research program was funded by a NASA Research Announcement (NRA) award to California Polytechnic State University, San Luis Obispo (Cal Poly SLO) and Georgia Tech Research Institute. The acoustic measurement program was funded separately by NASA Aeronautics Research Mission Directorate (ARMD) Fixed Wing Project. The authors gratefully acknowledge support from NASA Langley Research Center, and the Arnold Engineering Development Center (AEDC) National Full-Scale Aerodynamics Complex (NFAC) at Ames Research Center.

Cal Poly SLO: Dr. David Marshall, Principal Investigator, Dr. Tina Jameson, Principal Researcher, Eric Paciano, Jonathan Lichwardt, Georgia Tech: Dr. Robert Englar, Dr. Richard Gaeta, Dr. Donald Nance, NASA ARMD Fixed Wing Project, Ruben Del Rosario, Dr. Michael Rogers, Craig Hange, NASA Langley Research Center: Dr. Gregory Jones, Dr. Casey Burley, AEDC NFAC: Joseph Sacco, Charles Rogers, Christopher Hartley, Aerospace Computing, Inc: Robert Mosher.

Available from:

NASA Center for AeroSpace Information
7115 Standard Drive
Hanover, MD 21076-1320
443-757-5802

This report is also available in electronic form at

http://

Nomenclature

α	Angle of attack, degrees
AoA	Angle of attack, degrees
$C\mu$ =	Slot momentum coefficient, $m*V_j$ / (q*S)
CCW	Circulation Control Wing
CFD	Computational Fluid Dynamics
Δf	Frequency resolution (Hz)
H_{FF}	Freefield microphone correction
LE	Leading Edge
m =	Slot mass flow, lb_m/s
M	Mach number
Phi	Angular coordinate describing the longitude of the noise source, degrees
R	Propagation distance from model acoustic center to microphone, degrees
q =	Freestream dynamic pressure, psf
Rho	Propagation path from noise source to sensor, inches
S =	Wing planform reference area, ft^2
TE	Trailing Edge
Theta	Angular coordinate describing the total emission angle, degrees
TPS	Thrust Propulsion Simulator
V_j =	Slot jet velocity, ft/s
Θ	Emission angle relative to model acoustic center, degrees
Θ'	Convected emission angle relative to model acoustic center, degrees

Acoustic Measurements from Wind Tunnel test of AMELIA - Advanced Model for Extreme Lift and Improved Aeroacoustics

Nathan J. Burnside, W. Clifton Horne, and Robert K. Fong

NASA Ames Research Center

Summary

A wind tunnel test has been conducted to measure the aerodynamic and acoustic performance of an active circulation-control aircraft with leading- and trailing- edge slot blowing. The 11% Advanced Model for Extreme Lift and Improved Aeroacoustics (AMELIA) model was tested in the Arnold Engineering Development Center (AEDC) National Full Scale Aerodynamics Complex (NFAC) 40- by 80-Ft wind tunnel. Forward velocities ranged from 0 to Mach 0.15 and total slot mass-flow was varied from 0 to 2.8 lb_m/sec. Angle-of-attack and sideslip ranges were -5º to 25º and -10º to 10º, respectively.

This reports summarizes acoustic measurements from the wind tunnel test and the corrections applied to the released acoustic data. The analysis focuses on measurements for the clean wing configuration (turbine propulsion simulators removed) with trailing- and leading-edge slot blowing and with trailing-edge blowing, for systematic variations in slot mass flow from nearly zero to the system maximum. The acoustic measurements from a fixed phased microphone array and seven fixed microphones were corrected for sensor directional response and atmospheric attenuation. Graphs of 1/3-octave spectra, narrowband spectra, and directional variations in OASPL are presented for each active lift configuration. This report is intended to document the corresponding set of corrected data that is now available for development and verification of new predictive models of the active lift source.

For large slot mass flow conditions 1/3-octave spectral shapes were level and flat, typical of a pink noise source. Little source directivity was present in the OASPL levels for the 0º flap conditions and show only a slight downstream increase with the 60º flap configuration. For moderate to high slot mass flow conditions trailing-edge only blowing spectra were similar to leading- and trailing edge blowing cases. However for the lower mass flows variations of as much as 5 dB were observed.

Introduction

A wind tunnel test has been conducted to measure the aerodynamic and acoustic performance of an active circulation-control aircraft with leading- and trailing- edge slot blowing. The 11% model was tested in the Arnold Engineering Development Center (AEDC) National Full Scale Aerodynamics Complex (NFAC) 40- by 80-Ft wind tunnel. Forward velocities ranged from 0 to Mach 0.15 and total slot mass-flow was varied from 0 to 2.8 lb_m/sec. Angle-of-attack and sideslip ranges were -5º to 25º and -10º to 10º, respectively. This report will focus on a subset of the acoustic results that are relevant to future computational aeroacoustic work.

Background

Active circulation control has been applied to maintain lift at reduced flight speed for short takeoffs and landings, as well as to reduce the size and weight of control surfaces. The AMELIA CESTOL active-lift aircraft configuration was developed as the result of a NASA Research Announcement (NRA) collaboration between NASA, California Polytechnic University San Luis Obispo, and Georgia Tech Research Institute. The goal of this effort was to improve the ability to design and understand the performance of a modern aircraft with leading- and trailing-edge circulation control wing and other features such as above-wing propulsion to reduce community noise. The project culminated with a comparative assessment of CFD modeling of the complex vehicle aerodynamics with extensive aerodynamic and acoustic measurements of a sting-mounted , 11% scale-model in the NFAC.

The active circulation control wing for the full-span AMELIA design evolved from studies of a constant chord configuration with dual-radius trailing edge flap by Englar and Gaeta that maintained aerodynamic performance for both cruise and landing/take-off configurations (2009). For the AMELIA model, noise considerations were also addressed in selection of characteristics such as the placement of the engines as well as slot-flow parameters such as slot exit velocity, as discussed by Jameson et al (2011).

Preliminary acoustic data from this test was reported by Burnside and Horne that clearly showed the noise signatures of the active leading- and trailing-edge blown slots, as well as the effect of the wing in shielding noise from the above-wing turbine propulsion simulators (2012 and 2013). Directional acoustic characteristics of the three-dimensional AMELIA active wing were found to be quite different from those from a constant-chord model studied by Gaeta, et al (2009). In particular, the constant chord wing model with trailing edge blowing exhibited a cardioid pattern of noise directivity with the direction of minimum emission aligned with the chord line of the flap, similar to airfoil trailing edge noise. This feature was absent in the AMELIA wind tunnel measurements at approximately 7.5 m measurement distance, but present in closer measurements (~1.5m) during static testing in a lab to optimize the internal slot flow path, Horne and Burnside (2013). This result is not unexpected, and it is likely that noise scaling laws discussed by Gaeta can still be applied to the three dimensional AMELIA model for high-level estimates of vehicle noise (2010).

Objectives of this Report

This report will focus on the corrected results for selected conditions to enable the development of predictive models of the active flow leading- and trailing-edge acoustic sources. Correction methods for phased arrays and single microphone measurements are presented.

The TPS units were selected to simulate propulsion aerodynamic effects rather than propulsive acoustic effects. Some propulsive acoustic shielding effects for the CESTOL model were noted previously by Burnside and Horne, but will not be addressed in this report (2012). Only results from the "clean-wing" configurations with TPS units removed will be presented here and included in the accompanying set of data. Shielding effects of realistic above-wing propulsive sources were reported by Doty, et al for the Hybrid Wing Body Configuration (2014). Mass-flow sweeps of the circulation control provide the most probable or realistic results of a circulation-control wing, so focus will be placed on the $C\mu$ sweeps.

Test Set-up

An extensive discussion of the facility, model, test matrix, and aerodynamic results can be found in Fong et al. (2014). A brief description of the testing facility and model are included in the following sections to aid in discussion of the acoustic results.

Model Description

The AMELIA model was designed to validate predictive codes developed for powered-lift. It is an 11% scale-model of a 100 passenger, regional, cruise-efficient short take-off and landing airliner with a hybrid blended wing-body planform with circulation control wing (CCW) as discussed by Jameson et al. (2011). The model was sting mounted and included two independent high-pressure air flow-paths for the CCW and TPS units. The TPS flow path was routed through a 6-component flow-through balance and the CCW air was routed through a bellows configuration as shown in Figure 1.

Circulation control consisted of wing leading- and trailing-edge blowing over 95% of the wing span. Prior to installation, a detailed calibration of the slot was performed by Cal Poly researchers to balance the four CCW plenums, ensuring uniform slot flow at a maximum flow rate of 1.4 lb_m/s from each wing. Slot height increased from wing root to tip, however an average slot height of approximately 0.025 in. was used for the leading-edge inboard and outboard wing sections. Figure 2 shows a cross section of the wing including plenums and slots. Average heights of 0.025 in. and 0.047 in. were used for trailing-edge outboard and inboard sections, respectively. Table 1 lists the minimum, maximum, and average slot heights for all 8 wing-sections. The majority of test was conducted with CCW active on both leading and trailing edges of the wing, however a subset of data was collected with trailing edge only CCW.

Table 1. Circulation control slot heights for each of the 8 wing slot sections, measurements are in mils (1 mil = 0.001 inches).

	Left Wing			Right Wing		
	average	min	max	average	min	max
Leading Edge Inboard	24.46	15.78	30.8	26.43	19.98	32.25
Leading Edge Outboard	24.39	15	36.25	23.44	13.5	35.45
Trailing Edge Inboard	47.05	37.01	53.75	27.81	37.05	56.55
Trailing Edge Outboard	24.53	15.56	46.55	23.68	15.35	37.9

Two TPS units built by Tech Development Inc. (TDI) were mounted in engine nacelle pods above the fuselage. The 2-stage TDI 441 TPS units were borrowed from NASA Langley and refurbished by TDI for this test. They were run at a nominal speed of 33,400 RPM, about 77% of their designed maximum. The TPS units had a fan diameter of 5 inches (12.7 cm), with 2 stages, and a 3-stage air motor drive. TPS elevation above the wing surface was varied during the test; elevations of 0.84 and 1.25 fan diameters above the model center, referred to as low- and high-pylon elevations respectively. As stated in the objectives section this report will focus on the conditions with the TPS units removed.

Coordinate Systems and the Acoustic Center

Corrections to single microphone and array data require propagation distances and convected emission angles for proper application. The leading- and trailing-edge slots blowing create four distributed noise sources along the leading and trailing edges on both wings of the model in addition to any airframe noise sources. To approximate the source locations, the acoustic center was created as the approximate geometrical center of multiple noise sources. Figure 3 shows the test section layout and the acoustic center. It is easy to see that the acoustic center moves with the model and convected angles will be dependent on freestream conditions. Figure 4 shows the exact placement of the acoustic center on a planform drawing of the model, when looking down. The acoustic center is a good geometrical mean of the trailing edge slots but is not as good for the leading edge slots. The center was chosen not as an exact geometrical center but rather because it the midpoint between sweep change on the trailing edges, a point that is visibly identifiable in photographs.

Model attitude and sideslip changes create distinct propagation distances and emission angles for each of the microphones and the phased microphone array. A spherical coordinate system centered at the model acoustic center makes data correction straightforward. Figure 5 shows the spherical coordinate system defined at the model acoustic center. Rho is the propagation distance from the acoustic center to each of the sensors and theta is the non-convected emission angle from the acoustic source to the sensors. Upstream radiation corresponds to 0º and downstream radiation corresponds to 180º in theta. Phi of 0º points down while 90º points out of the left wing. Appendix A lists the spherical coordinates for every angle-of-attack and sideslip condition tested. Emission angles in the report are convected incorporating downstream drift due to the freestream velocity.

Facility Description

The NFAC facility at NASA Ames Research Center is currently leased and operated by Arnold Engineering Development Complex (AEDC) as shown in Figure 6. The 40- by 80-Foot Wind Tunnel (40x80) is a closed-circuit wind tunnel, driven by six 40-ft-diameter, 22,550-hp fans. The test section walls are semi-circular with a flat floor and ceiling. The test section is nominally 40 ft high, 80 ft wide, and 80 ft long. An 8:1 contraction accelerates flow and helps to reduce nonuniformity and turbulence (0.5% stream-wise, 0.7% cross-stream). The atmospheric wind tunnel has a maximum test-section velocity of 300 knots (M=0.45).

The test section of the 40x80 is acoustically treated to minimize reverberation. A porous liner and perforated metal sheet form an aerodynamic surface that covers 42-inch-deep sound absorbing fiberglass wedges. Figure 7 shows the details of the acoustic lining. The acoustic lining absorbs 94% to 97% of the acoustic energy between 100 Hz to 2,500 Hz and 78% to 97% between 4 kHz to 20 kHz as reported by Soderman et al. (2002). Allen, Jaeger, and Soderman reported measurements of the test section background noise using in-flow sensors (2003).

Instrumentation and Data Acquisition System

Acoustic instrumentation included fixed microphones, a phased microphone-array, and surface-mounted unsteady pressure sensors. All microphones were G.R.A.S. 40BF, ¼" free-field condenser type. The unsteady pressure measurements were made using a mix of 5 psi and 15 psi Kulite transducers type XCS-062. All acoustic signals were acquired simultaneously using a National Instruments 24-bit PXI data system. Data were sampled at 102.4 kHz yielding a 40 kHz bandwidth.

Eight unsteady surface pressure transducers were mounted on the model at locations near the TPS nacelle and along the mid-fuselage as shown in Figure 8. Seven fixed microphones were installed outboard of the left wing and a phased microphone array was placed outboard of the right wing as shown in Figure 3.

The microphones were staggered so that their turbulence wakes would not impinge on downstream microphones. Each microphone was mounted in stream-wise aerodynamic holder with a G.R.A.S. RA0022 nosecone as shown in Figure 9. The microphone assembly was mounted atop a McMasters-Henderson airfoil shaped strut, which has be shown to not generate vortex tones (McMasters et al. 1981).

The 48-channel, 40-inch diameter array was mounted in an aerodynamic fairing and recessed behind a porous Kevlar screen (Horne et al 2004). The array pattern and processing software were purchased from Optinav, Inc. High-resolution photos for array beamforming were taken with a Canon 5d II camera mounted at the array center during the model wind off weight tares.

Data Processing

Single Microphone

A series of corrections are applied to the single microphone data to remove test day and microphone effects. All corrections were applied in post processing.

Convection Effect

As sound travels from source to receiver in a moving fluid medium, its emission angle and propagation path are altered. Convected emission angle Θ' and convected propagation path R' are used to account for the moving fluid media. Soderman and Allen discuss at depth how to account for convection effects (2002):

$$\Theta' = \cos^{-1}\left[M\sin^2\Theta + \cos\Theta\sqrt{1-M^2\sin^2\Theta}\right], \qquad (1)$$

where Θ is the geometric angle from source to receiver and M is the Mach number of the flow. R' is the convected propagation distance and is calculated as:

$$R' = \frac{R}{-M\cos\Theta + \sqrt{1-M^2\sin^2\Theta}}, \qquad (2)$$

where R is the geometric propagation path from source to receiver.

Nosecone Directional Effect

Microphone forebodies or nosecones are necessary to prevent direct flow impingement on the diaphragm, however their presence influences the measured pressure fluctuations. A wind-off calibration of nosecone directional effects over the full range of emission angles was conducted in the AOX anechoic chamber. The free-field microphones are designed to produce an accurate measurement of fluctuating pressure when mounted in the freefield with a 0º incidence. The microphone and nosecone pair was used to measure the sound pressure levels of a steady pink-noise source at incidence angles ranging from -180º to 180º. Frequency and incident angle dependent corrections were then calculated using the measured sound pressure levels of the same source and microphone with no nosecone at a 0º incidence. Figure 10 shows a surface plot of the corrections for incident angles of 0º to 180º, the corrections are symmetric for -180º to 0º. Note that the corrections are added to the measure data and that the corrections are referenced to incident angles not emission angles. Samples of typical corrections are shown in Figure 11.

Nosecone Velocity Effect

To quantify the effect of forward velocity the G.R.A.S. nosecones were calibrated in the AOX anechoic chamber wind tunnel. A 4" nozzle extends from the wall and creates an open jet wind tunnel across the short dimension of the chamber. A speaker source with pink noise was placed outside the jet stream. Figure 12 and Figure 13 show that below 40 kHz the corrections are negligible for M = 0.128 and are less then 2 dB for M = 0.185. The majority of this test was run at M = 0.06 and the maximum Mach number was 0.15. Because the corrections are negligible for the data of interest, nosecone velocity corrections are not applied to the data. In the accompanying data sets, atmospheric absorption levels were calculated for Doppler-shifted frequencies as discussed by Soderman and Allen (2002).

Atmospheric Absorption

Frequency dependent atmospheric attenuation is calculated for each condition and microphone using commonly accepted methods (Bass et al. 1995 and 1996). Propagation distance is calculated using the acoustic center and the model attitude and sideslip conditions. Figure 14 shows a typical set of atmospheric corrections for the seven single microphones. Notice that the corrections are unique to each microphone because of convected propagation distances.

Comment on Reflections

The depth of the wind tunnel acoustic liner is 42 inches over most of the test section, but is shallower (to a minimum of 6") over some portions of the test section floor. The seven microphones are subject to floor reflections at low tunnel speeds for which the direct and reflected signal emission angles are comparable. At higher tunnel speeds, the direct and reflected emission angles are less correlated. This effect can be seen in Figure 15 as low frequency scalloping of the microphone spectra by about +/-5 dB for maximum slot blowing condition at 0 kts (Run 268). The reflection effects taper off for higher tunnel speeds of 40 and 60 kts as seen in Figure 16 and Figure 17, respectively. Reflection effects were not anticipated for the phased microphone array since the orientation of the array fairing 15˚ from horizontal helped to block the reflected signal.

Correction for Noise Level

For combinations of higher wind tunnel speed and low CCW mass flow, he CCW slot noise was close to or lower than the microphone background noise level. The graphical plots and accompanying data sets of this report were not corrected for background noise effects. For measured levels close to the background levels, typical corrections are provided in the following table:

Table 2. Typical corrections for background noise.

(Signal + noise) - noise	Correction: signal – (signal + noise)
1.8	-4.8
3	-3
4.8	-1.8
7.8	-.8

For example, if the measured signal is 3 dB above the background, then subtract 3 dB from the measured signal to estimate the signal level with noise removed.

Phased Microphone Array

Microphone Freefield Response Effect

The G.R.A.S. 40BF freefield microphones used in the array do not measure a true pressure field when placed into a flat plate. The diaphragms are designed to have a lower pressure response as frequency increases to minimize the effects of microphone on the measured pressure field. When placed in a flat plate this response is not needed because the plate creates a pressure field doubling resulting in a uniform 6 dB increase in amplitude. The microphone freefield response, H_{FF} is approximated using a 9th order polynomial cure fit of the measured response and was used to remove the freefield response:

$$\begin{aligned} H_{FF}(f) &= 0.46888 - (1.3249\times10^{-4})f \\ &+(2.8876\times10^{-6})f^2 - (9.0321\times10^{-13})f^3 \\ &+(1.2855\times10^{-17})f^4 - (1.0181\times10^{-22})f^5 \\ &+(4.8886\times10^{-28})f^6 - (1.4977\times10^{-33})f^7 \\ &+(2.9289\times10^{-39})f^8 - (2.9285\times10^{-45})f^9, \end{aligned} \tag{3}$$

where *f* is frequency.

Kevlar Directional Effect

The Kevlar screen used to suppress the boundary layer noise over the face of the array increases the signal-to-noise ratio significantly, however is also affects the measured data and corrections are needed. An in-situ calibration was performed in the 40x80 using the phased array and a mobile broadband speaker source. The array was tilted so that the its normal vector was parallel with the floor and a speaker source was moved on a constant arc in 15º steps. The test was repeated with the Kevlar screen removed to develop a calibration. Figure 18 shows the frequency and incident dependent results. For emission angles of interest in this study, the correction varied between a minimum of -1.5 dB to a maximum of +5 dB. As with all corrections presented in this report the correction is added to the data.

Array Correction Summary

In addition to the freefield response and Kelvar effects, the array data were corrected for atmospheric attenuation and pressure doubling. The atmospheric attenuation corrections were calculated using Equation 1 and Equation 2 and applied the same way as the microphone corrections. Microphone installation in a flat plate creates a nominal 6 dB pressure doubling that was subtracted from the data. Kevlar and atmospheric corrections are freestream condition dependent and are calculated using the acoustic center. Typical array corrections are shown in Figure 19.

As with the single microphones, the array levels were not corrected for background noise levels. With conventional (delay-and-sum) beamforming method used in this study, the in-flow array provides about 10 dB suppression of background noise relative to a single in-flow microphone with nosecone since the noise from the turbulent boundary layer near the sensors is associated with subsonically convecting boundary layer disturbances. These disturbances are far less coherent between the array microphones than the incident sound waves from the test model. Further suppression of up to 20 dB of noise from the wind tunnel fan drive and model support hardware was achieved by subtracting the array cross-spectral matrix (CSM) of the test model with CCW blowing off from conditions with CCW active during the same test run, as described by Horne and Burnside (2013). Comparisons between levels measured with the microphone array using the CSM background subtraction method and a comparable single microphone are presented in the following section.

Comparison of Results from the Microphone Array and Single Microphone

A single phased microphone array was used to provide information on the location of CCW acoustic sources, and to provide significant suppression of background noise for measurement of low-level sources at the higher wind tunnel speeds. The wind tunnel schedule precluded additional time needed for traversing either the array or the single strut mounted microphones, so directivity information was obtained from the seven fixed microphones. The emission angle for the array was comparable to that for the 6th microphone and comparison of levels measured by these two sensors is presented below.

Comparisons between microphone measurements and phased array peak levels for a hemispherically processed scan grid are good for 60º flaps cases but not as good for the 0º flap configuration. Figure 20 to Figure 23 compare array and microphone measurements for velocities ranging from 0 to 100 knots. For each comparison the microphone with the convected emission angle closest to the array convected emission angle was used. Array levels are lower by about 4 dB for the V = 0 knot case but are within 2 dB for the V = 40 and 60 knot cases. Higher microphone levels at the V = 0 case shown in Figure 20 may be attributed to reflections associated with the source directivity at this flap angle of 0º. The 100 knot case shows array levels 10 dB below the single microphone, however this is expected because background noise levels are approaching the slot blowing levels and the microphone measurements can not differentiate between the slot blowing and background noise.

Comparisons of the 60º flap configuration with velocities ranging from 0 knot to 100 knots are shown in Figure 24 to Figure 27. Below 10 kHz array and microphone levels compare very well for the lower three velocities. As the wind tunnel background noise increases the microphone measurements become contaminated with background noise. The 60º flap setting appears to have a favorable source directivity for these comparisons. Not shown but investigated were the 80º flap and 40 knot configuration where the data trends were similar to the 60º flap cases. It is assumed that the source directivity and reflections cause the 0º flap configuration differences.

In general, the agreement in spectral level trend with frequency is better below 10 kHz than above. Reasons for the divergence at high frequencies include the following: 1) Below 10 kHz the array resolution using conventional beamforming does not resolve individual sources and the array peak level corresponds well with the integrated level within the region of interest (ROI) containing the test model. Above this frequency, the individual CCW sources are resolved and integration of levels within the ROI should compare better with the single microphone signal. 2) At 0˚ yaw and incidence, the array solid capture angle is less than 8˚. While this is relatively small, incident sound from the distributed CCW sources may become less coherent with increasing frequency between the microphones over the array face, resulting in decreasing level as the frequency increases.

Figure 23 and Figure 27 show that at velocity of 100 knots the fixed microphones no longer measure the CCW noise but are instead overpower by the freestream background noise. Figure 28 shows that as freestream velocity increases the CCW noise remains relatively constant. This showcases the ability of the phased array with CSM background noise subtraction to measure the source of interest while rejecting the wind tunnel background noise.

The biggest utility of the array is measuring noise sources that are below the background noise. Figure 29 is a slot $C\mu$ sweep at 100 knots with leading- and trailing-edge blowing as measured by the microphone with a convected emission angle of 123º. The bunching of the lower $C\mu$ illustrates where the noise from the slot blowing exceeds the background noise of the wind tunnel. The same conditions were measured with the phased array and background noise subtraction in Figure 30 where it is evident that many more of the lower $C\mu$ conditions are measureable above the background noise. Below 20 kHz it only the two lowest conditions are grouped together.

Results

This section will present plots of the 1/3-octave and narrowband (Δf = 25 Hz) spectra, as well as directivity of the OASPL from the seven fixed microphone sensors. The 1/3-octave plots depict the sideline microphone, ie the microphone closed the the 90º convected emission angle. Selected source location images and spectra (uncorrected) from the phased microphone array were presented and discussed previously by Burnside and Horne and are not included in this report. The phased microphone array and microphone 6 were positioned close to the same unconvected emission angle (~115º at yaw = 0º); comparisons of corrected 1/3-octave spectra for selected conditions are included in previous section.

Wind tunnel steady state conditions were acquired by the facility while the dynamic acoustic data were acquired by the AOX staff. Security restrictions prevent network communication between the two data systems and as a result the NFAC run numbering system is different than the acoustic run numbering system. All run numbers presented here will be acoustic run numbers. The data set accompanying this report references only the acoustic run numbers. Run and point numbers were modified in the NFAC data to reflect the acoustic run number bookkeeping.

Data files of corrected 1/3-octave and narrowband spectra for the seven microphones and the array, as well as aerodynamic and acoustic logs of run conditions are available for further analysis of this data. The available file descriptions and formats are detailed in Appendix B.

Each mass flow sweep consisted of typically twenty sequentially increasing settings of total mass flow (plenum pressure), although the specific settings vary between configurations. File #1 (NFAC conditions) includes slot exit flow conditions for each of the eight slots (four LE, four TE). The noise scaling law for the flap trailing edge with slot blowing discussed by Gaeta is based on the velocity at the flap trailing edge (2010). This quantity was not measured directly, but may be computed with a simulation of the local flap flowfield using the nozzle exit conditions.

Airframe Noise (Clean wing, no slot blowing)

Figure 31, Figure 32, and Figure 33 show spectra from the fixed microphones for angle of attack sweeps at 40 kts for flap angles of 0º, 60º and 80º, respectively, with little variation in the spectral level over the full range of angle-of-attack.

It was possible to suppress a large portion of the background noise from the in-flow microphone array with the method of cross-spectral-matrix background noise subtraction, as discussed by Horne and Burnside (2013). This method demonstrated suppression levels of up to 20 dB by subtracting the CSM of the test configuration with zero slot blowing from comparable measurements (same α and flap angle). Systematic measurements of noise from the model support sting and strut prior to model installation were obtained for a range of representative configurations to attempt airframe noise measurements with the array, however this did not achieve usable results since significant changes to the sting support (addition of high pressure supply hoses, instrumentation cables, etc) occurred after the sting-only measurements were acquired.

Trailing-Edge Cμ Sweeps

This section presents microphone spectra (~90˚ 1/3-octave and narrowband) and OASPL directional plots for the seven microphones with only trailing-edge slow-blowing mass flow sweeps. The corresponding figures (Figure 34 to Figure 57) are organized according to Table 3 and Table 4.

Table 3. Trailing-edge only Cμ sweeps discussed for 0º angle-of-attack.

α = 0˚				
	Flap 0˚		Flap 60˚	
V (knots)	Run	Figures	Run	Figures
0	271	Fig. 34-36	239	Fig. 46-48
40	263	Fig. 37-39	244	Fig. 49-51
60	268	Fig. 40-42	249	Fig. 52-54
100	277	Fig. 43-45	255	Fig. 55-57

Table 4. Trailing-edge only Cμ sweeps discussed for 10º angle-of-attack.

α = 10˚				
	Flap 0˚		Flap 60˚	
V (knots)	Run	Figures	Run	Figures
0	273	Fig. 58-60	254	Fig. 67-69
40	265	Fig. 61-63	246	Fig. 70-72
60	270	Fig. 64-66	251	Fig. 73-75

Preliminary observations from the plots (trailing edge blowing only) include the following:

The starting and ending value for total mass flow in lbm/sec is depicted on the 1/3-octave plot for the ~90˚ microphone for each condition. Intermediate values of total and individual slot mass flows and flow coefficients Cμ can be found in the NFAC run data file #1 listed in Appendix B. For large values of slot flow, the 1/3 octave spectral shape is level and flat, typical of a pink noise source. Some spectral peaks are apparent in the narrow band plots, prominent peaks vary between 5-8 dB. For low values of slot flow more variability in the 1/3 octave and narrowband spectra are seen.

For flap angle of 0˚, the directional variations in OASPL are not large but tend to decrease for the aft angles. For flap angles of 60˚, the OASPL levels are not significant in the forward direction, but increase steadily with emission angle aft of 90˚. No relative minima in directional level are observed for any of the trailing-edge slot-flow conditions, consistent with observations of a limited set of wind tunnel conditions reported by Horne and Burnside. As noted previously, this is not surprising due to the different sweep angles of the trailing edge slot segments and the large distance of the sensors from the model.

The directional OASPL levels are not scaled for variations in sensor distance from the acoustic center, but these variations are small, as tabulated in Appendix A. For example, with an angle-of-attack and sidelslip angles of 0˚, the sensor distance varies from 336 in. for microphone 1 (upstream) to a minimum of 286 in. for microphone 4, and increasing again to 330 in. for microphone 7 (downstream). Level variations due to distance relative to microphone 4 are -1.4 dB, 0, dB, and -0.5 dB respectively.

The apparent gap in the mass flow sequence in Figure 34 and Figure 35 is not observed in other conditions resulted from a data acquisition error.

The noise floor due to wind noise over the microphone nosecone increases steadily as wind speed increases from 40 to 60 to 100 kts. Above the noise floor, the effect of wind speed on spectral shape or directivity is not dramatic.

Trailing- and Leading-Edge Cμ Sweeps

This section presents results of measurements of the model with both leading- and trailing-edge blowing in a format similar to the previous section for trailing-edge only blowing. In the aerodynamic results, Fong report that the leading edge slots were effective in postponing stall as α increased beyond the stall α of the trailing edge only blowing. For the acoustic sensor layout of this test, the leading edge slots and downstream slot flow area were shielded by the wing for the clean-wing mass flow sweep configurations reported here. Little aerodynamic difference was reported between the α = 0˚ and α = 10˚ conditions. The model configurations, run numbers and report figures for the trailing- and leading-edge slot flow sweeps are given in Table 5 and Table 6.

Table 5. Trailing- and leading-edge Cμ sweep discussed for 0º angle-of-attack.

α = 0˚						
	Flap 0˚		Flap 60˚		Flap 80˚	
V (knots)	Run	Figures	Run	Figures	Run	Figures
0	202	Fig. 76-78	178	Fig. 88-90		
40	208	Fig. 79-81	185	Fig. 91-93	227	Fig. 100-102
60	223	Fig. 82-84	196	Fig. 94-96	231	Fig 103-105
100	217	Fig. 85-87	200	Fig. 97-99	237	Fig 106-108

Table 6. Trailing- and leading-edge Cμ sweeps for 10º angle-of-attack.

α = 10˚				
	Flap 0˚		Flap 60˚	
V (knots	Run	Figures	Run	Figures
0	204	Fig. 109-111	180	Fig. 121-123
40	210	Fig. 112-114	187	Fig. 124-126
60	216	Fig. 115-117		
100	219	Fig. 118-120		

In general the trends observed in 1/3-octave and narrowband spectral shape for moderate to high levels of slot blowing are similar for the two configurations. For low- to moderate levels of blowing, however, the 1/3-octave and narrow band spectra exhibit significantly greater variation in level with frequency (+/- 5 dB) for the trailing- and leading-edge slot blowing configuration than for the trailing-edge only. It is not clear if this is due to an external aeroacoustic interaction or other mechanism from the data acquired from this test and another study may be needed to further characterize the effect.

Concluding Remarks

This reports summarizes acoustic measurements from the wind tunnel test of the 11% scale AMELIA CESTOL active lift aircraft model in the AEDC NFAC 40- by 80- Foot Wind Tunnel. The analysis focuses on measurements for the clean wing configuration (turbine propulsion simulators removed) with trailing- and leading-edge slot blowing and with trailing-edge blowing, for systematic variations in slot mass flow from nearly zero to the system maximum. The acoustic measurements from a fixed phased microphone array and seven fixed microphones were corrected for sensor directional response and atmospheric attenuation graphs of 1/3-octave spectra, narrowband spectra, and directional variations in OASPL are presented for each active lift configuration. The report is intended to document the corresponding set of corrected data that is now available for development and verification of new predictive models of the active lift source.

References

Allen, C.S., Jaeger, S.M., Soderman, P.T., “Background Noise Sources and Levels in the NASA Ames 40- by 80-Foot Wind Tunnel at the Turn of the Century: A Status Report,” NASA/TP-2003-212259, November 2003.

Bass, et al., "Journal of Acoustical Society of America", (97) pg 680, January 1995.

Bass, et al., "Journal of Acoustical Society of America", (99) pg 1259, February 1996.

Burnside, Nathan J., and Horne, William C., “Acoustic Surveys of a Scaled-Model CESTOL Transport Aircraft in Static and Forward Speed Conditions, AIAA-2012-0237 AIAA/CEAS 18th Aeroacoustics Conf., 4-6 June, 2012, Colorado Springs, CO

Doty, Michael J., Brooks, Thomas F., Burley, Casey L, Bahr, Christopher J., and Pope, Dennis S., “Jet Noise Shielding Provided by a Hybrid Wing Body Aircraft”, AIAA-2014-2625, AIAA/CEAS 20th Aeroacoustics Conference, AIAA Aviation, 16-10 June, 2014, Atlanta, GA

Englar, Robert J, Blaylock, Graham, M., Gaeta, Richard J., Jones, Gregory S., and Milholen, William E., “Recent Experimental Development of Circulation Control Airfoils and Pneumatic Powered-Lift Systems”, AIAA-2010-345, 48th AIAA Aerospace Sciences Meeting, 4-7 Jan. 2010, Orlando FL

Fong, R., et al. “Advanced Model for Extreme Lift and Improved Aeroacoustics (AMELIA)”, NASA Technical Memorandum, 2014-xxxxx.

Gaeta, Richard J., Lee, Warren, and Flick, Ashley, “Over-the-wing Lift, Engine-Airframe Integration effects on acoustic shielding”, AIAA-2009-282, 47th AIAA Aerospace Sciences Meeting, 5-8 Jan. 2009, Orlando, FL.

Gaeta, R., and Young, R., AIAA 2010-3880, “Development of a Noise Prediction Model for a Cruise Friendly Circulation Control Wing”, AIAA-2010-3880, 16th AIAA/CEAS Aeroacoustics Conf, 7-9 June, 2010m Stockholm, Sweden.

Horne, W. C., Burnside, N.J., Soderman P. T., Jaeger, S. M., Reinero, B. R., James, K. D., Arledge, T. K., “Aeroacoustic Study of a 26% Semi-span Model of a Boeing 777 Wing in the NASA Ames 40- by 80-Foot Wind Tunnel,” NASA/TP-2004-212802, October, 2004.

Horne, William C., and Burnside, Nathan J., “AMELIA CESTOL Test: Acoustic Characteristics of Circulation Control Wing and Leading- and Trailing-Edge Slot Blowing”, AIAA-2013-0978, 51st AIAA Aerospace Sciences Meeting, 07-10 Jan. 2013, Grapevine (Dallas/Ft. Worth Region), TX

Jameson, K., Marshal, D., Golden, R., Paciano, E., Englar, R., Gaeta, R., Paterson, J, Mason, D., “Part1: The Wind Tunnel Model Design and Fabrication of Cal Poly’s AMELIA 10 Foot Span Hybrid Wing-Body Low Noise CESTOL Aircraft,” 49th AIAA Aerospace Sciences Meeting, Orlando FL, AIAA-2011-1306, January 4-7, 2011.

Marshall, David D., Lichtwardt, Jonthan, A., Pham, John, Blessing, Bryan, and Storm, Travis, “Summary of the Aerodynamic Modeling Efforts for Amelia”, AIAA 2013-0973, 51st AIAA Aerospace Sciences Meeting including the New Horizons Forum and Aerospace Exposition 07-10 January 2013, Grapevine (Dallas/Ft. Worth Region

McMasters, JH, Nordvik, RH, Henderson, RH, and Sandvig, JH (1981) Two Airfoil Sections Designed for Low Reynolds Number. *Technical Soaring*, vol. VI, no4, XVIIth OSTIV Congress, Paderbon, Germany.

Soderman, P. T., and Allen, C. A., Aeroacoustic Measurements, Springer-Verlag Berline Heidenlberg, Germany, ed Thomas J. Mueller, 2002.

Soderman, P. T., Jaeger, S. M., Hayes, J. A., Allen, C.S., “Acoustic Performance of the 40-x by 80-Foot Wind Tunnel Section Deep Acoustic Lining,” NASA/TP-2002-211851, November, 2002.

Figures

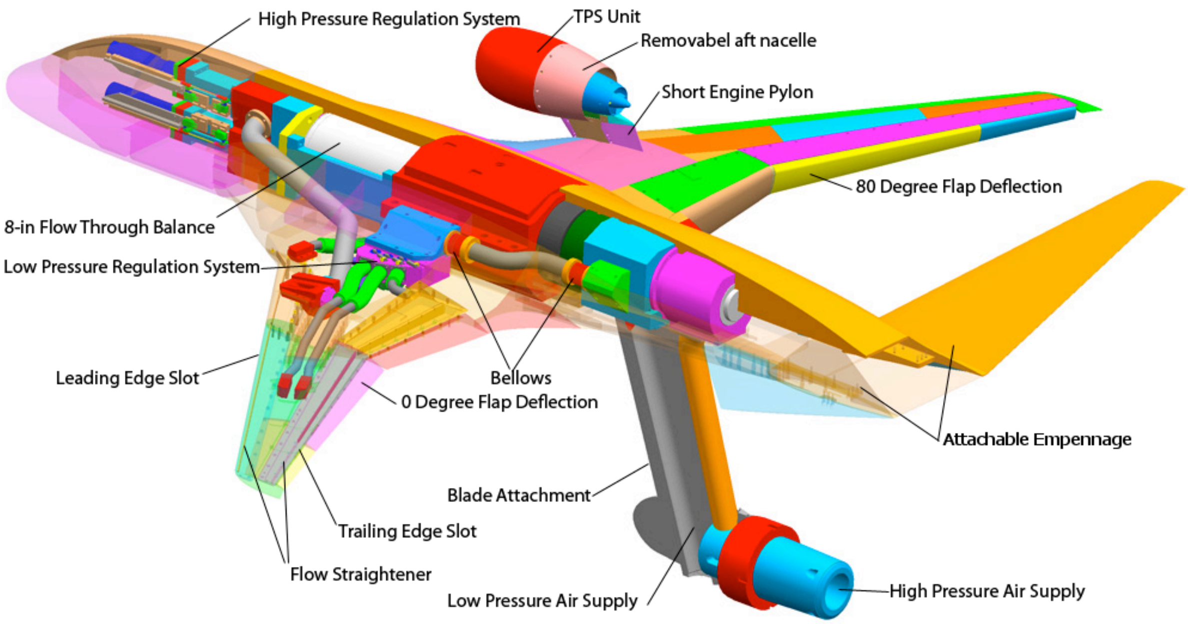

Figure 1. View of model internal components. TPS air is supplied through the sting / blade (high pressure air supply) CCW air from external hoses (low pressure air supply).

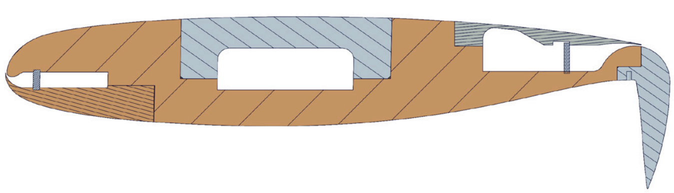

Figure 2. Inboard wing cross-section at 26% of semi-span from centerline (middle of inboard flap), flap angle 80º.

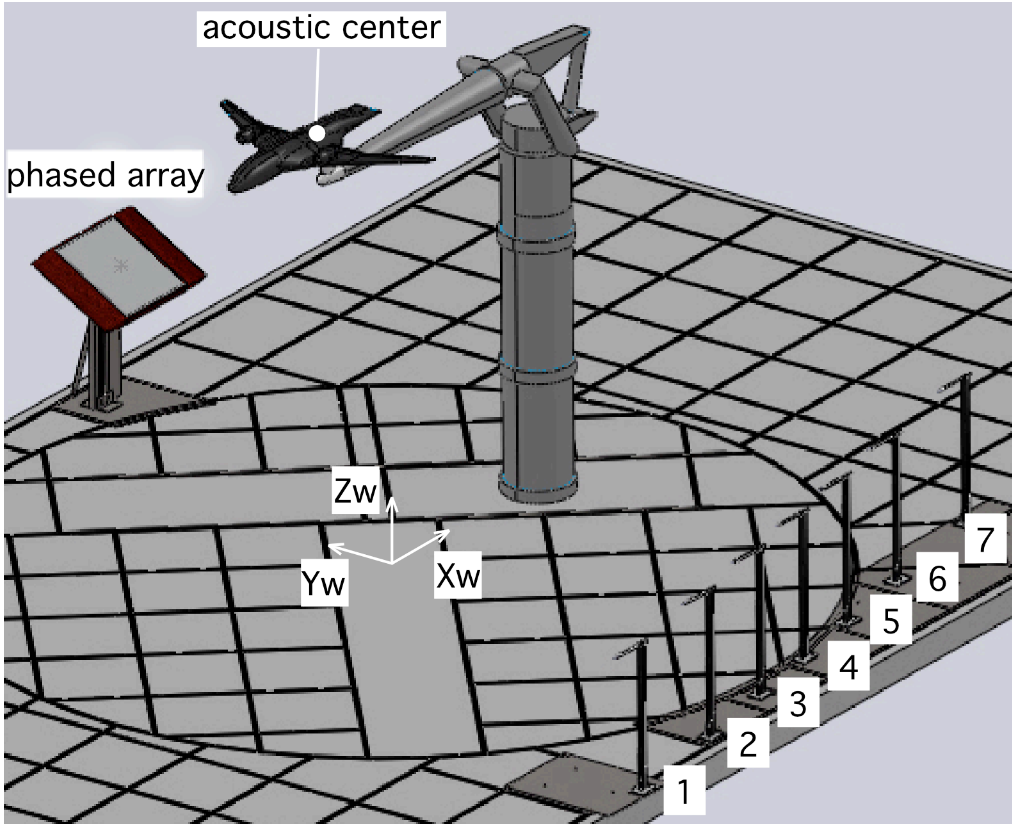

Figure 3. CESTOL test section layout. Note that the acoustic center moves with attitude and sideslip.

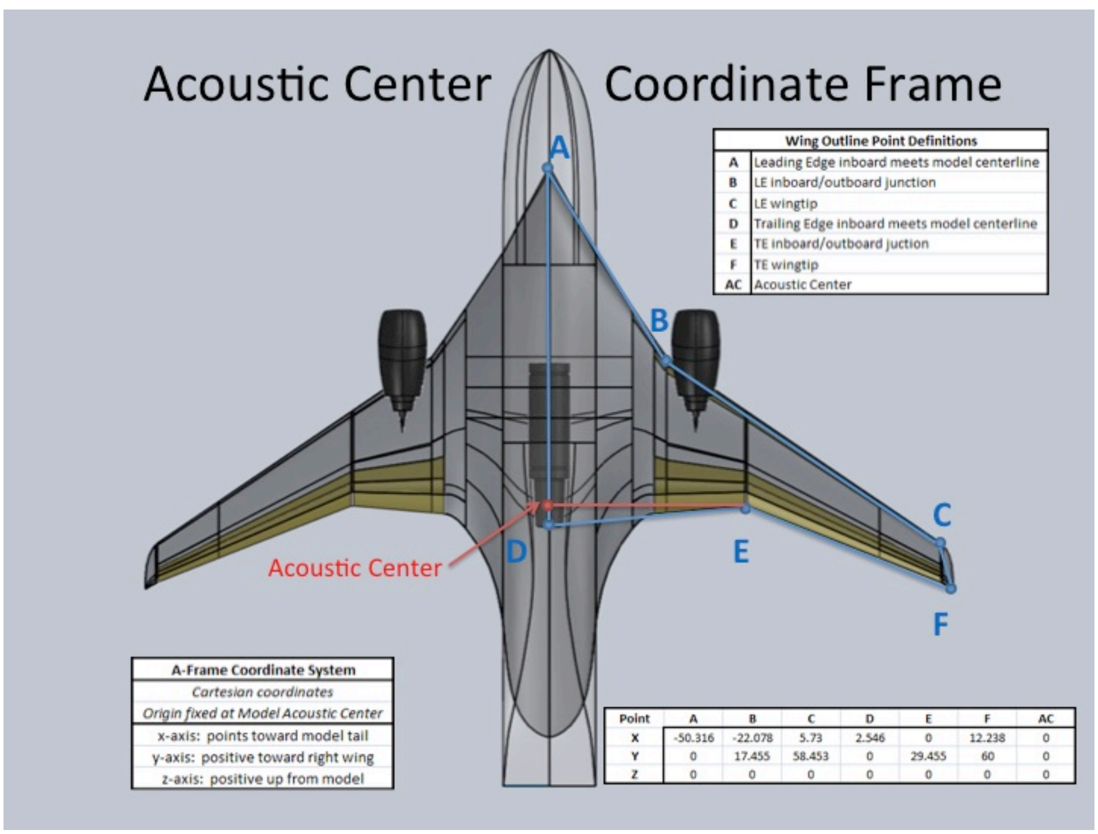

Figure 4. Acoustic center definition looking down on the model.

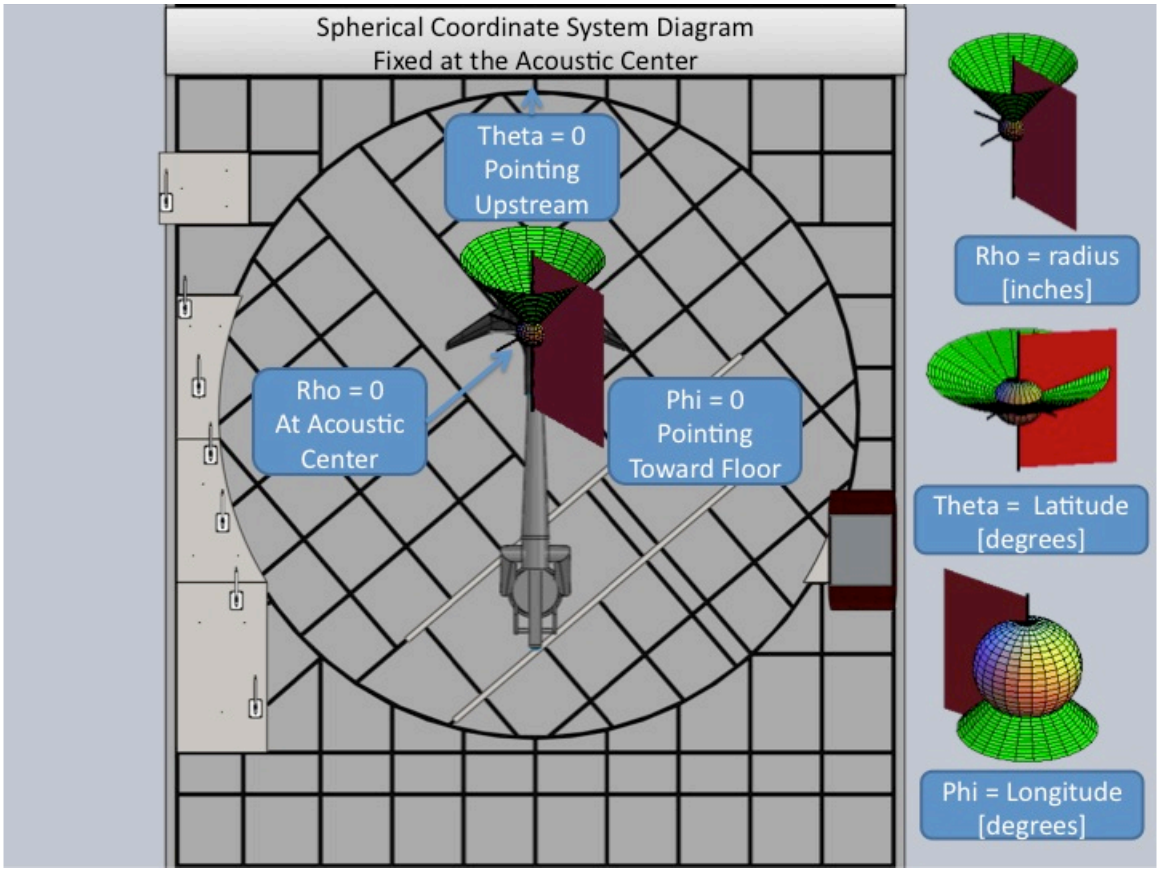

Figure 5. Spherical coordinate system centered at the model acoustic center.

Figure 6. Overhead view of Arnold Engineering Development Complex NFAC.

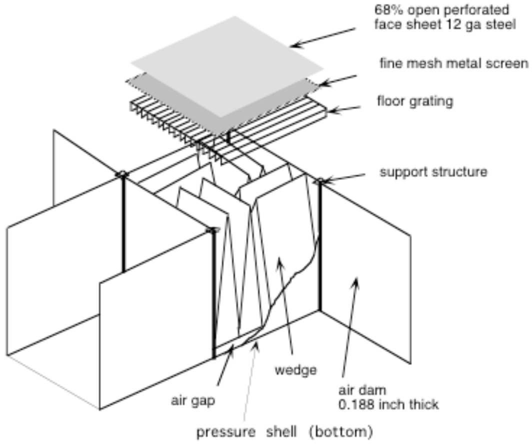

Figure 7. Test section acoustic treatment.

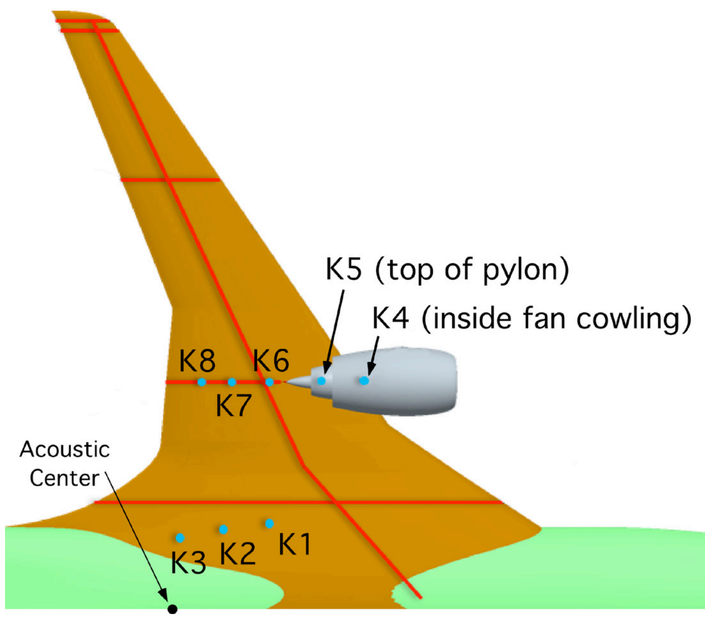

Figure 8. Unsteady surface pressure sensor locations, top view.

Figure 9. G.R.A.S. RA0022 nosecone.

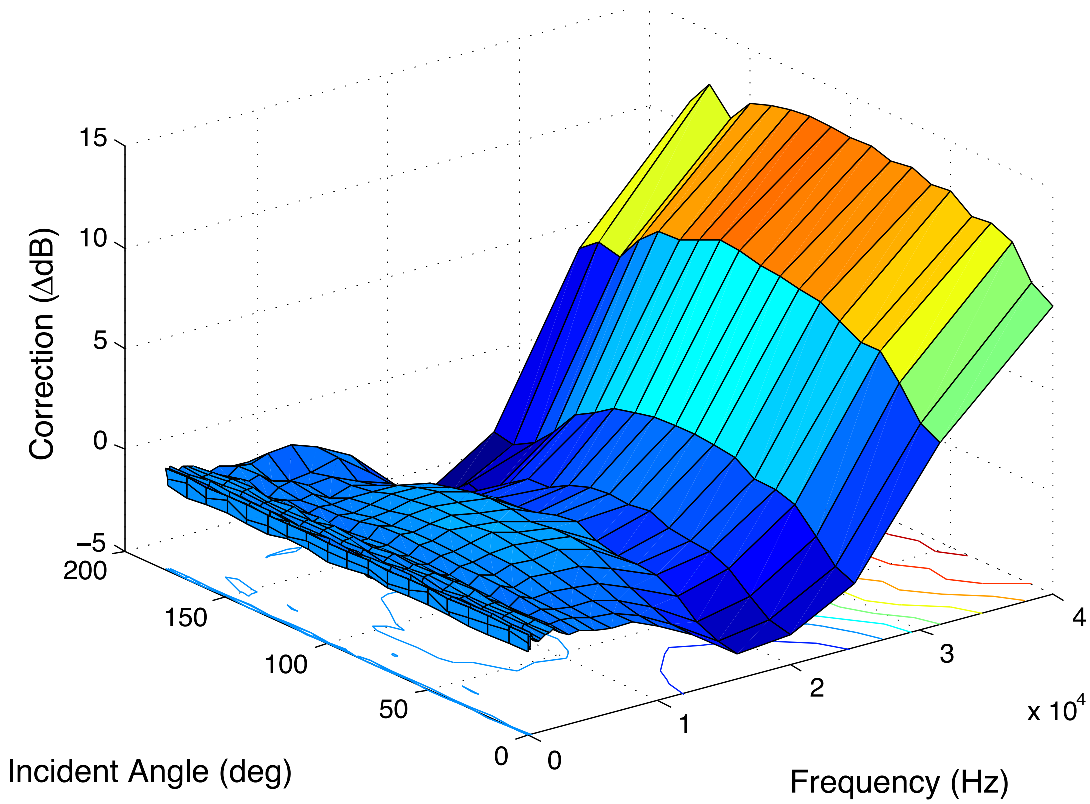

Figure 10. GRAS nosecone corrections as measure in the AOX anechoic chamber. Corrections are added to the measure data.

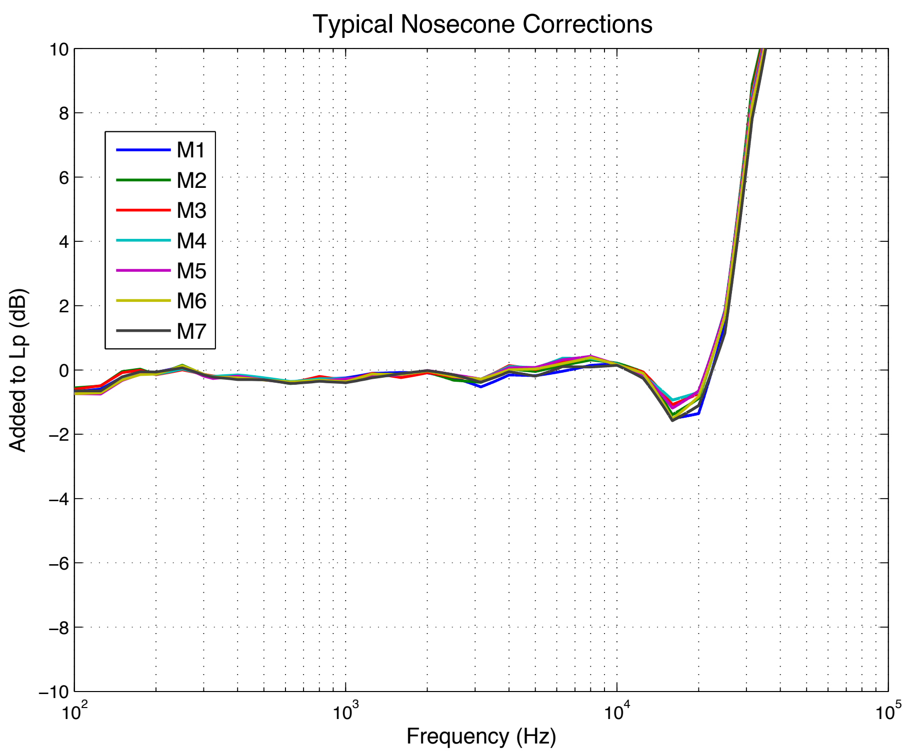

Figure 11. A sample of typical corrections applied to the single microphone data.

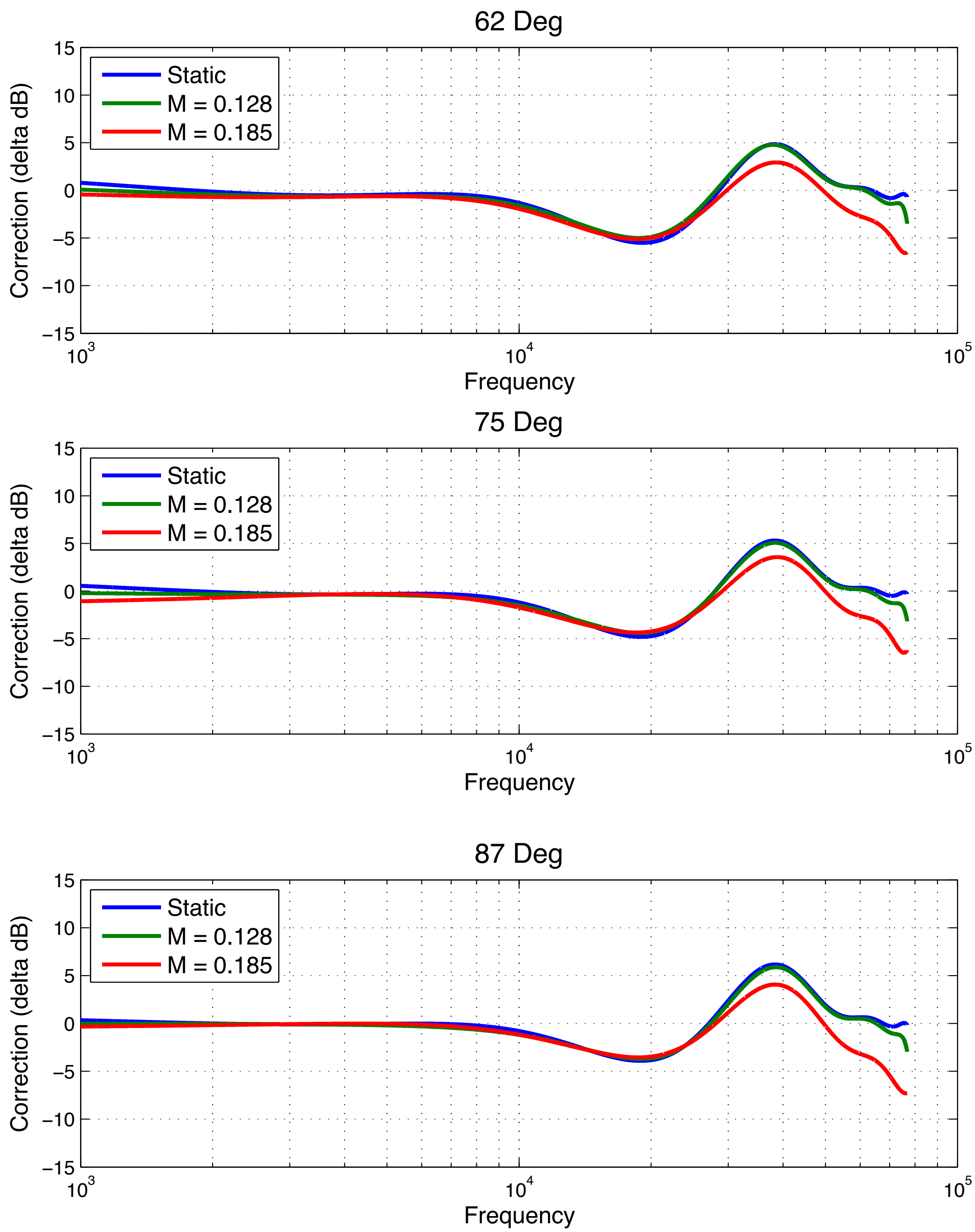

Figure 12. G.R.A.S. nosecone velocity calibration (62º - 87º).

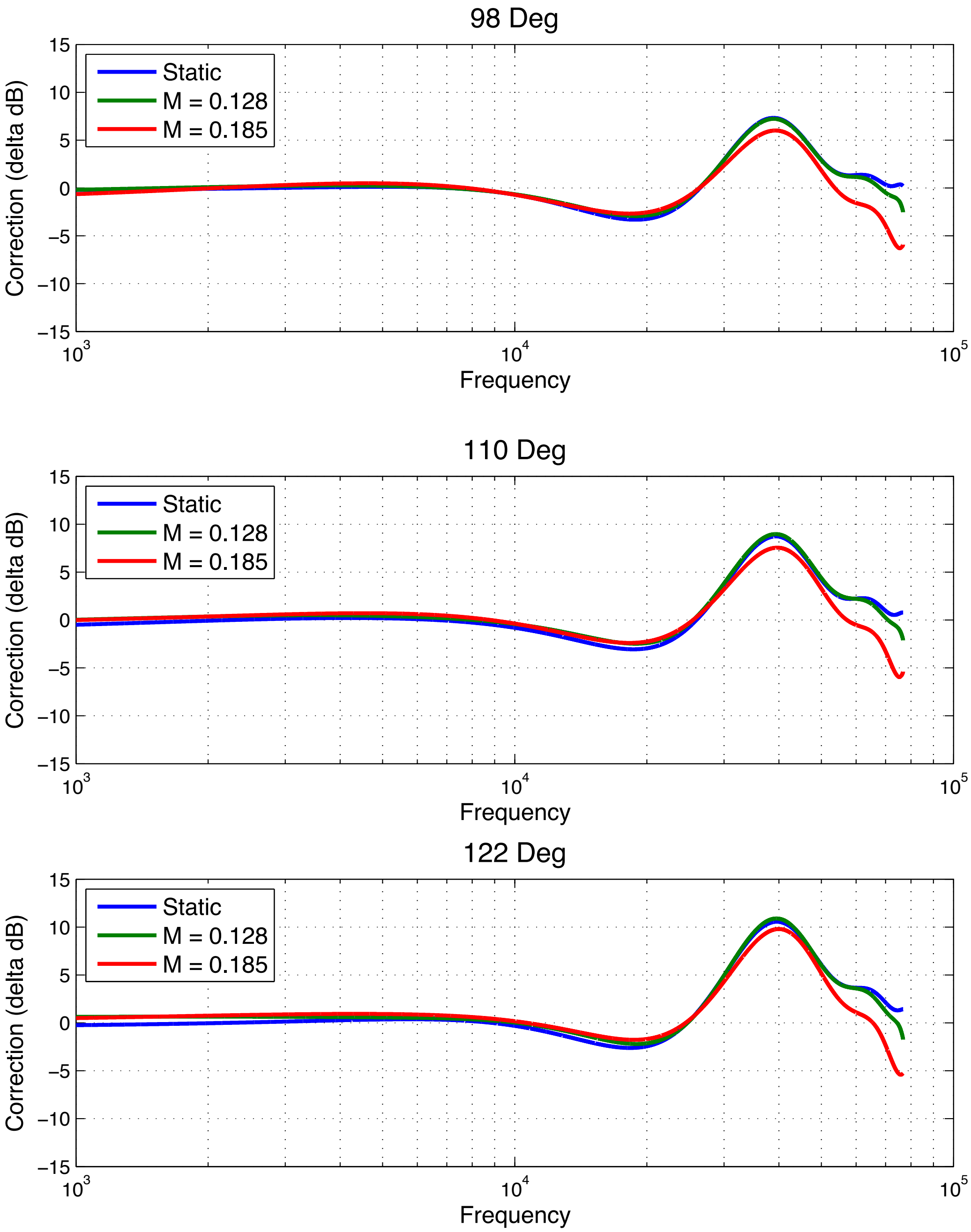

Figure 13. G.R.A.S. nosecone velocity calibration (98º - 122º).

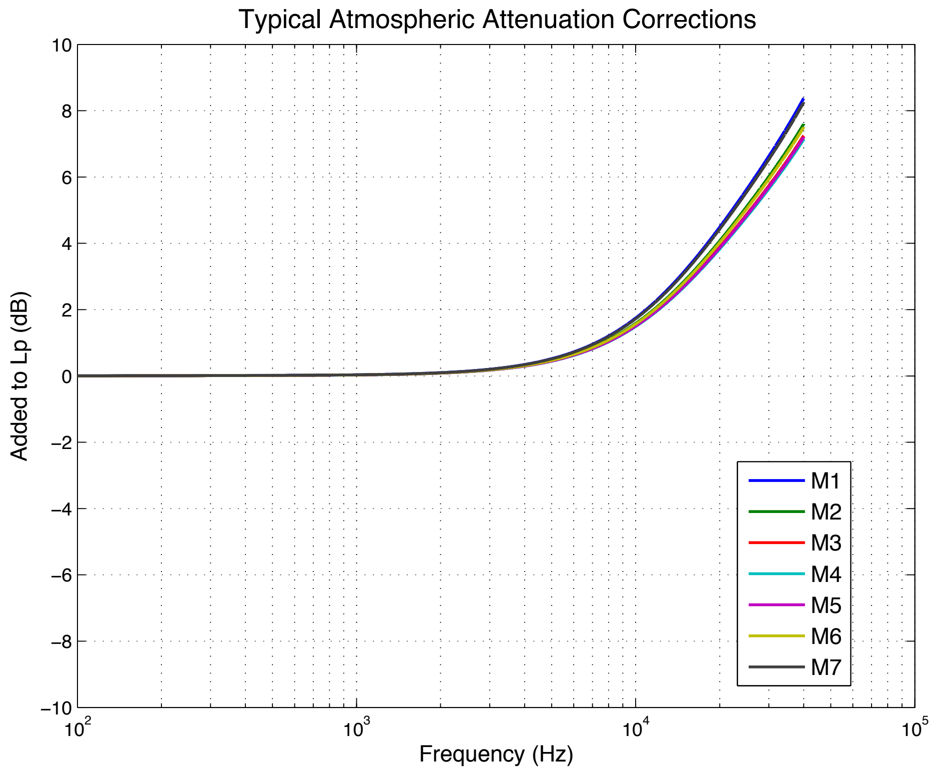

Figure 14. A sample of typical atmospheric attenuation corrections that were added to the data.

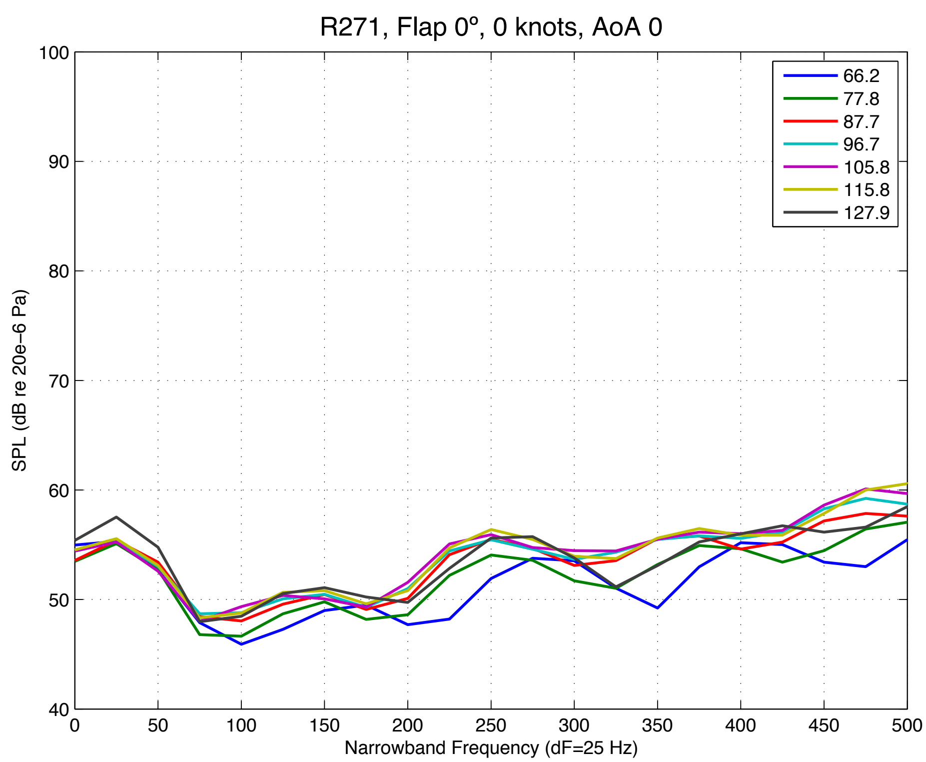

Figure 15. Low frequency reflection plot for no flow.

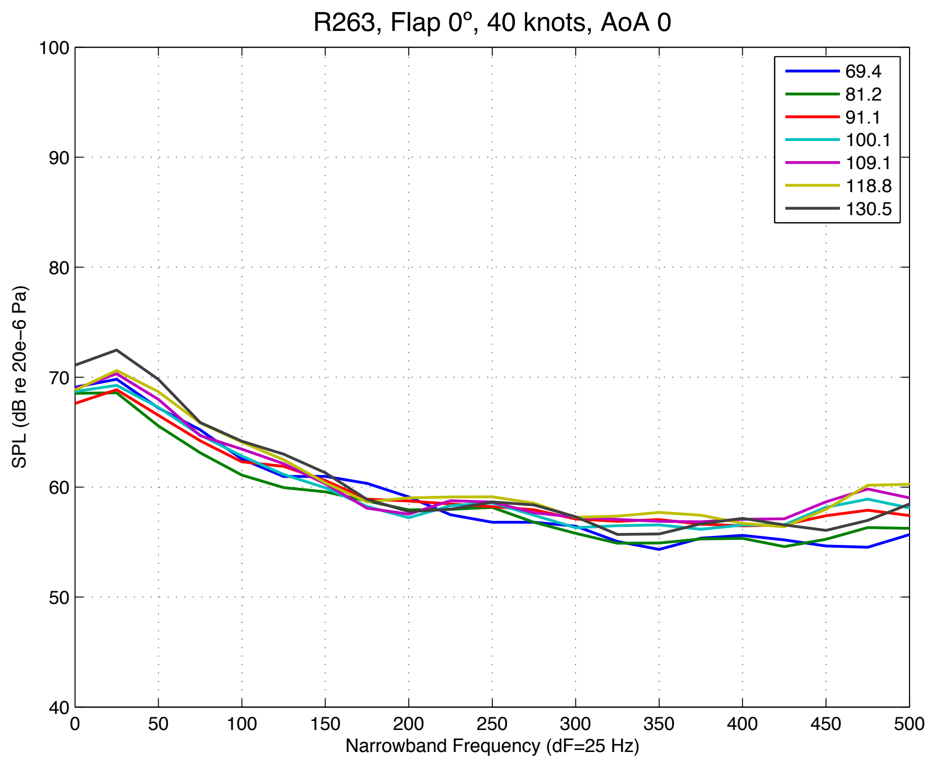

Figure 16. Low frequency reflection plot for V = 40 knots.

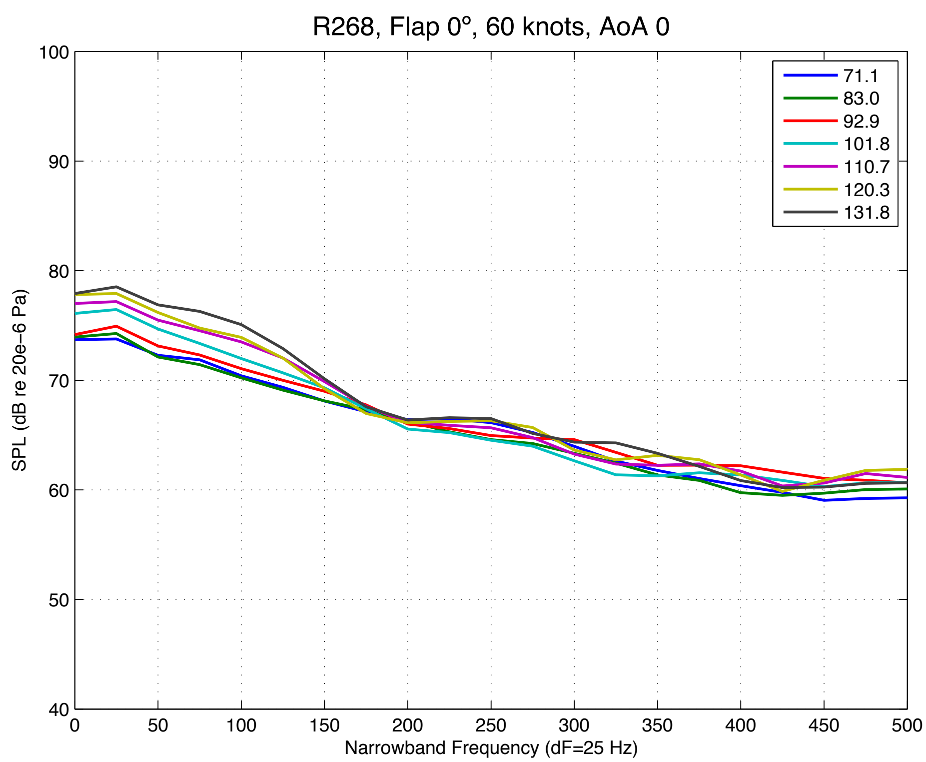

Figure 17. Low frequency reflection plot for V = 60 knots.

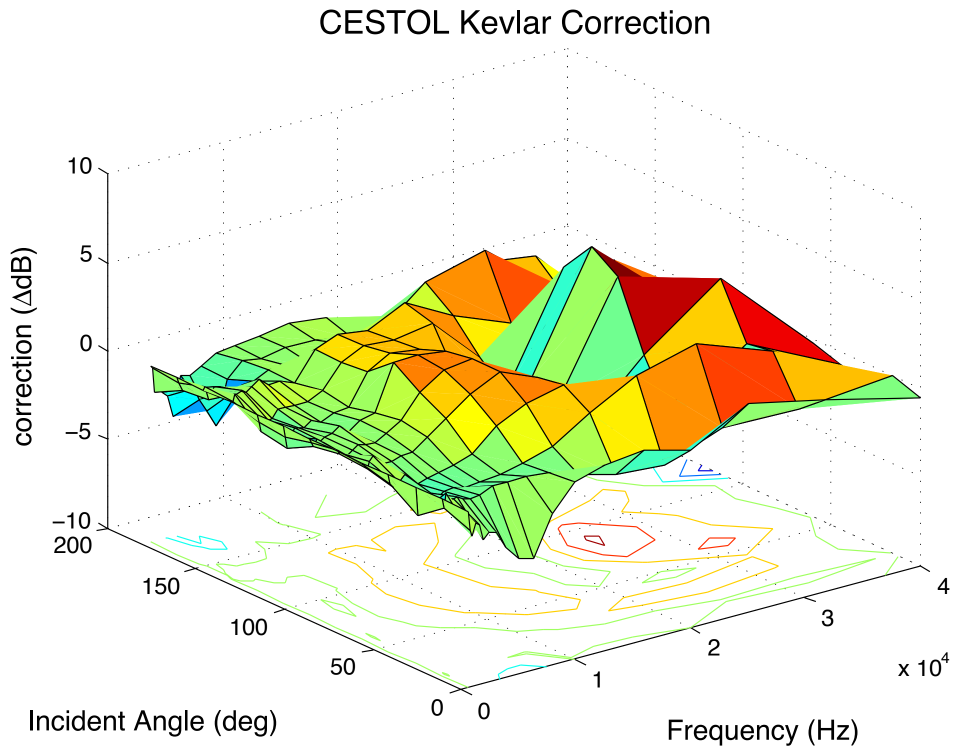

Figure 18. Kevlar correction measured in-situ of the 40x80.

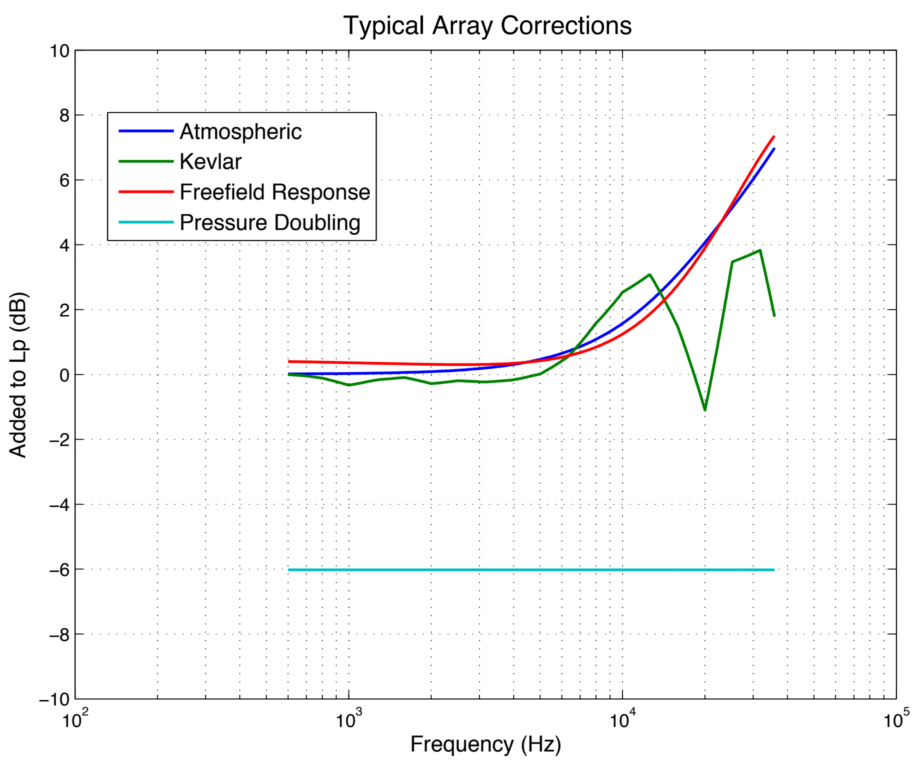

Figure 19. Typical corrections applied to array data.

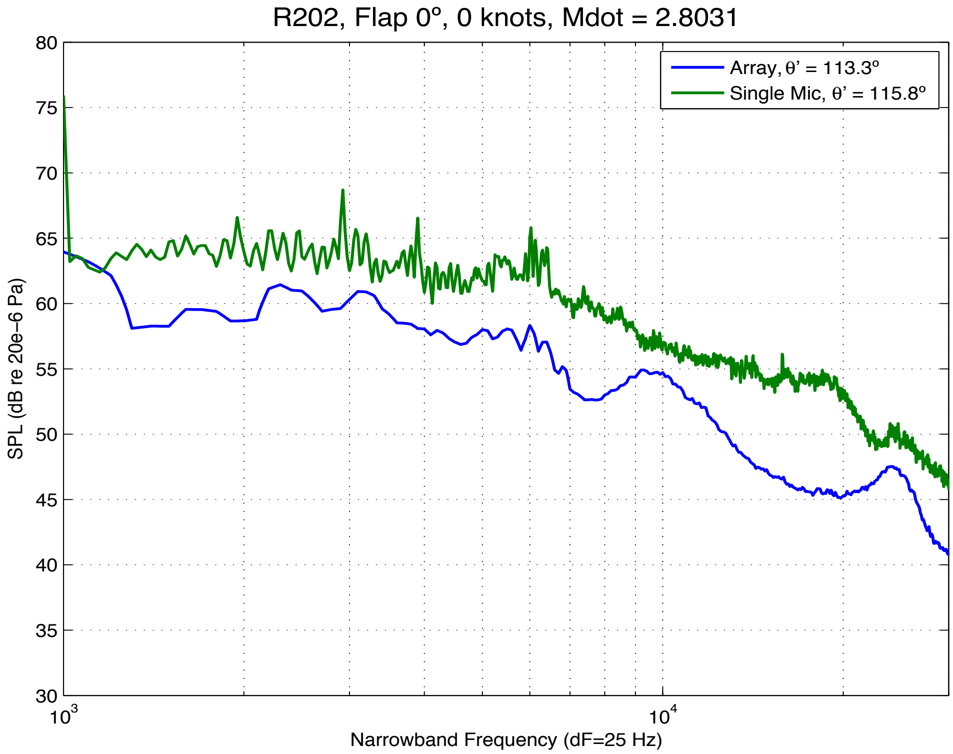

Figure 20. Array and microphone comparison for 0º flap, maximum leading- and trailing-edge blowing at V = 0 knots.

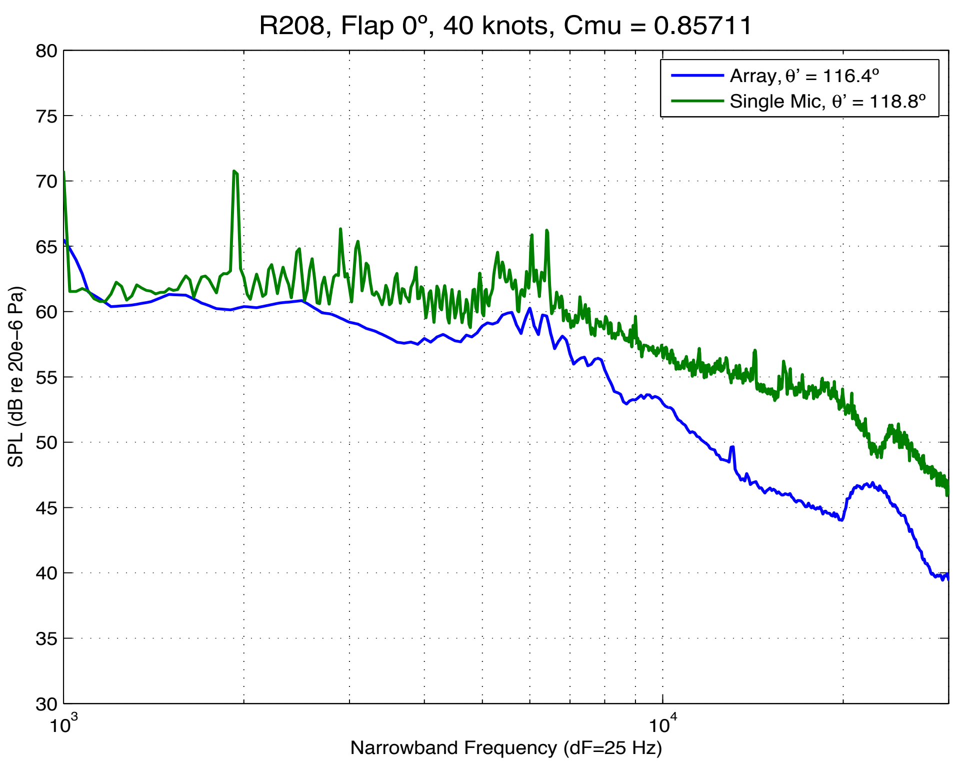

Figure 21. Array and microphone comparison for 0º flap, maximum leading- and trailing-edge blowing at V = 40 knots.

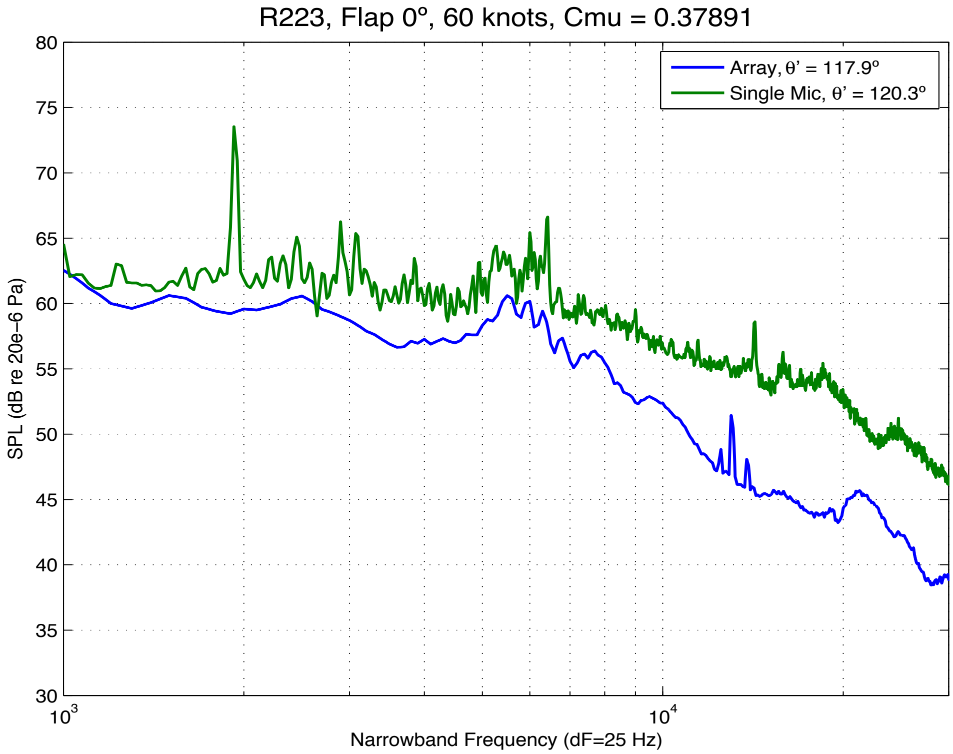

Figure 22. Array and microphone comparison for 0º flap, maximum leading- and trailing-edge blowing at V = 60 knots.

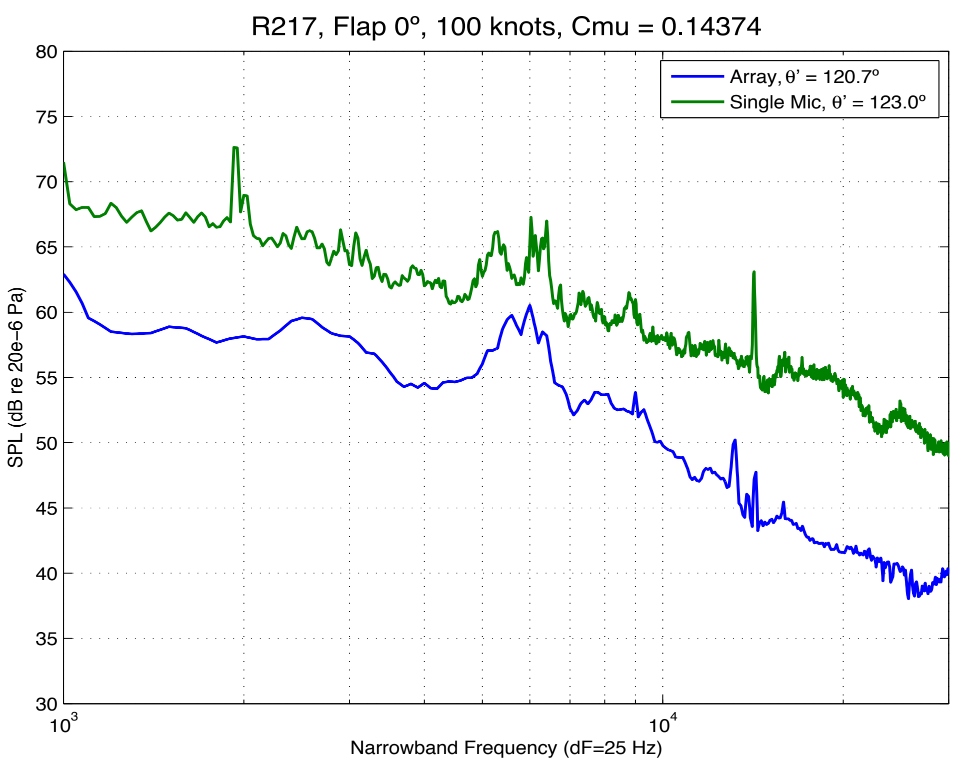

Figure 23. Array and microphone comparison for 0º flap, maximum leading- and trailing-edge blowing at V = 100 knots.

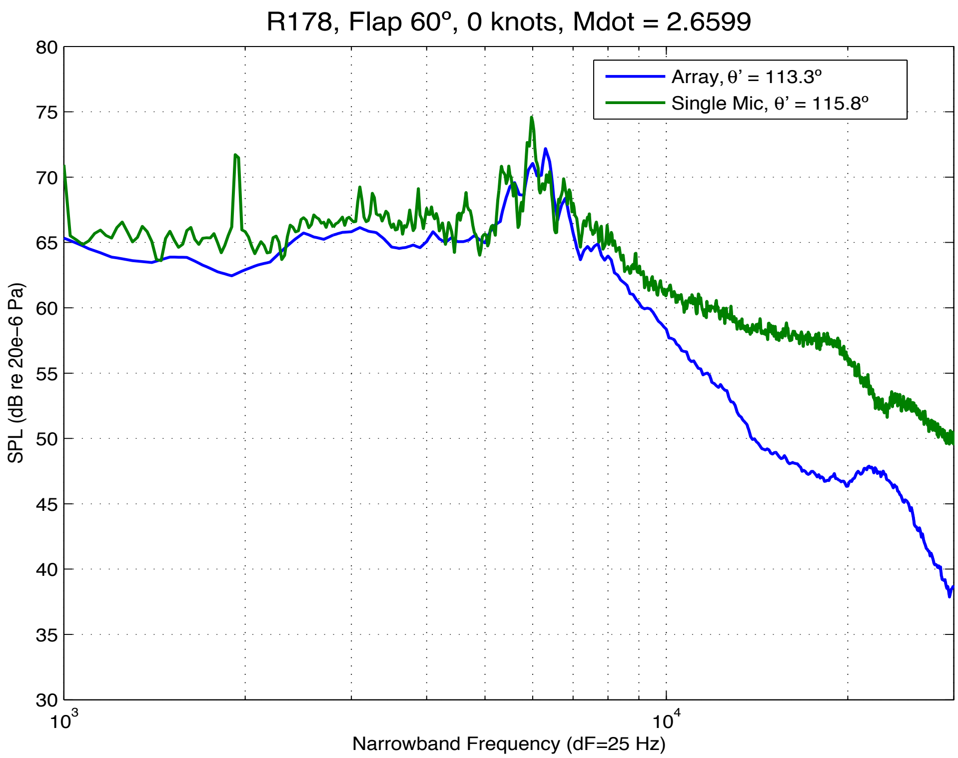

Figure 24. Array and microphone comparison for 60º flap, maximum leading- and trailing-edge blowing at V = 0 knots.

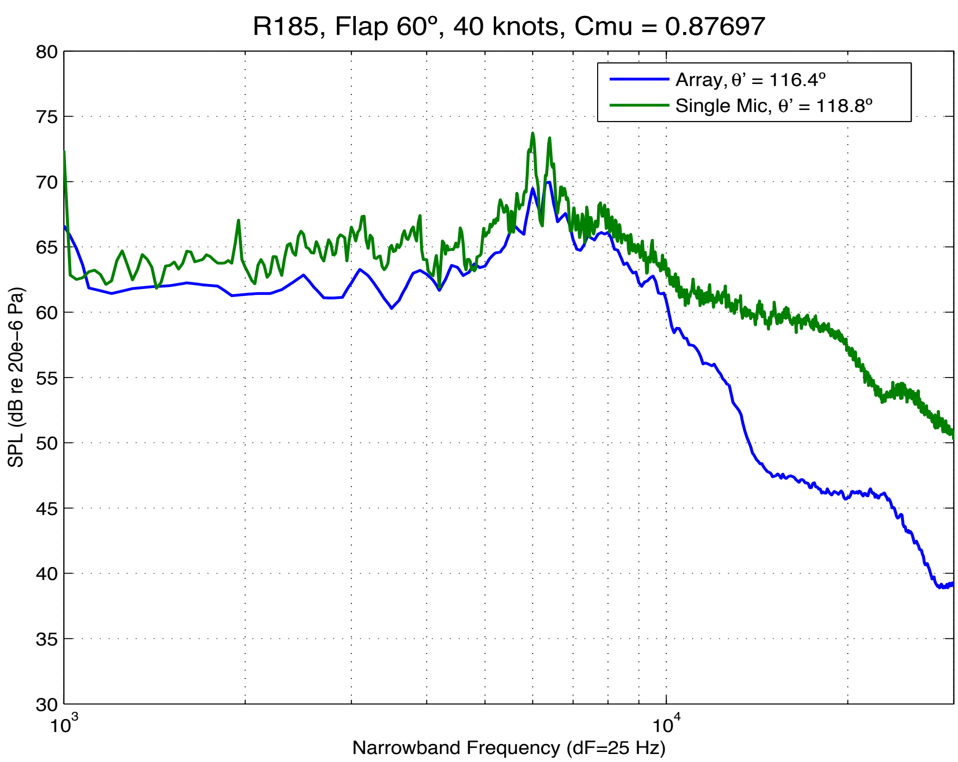

Figure 25. Array and microphone comparison for 60º flap, maximum leading- and trailing-edge blowing at V = 0 knots.

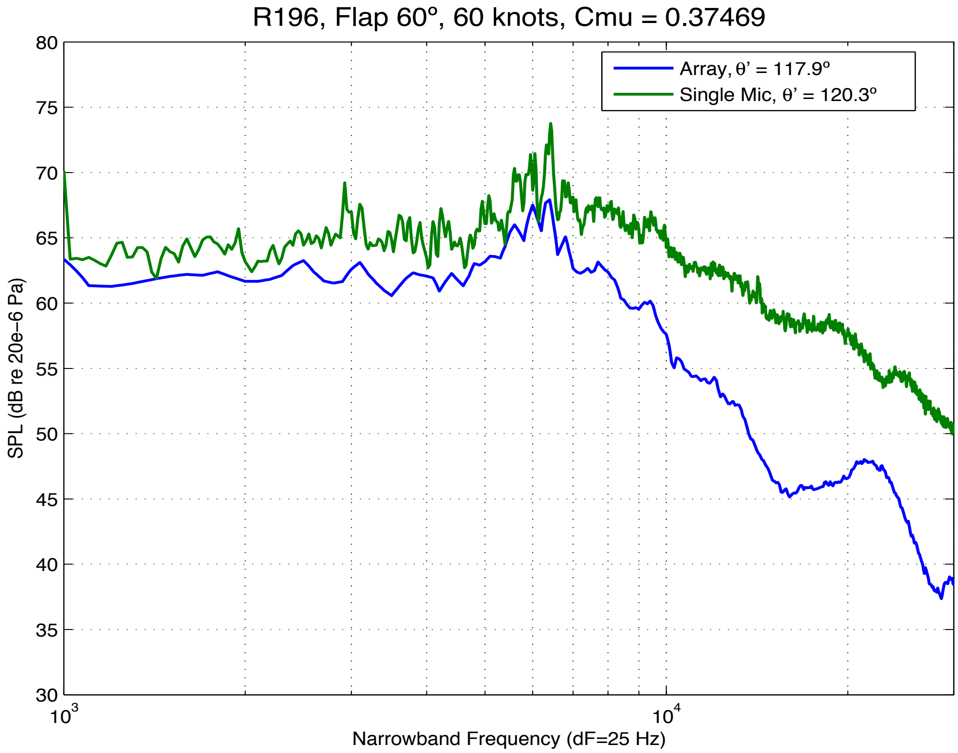

Figure 26. Array and microphone comparison for 60º flap, maximum leading- and trailing-edge blowing at V = 60 knots.

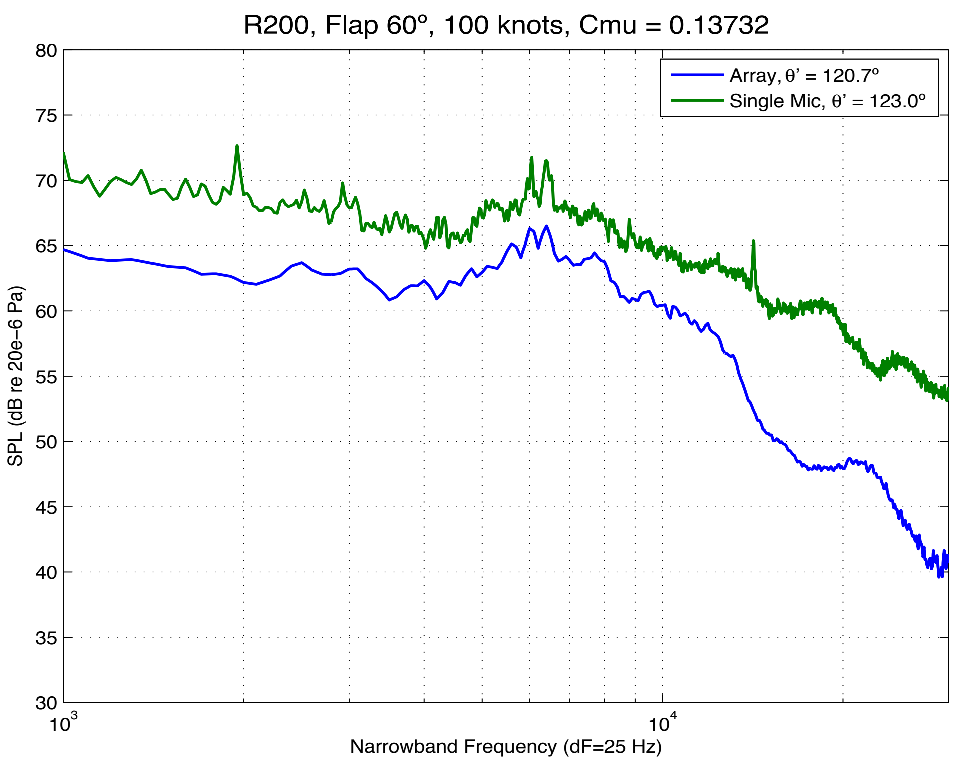

Figure 27. Array and microphone comparison for 60º flap, maximum leading- and trailing-edge blowing at V = 100 knots.

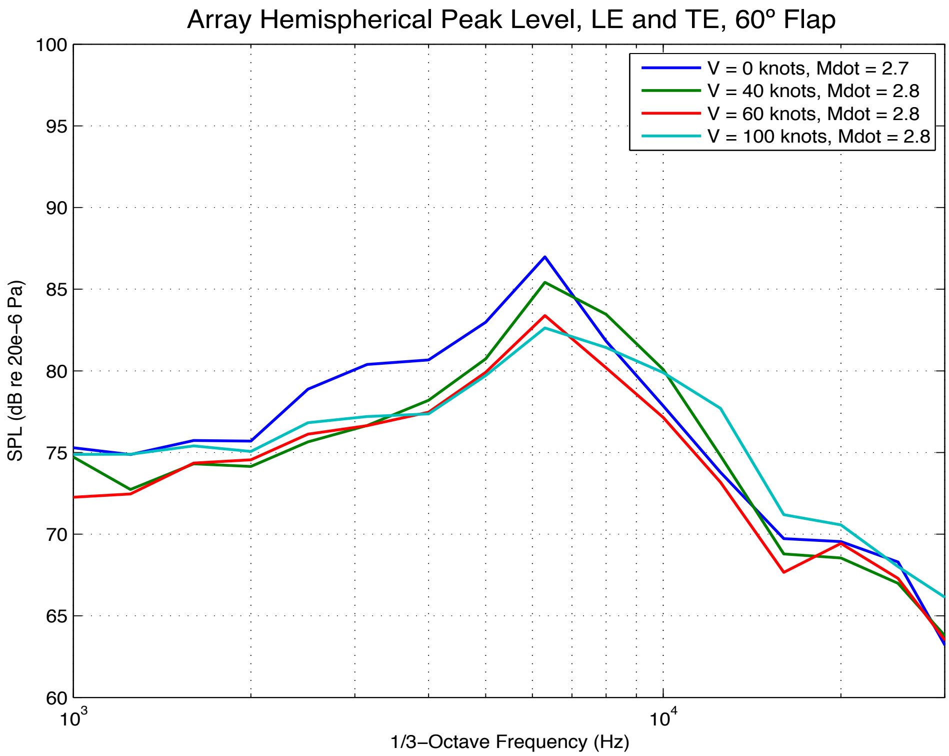

Figure 28. Phased array results for 60º flap velocity sweep.

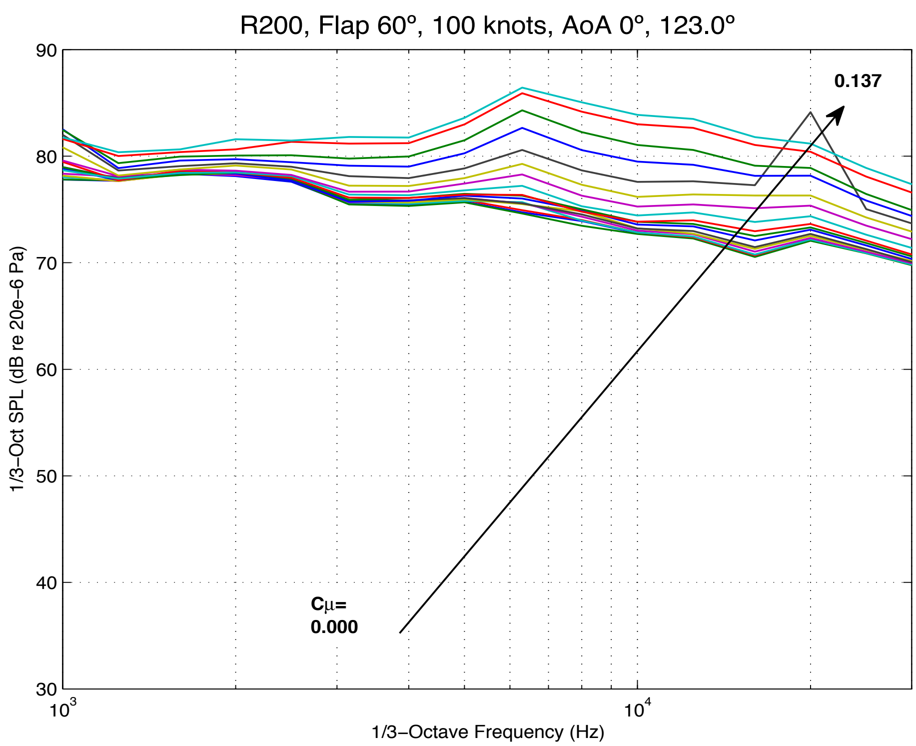

Figure 29. Single microphone Cμ sweep with 60º flap at 100 knots.

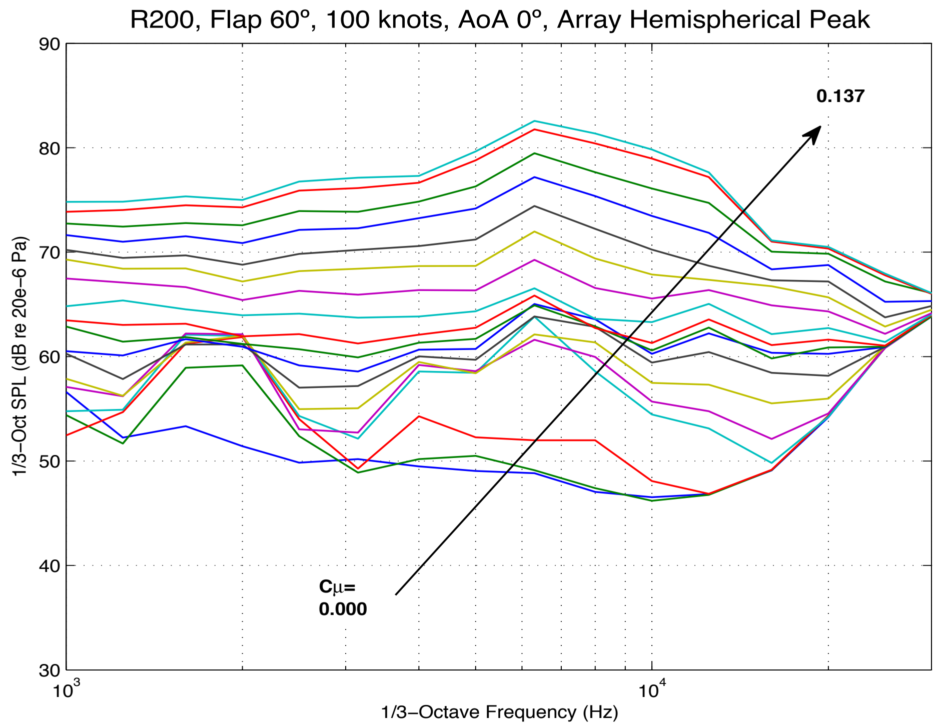

Figure 30. Phased array Cμ sweep with 60º flaps at 100 knots.

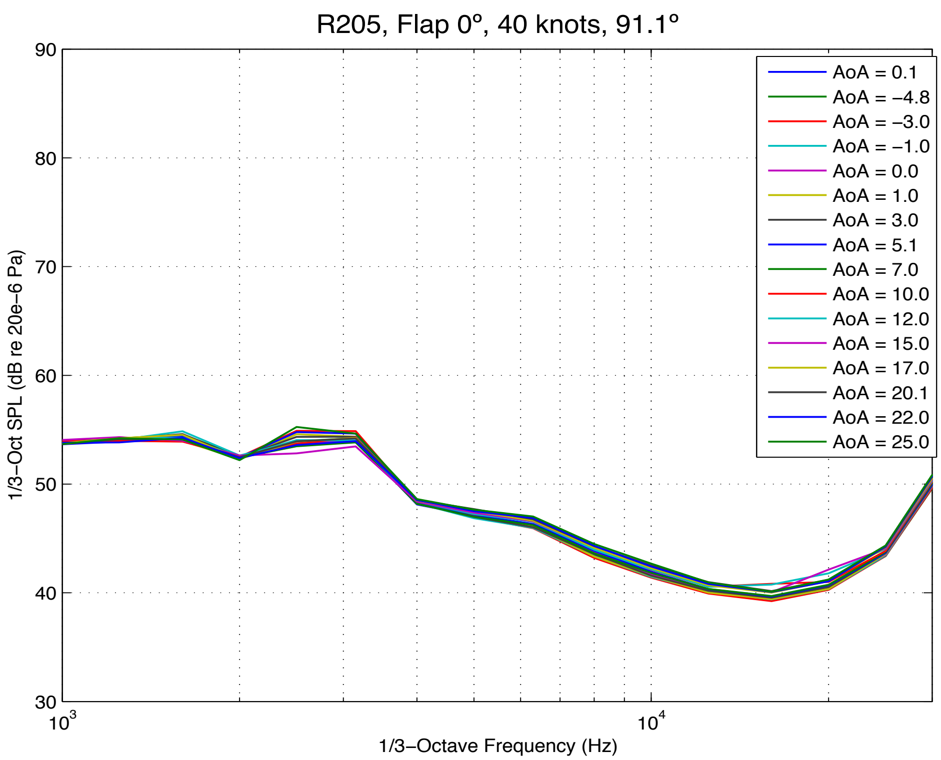

Figure 31. Angle-of-attack sweep with 0º Flap at 40 knots.

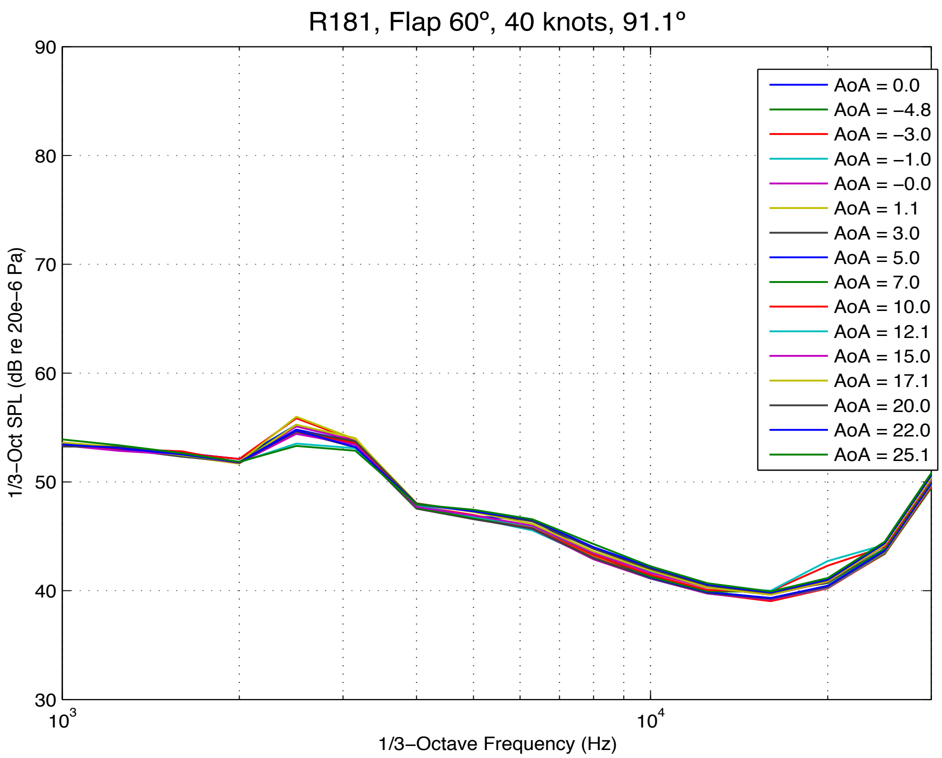

Figure 32. Angle-of-attack sweep with 60° Flap at 40 knots.

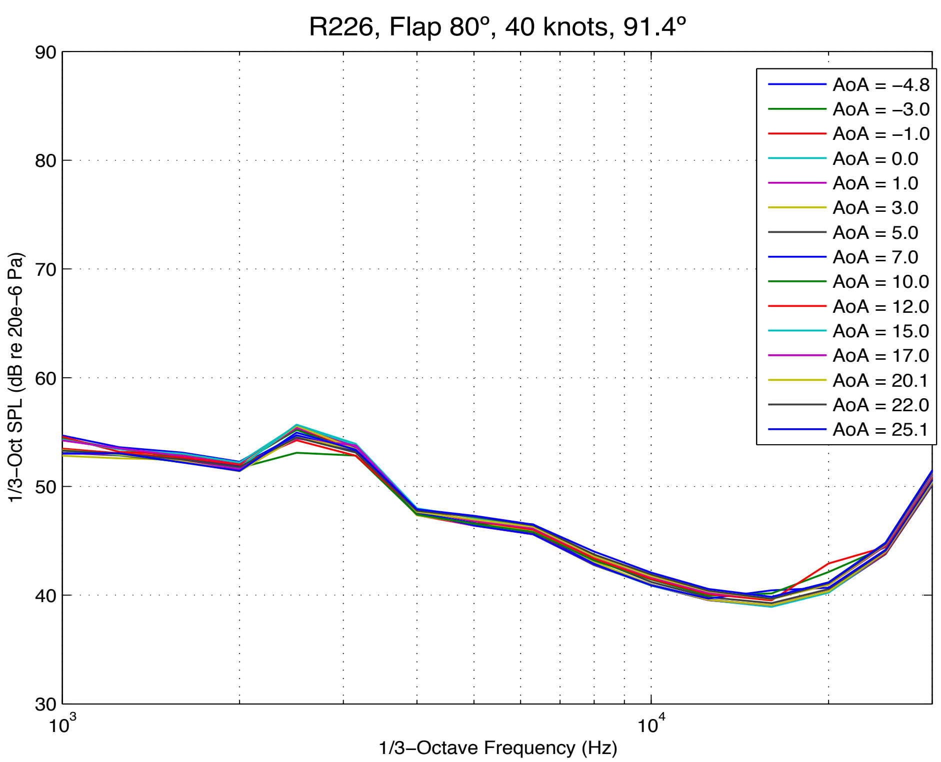

Figure 33. Angle-of-attack sweep with 80° Flap at 40 knots.

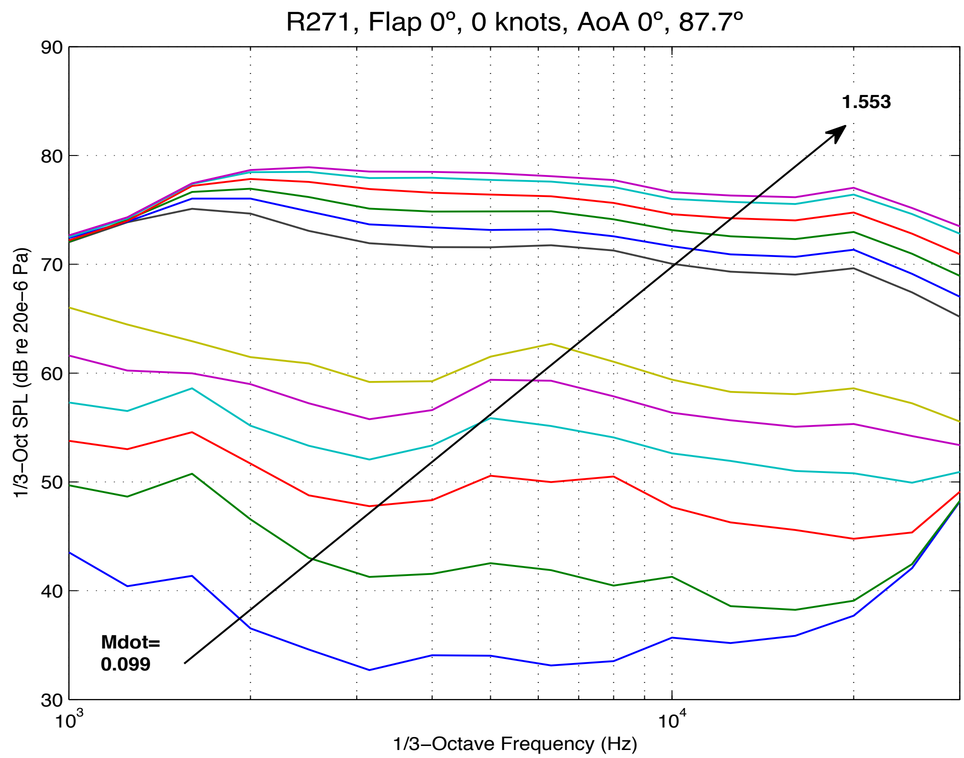

Figure 34. Trailing-edge only blowing Cμ sweep for α = 0°, 0° flap at 0 knots.

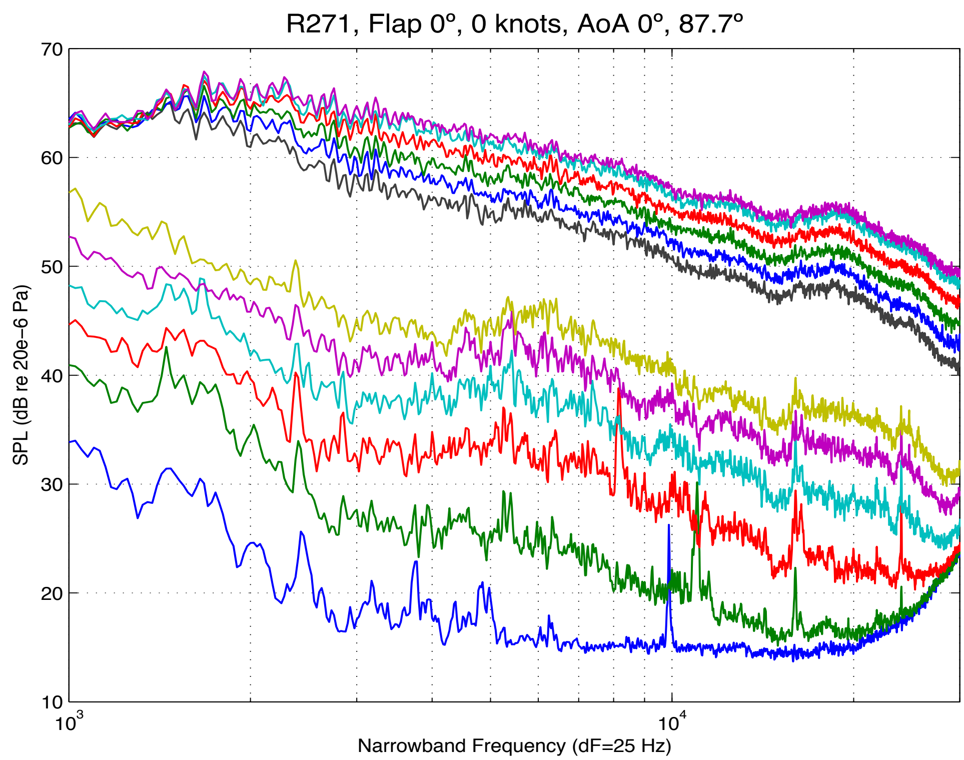

Figure 35. Narrowband plot of trailing-edge only blowing Cμ sweep for α = 0°, 0° flap at 0 knots.

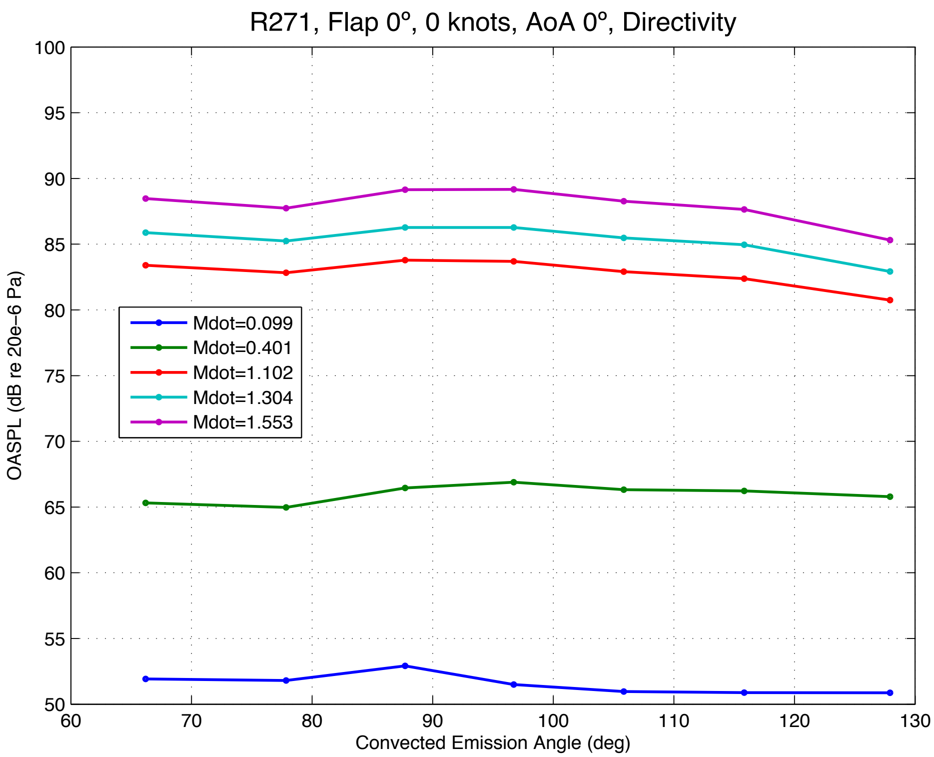

Figure 36. Directivity of trailing-edge only blowing Cμ sweep for α = 0º, 0º flap at 0 knots.

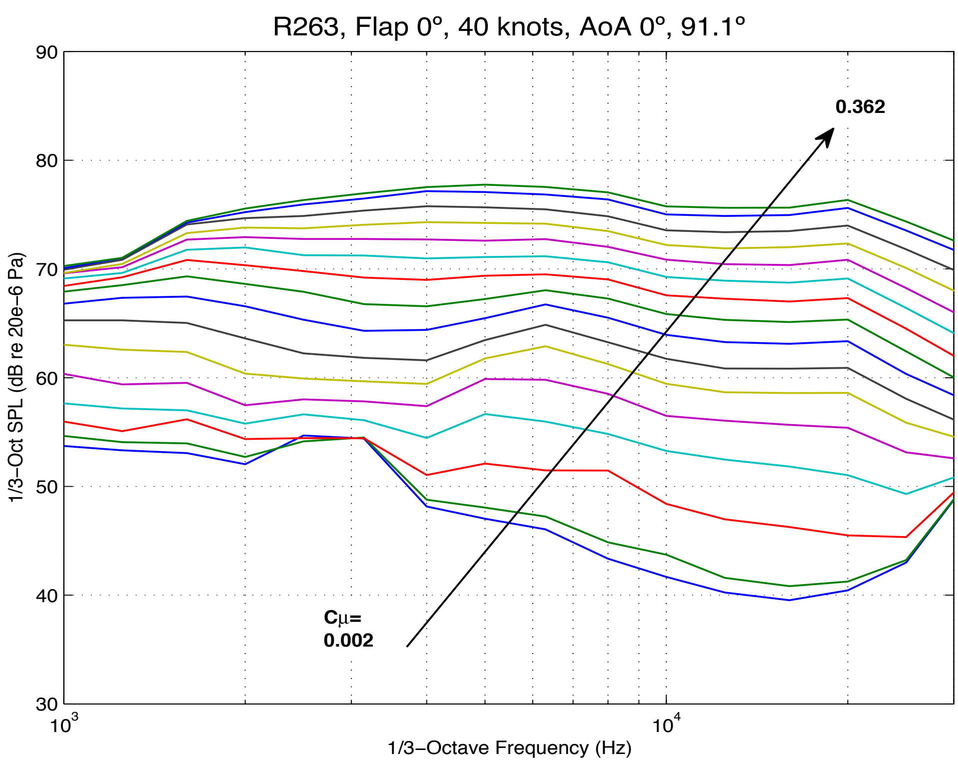

Figure 37. Trailing-edge only blowing Cμ sweep for α = 0º, 0º flap at 40 knots.

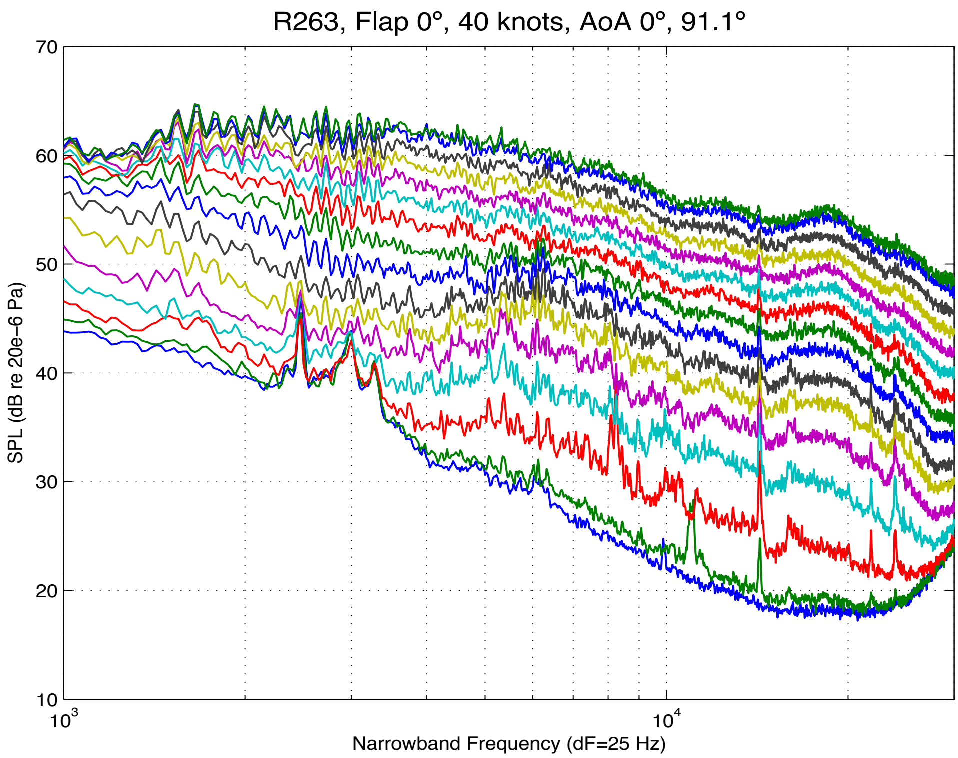

Figure 38. Narrowband plot of trailing-edge only blowing Cμ sweep for α = 0º, 0º flap at 40 knots

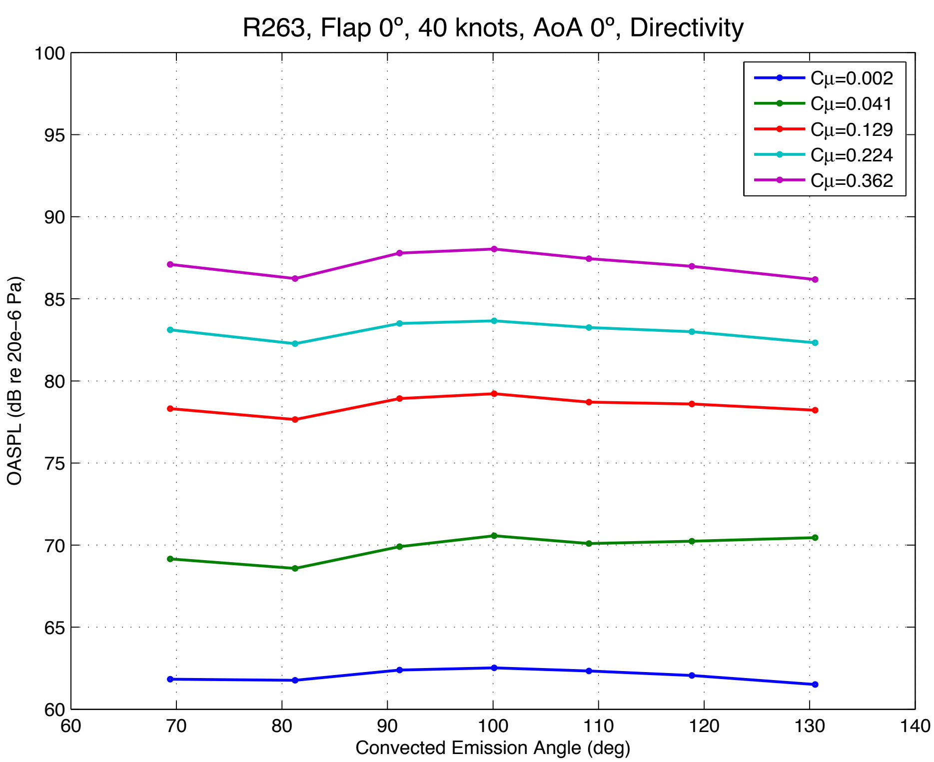

Figure 39. Directivity of trailing-edge only blowing Cμ sweep for α = 0º, 0º flap at 40 knots.

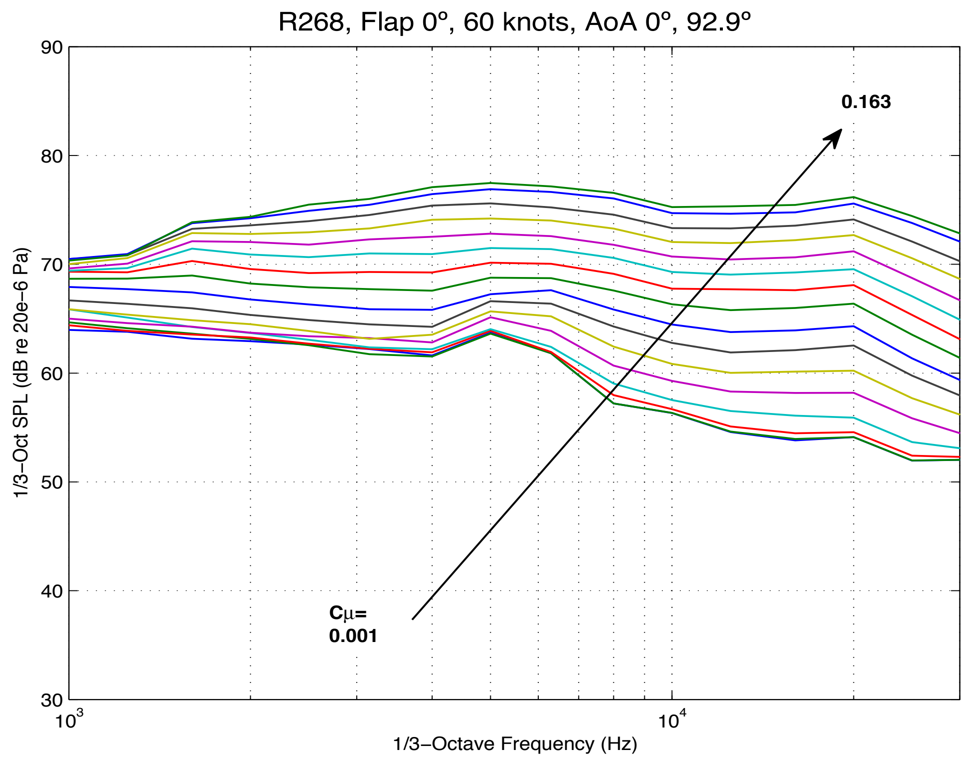

Figure 40. Trailing-edge only blowing Cμ sweep for α = 0º, 0º flap at 60 knots.

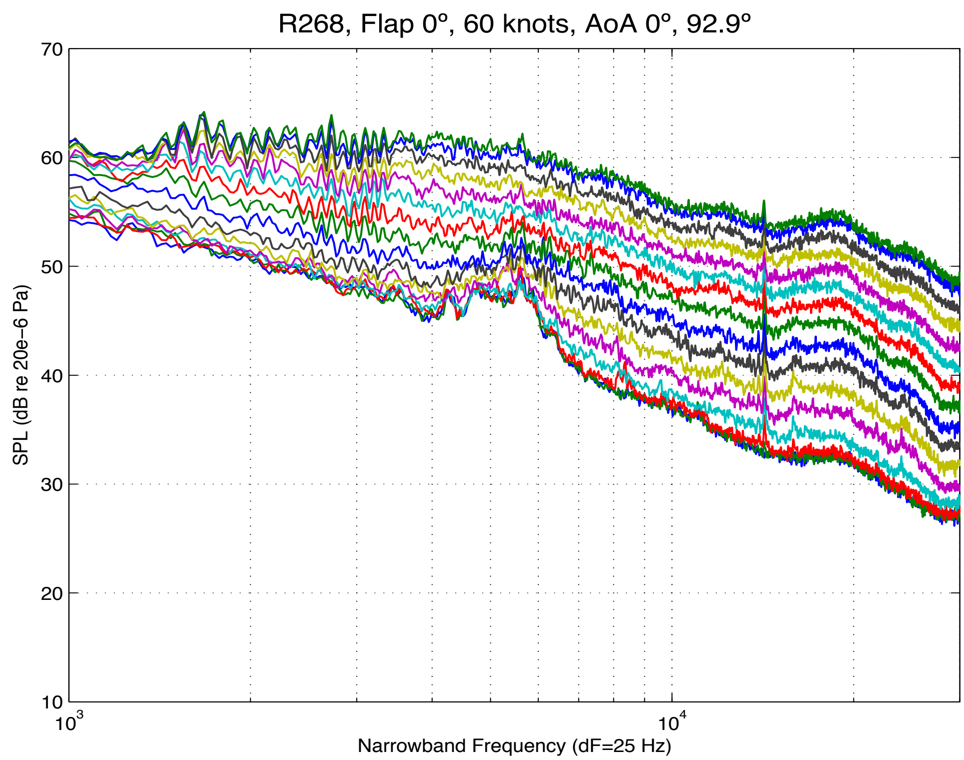

Figure 41. Narrowband plot of trailing-edge only blowing Cμ sweep for α = 0º, 0º flap at 60 knots.

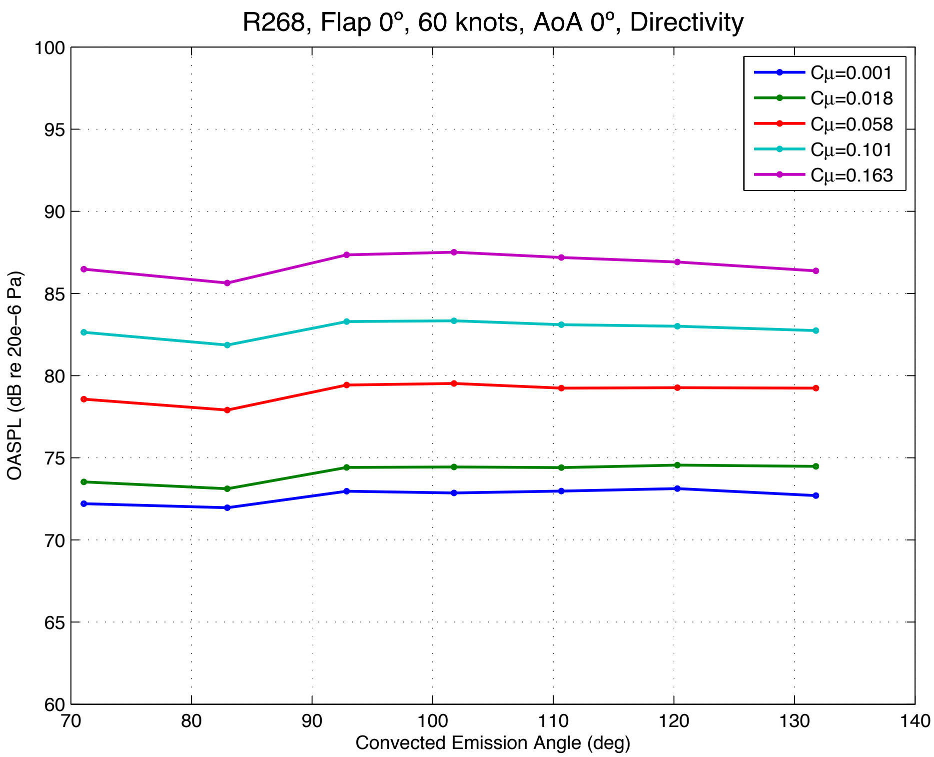

Figure 42. Directivity of trailing-edge only blowing Cμ sweep for α = 0°, 0° flap at 60 knots.

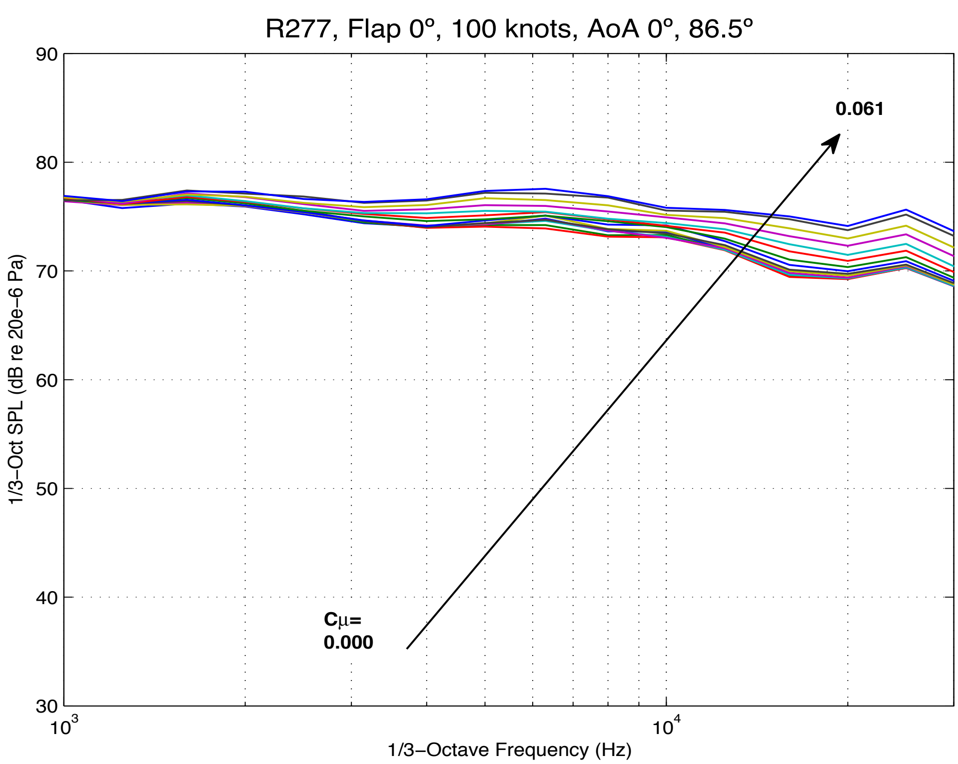

Figure 43. Trailing-edge only blowing Cμ sweep for α = 0°, 0° flap at 100 knots.

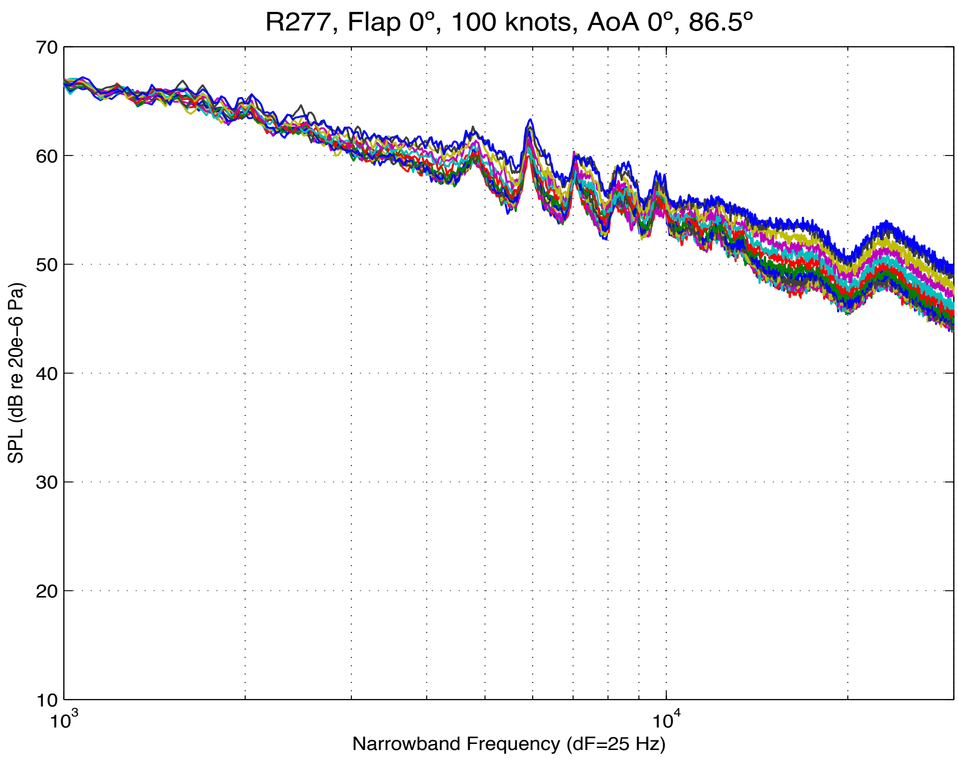

Figure 44. Narrowband plot of trailing-edge only blowing Cμ sweep for α = 0°, 0° flap at 100 knots.

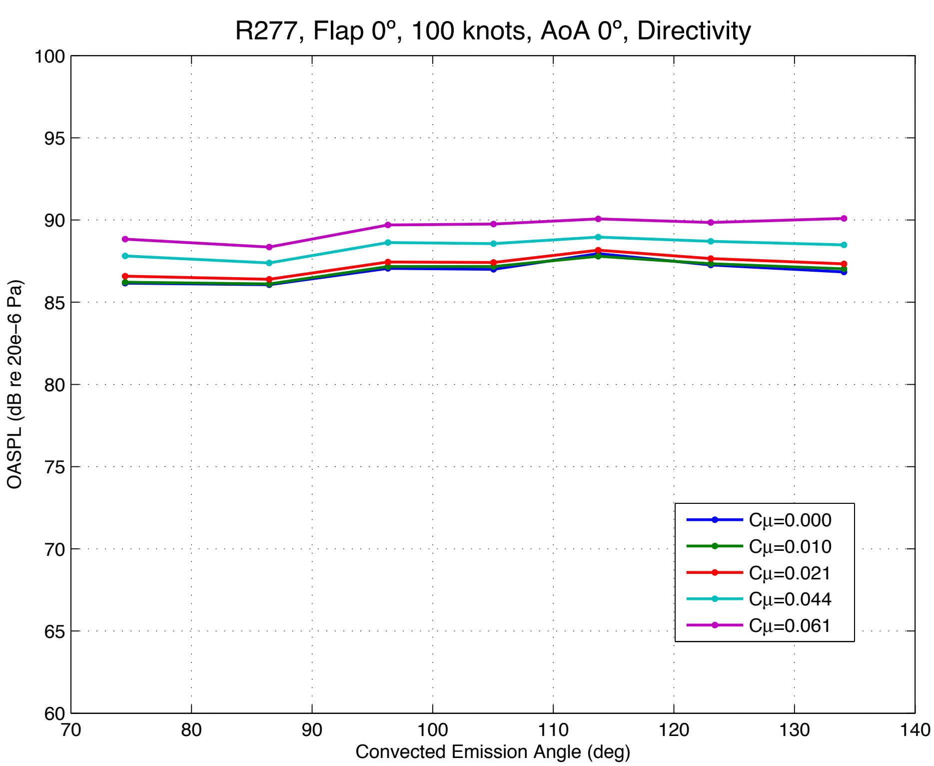

Figure 45. Directivity of trailing-edge only blowing Cμ sweep for α = 0°, 0° flap at 100 knots.

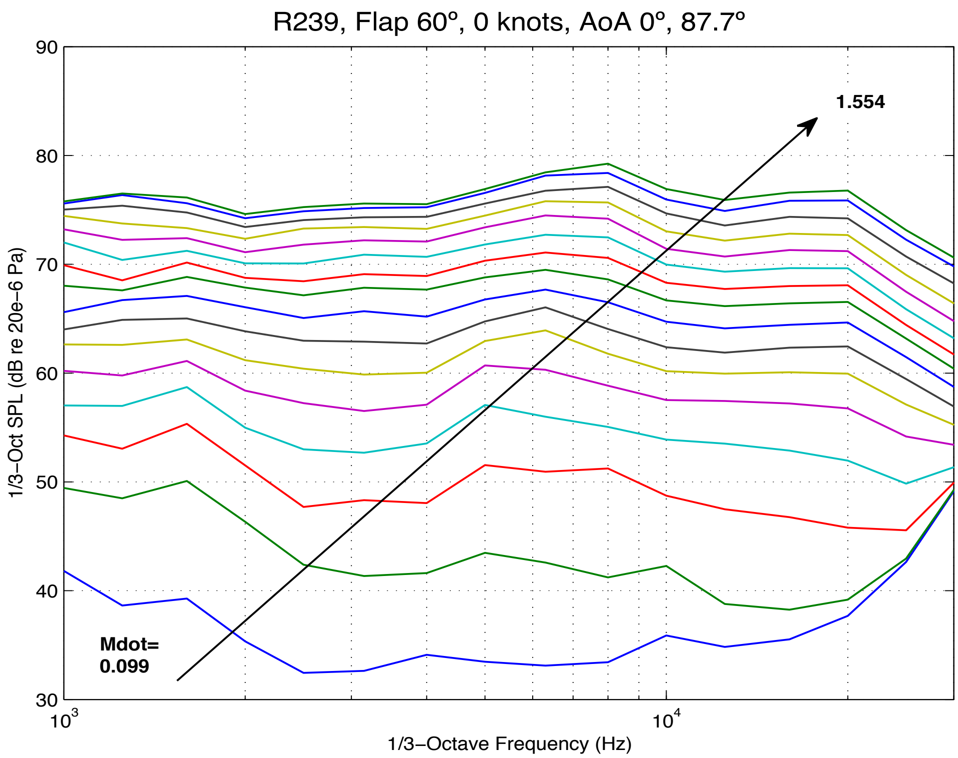

Figure 46. Trailing-edge only blowing Cμ sweep for α = 0°, 60° flap at 0 knots.

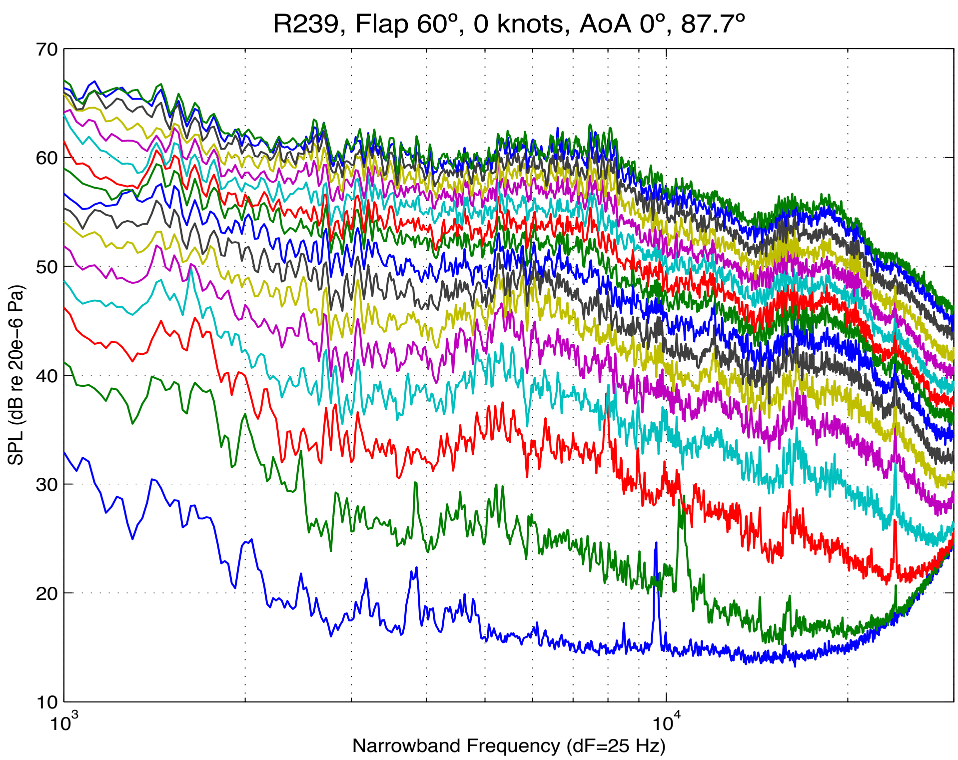

Figure 47. Narrowband plot of trailing-edge only blowing Cμ sweep for α = 0°, 60° flap at 0 knots.

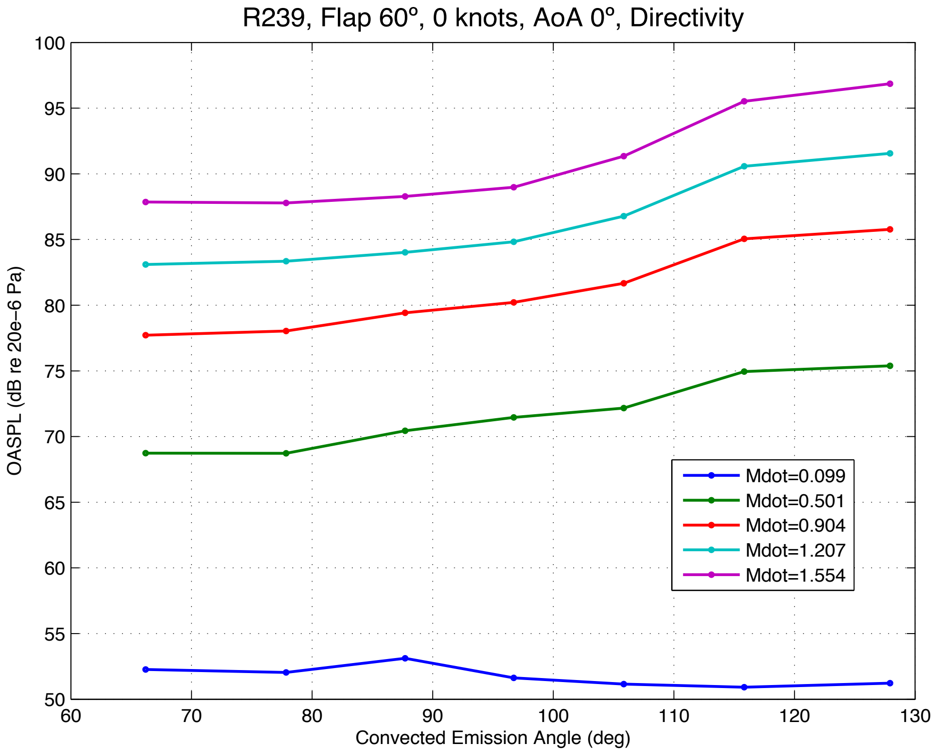

Figure 48. Directivity of trailing-edge only blowing Cμ sweep for α = 0º, 60º flap at 0 knots.

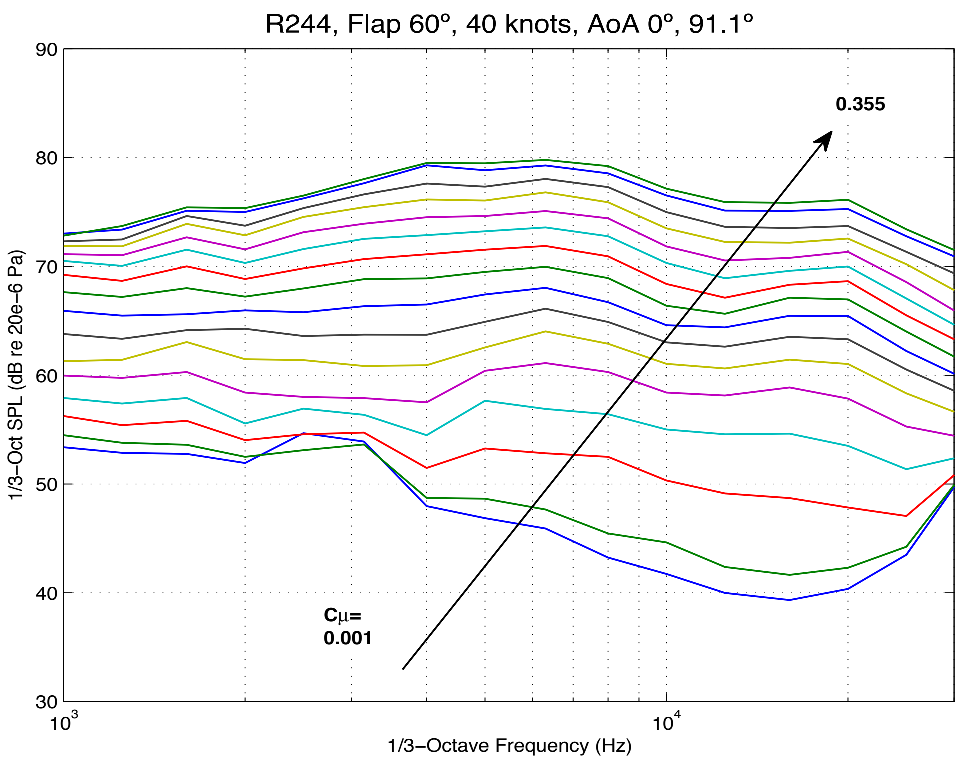

Figure 49. Trailing-edge only blowing Cμ sweep for α = 0º, 60º flap at 40 knots.

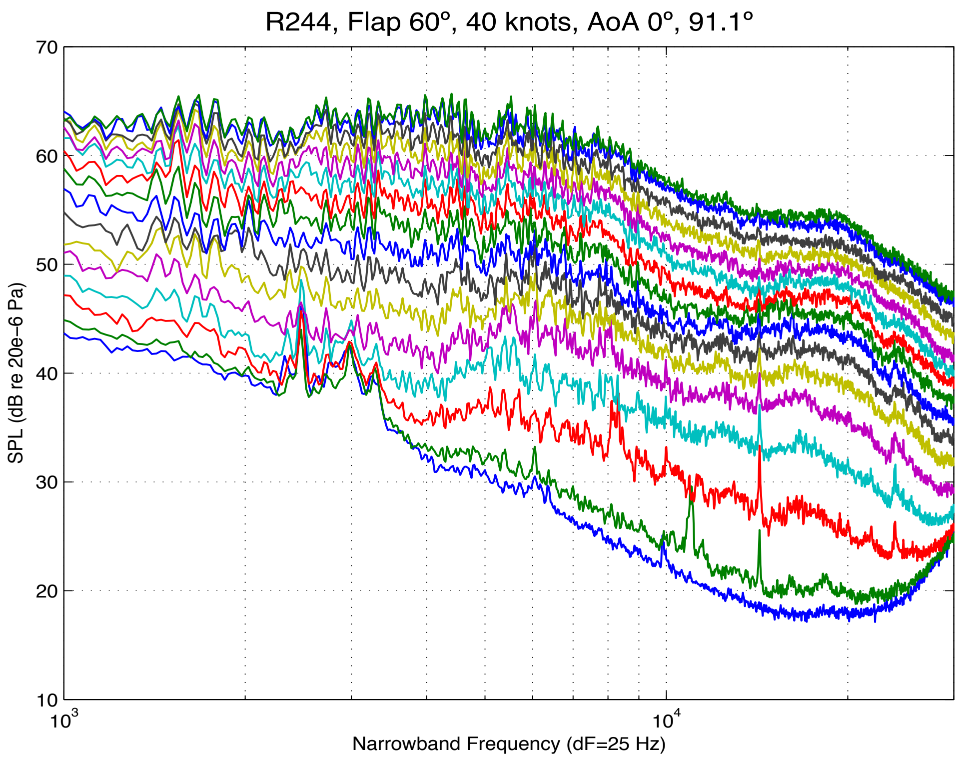

Figure 50. Narrowband plot of trailing-edge only blowing Cμ sweep for α = 0º, 60º flap at 40 knots.

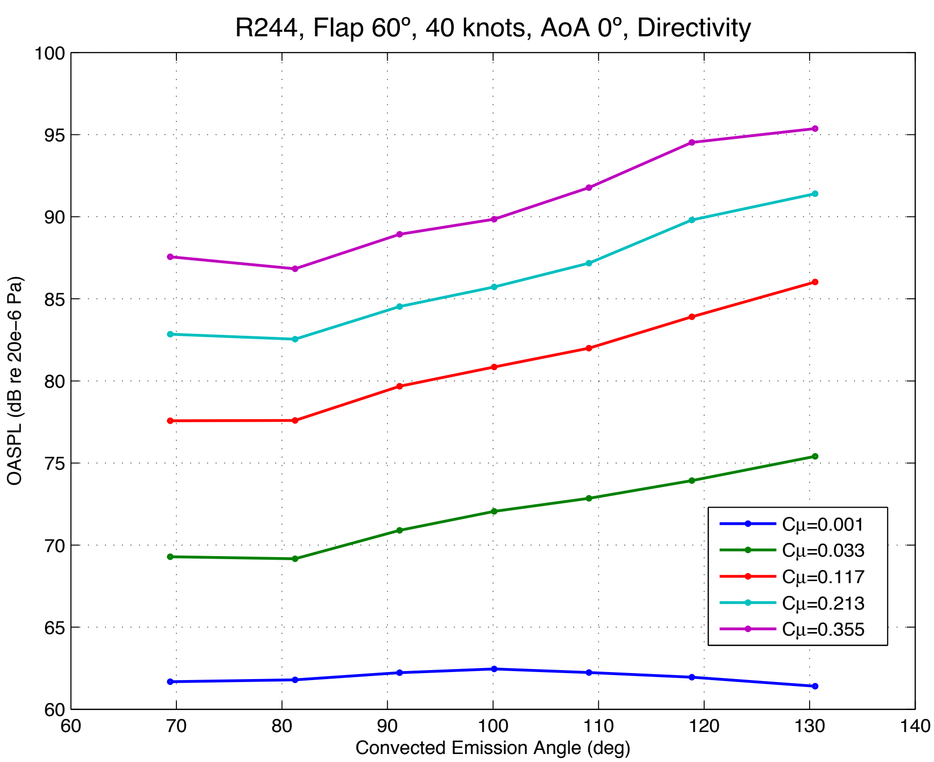

Figure 51. Directivity plot of trailing-edge only blowing Cμ sweep for α = 0º, 60º flap at 40 knots.

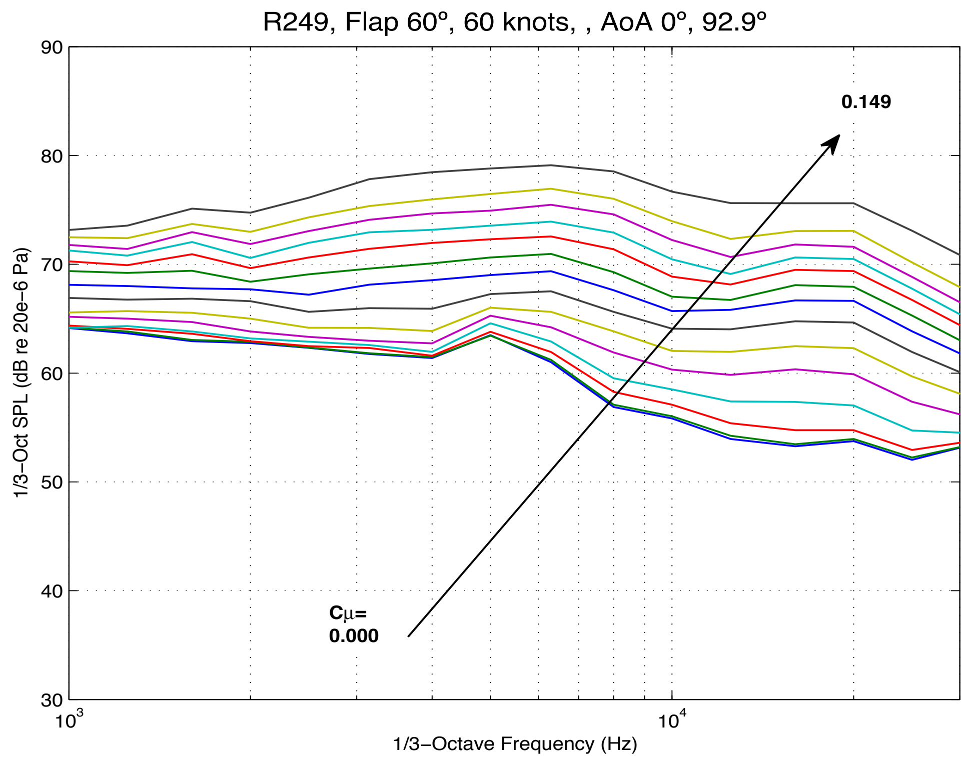

Figure 52. Trailing-edge only blowing Cμ sweep for α = 0º, 60º flap at 60 knots.

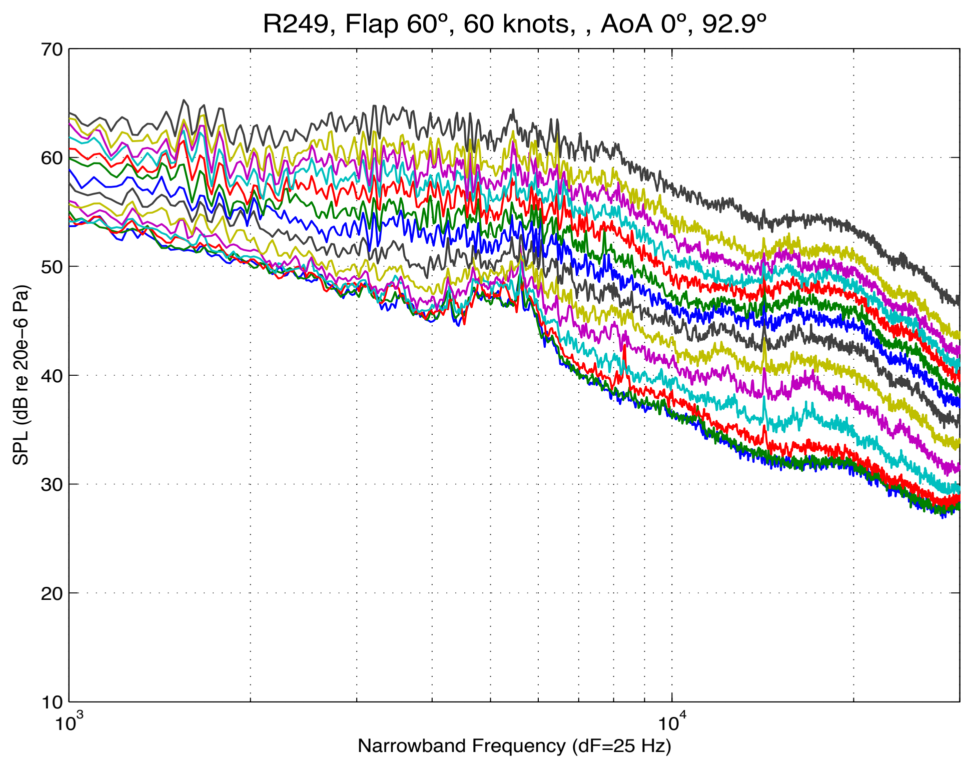

Figure 53. Narrowband plot of trailing-edge only blowing Cμ sweep for α = 0º, 60º flap at 60 knots.

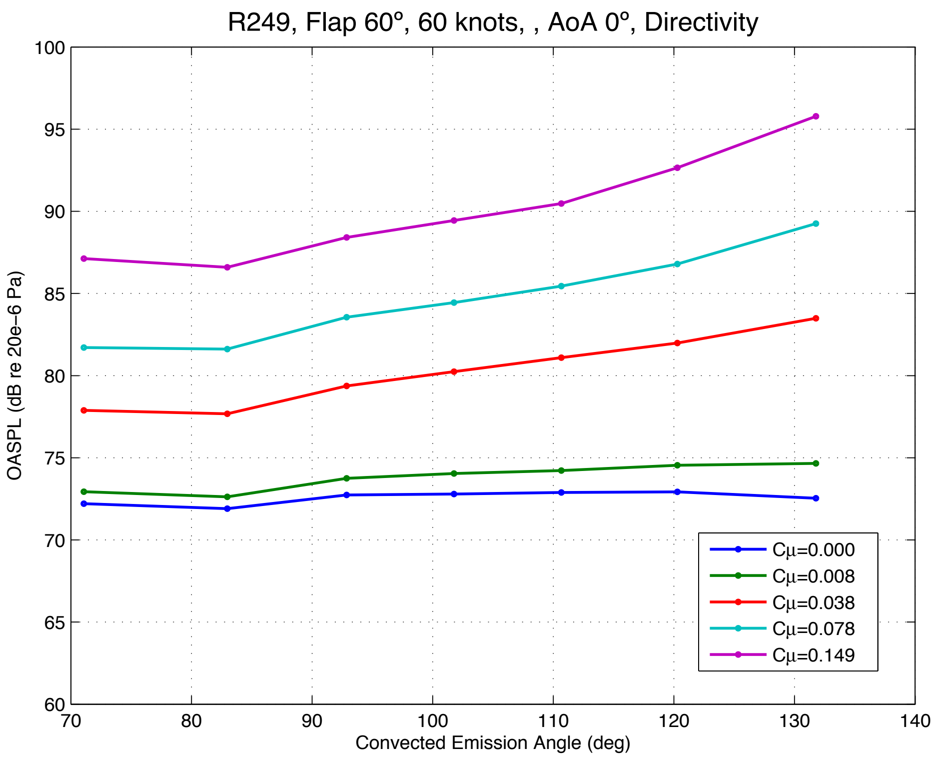

Figure 54. Directivity of trailing-edge only blowing Cμ sweep for α = 0º, 60º flap at 60 knots.

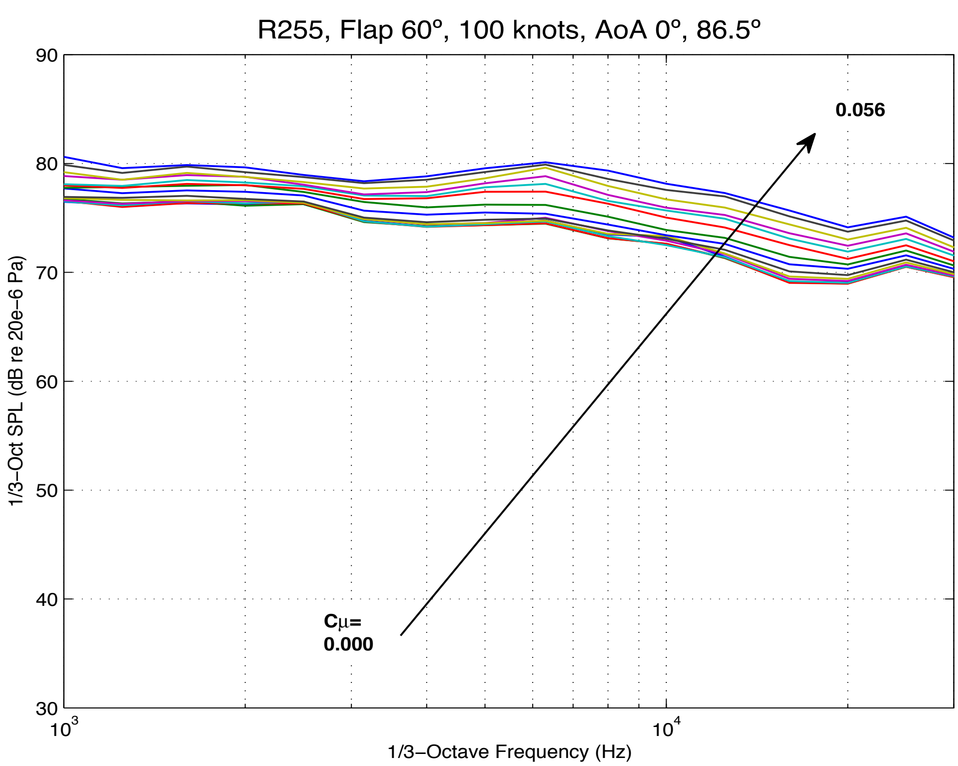

Figure 55. Trailing-edge only blowing Cμ sweep for α = 0º, 60º flap at 100 knots.

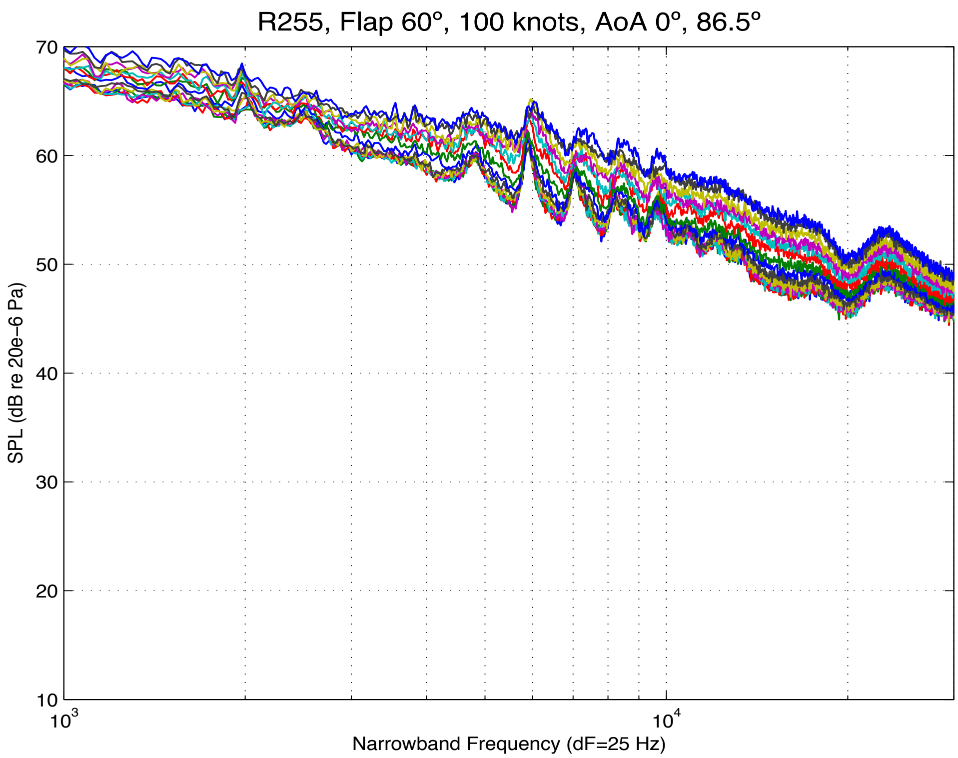

Figure 56. Narrowband plot of trailing-edge only blowing Cμ sweep for α = 0º, 60º flap at 100 knots.

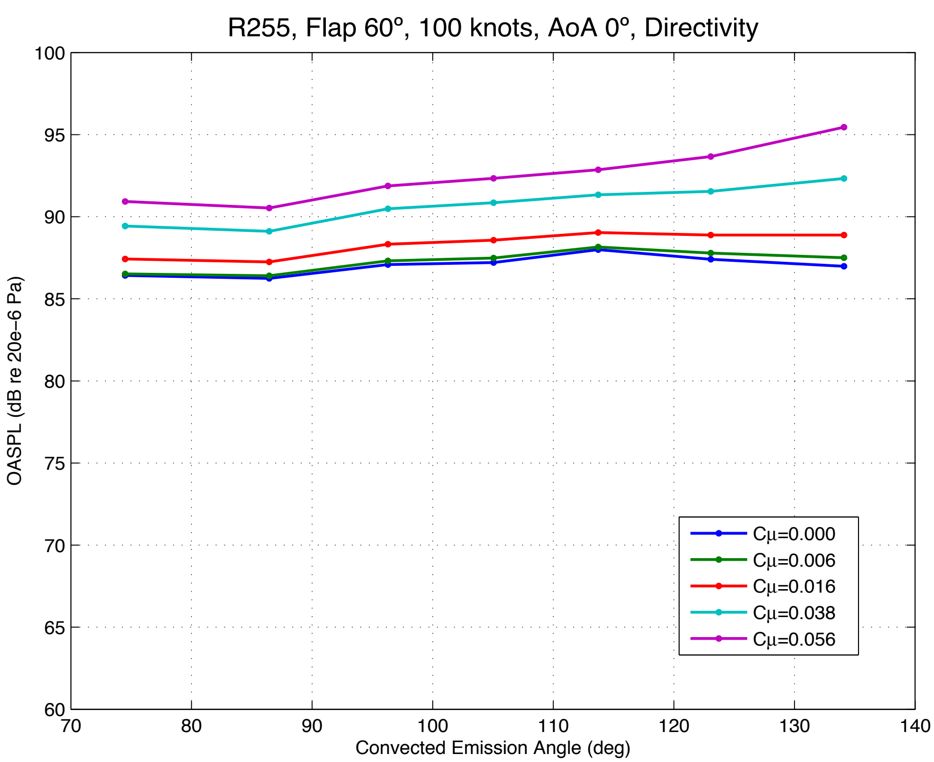

Figure 57. Directivity of trailing-edge only blowing Cμ sweep for α = 0º, 60º flap at 100 knots.

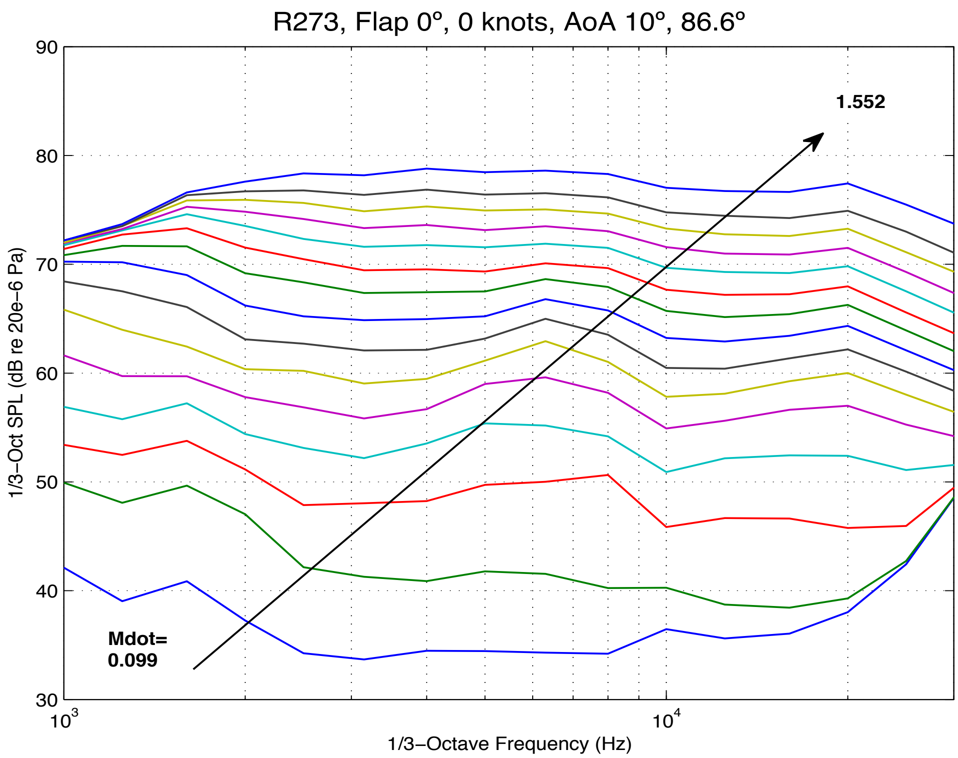

Figure 58. Trailing-edge only blowing Cμ sweep for α = 10°, 0° flap at 0 knots.

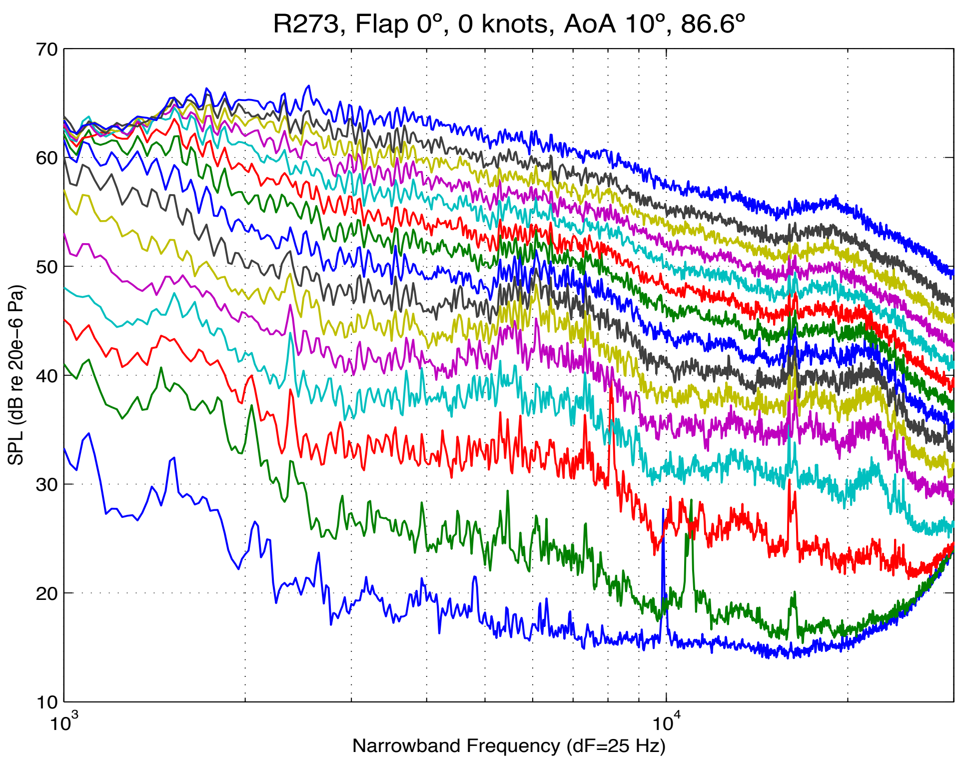

Figure 59. Narrowband plot of trailing-edge only blowing Cμ sweep for α = 10°, 0° flap at 0 knots.

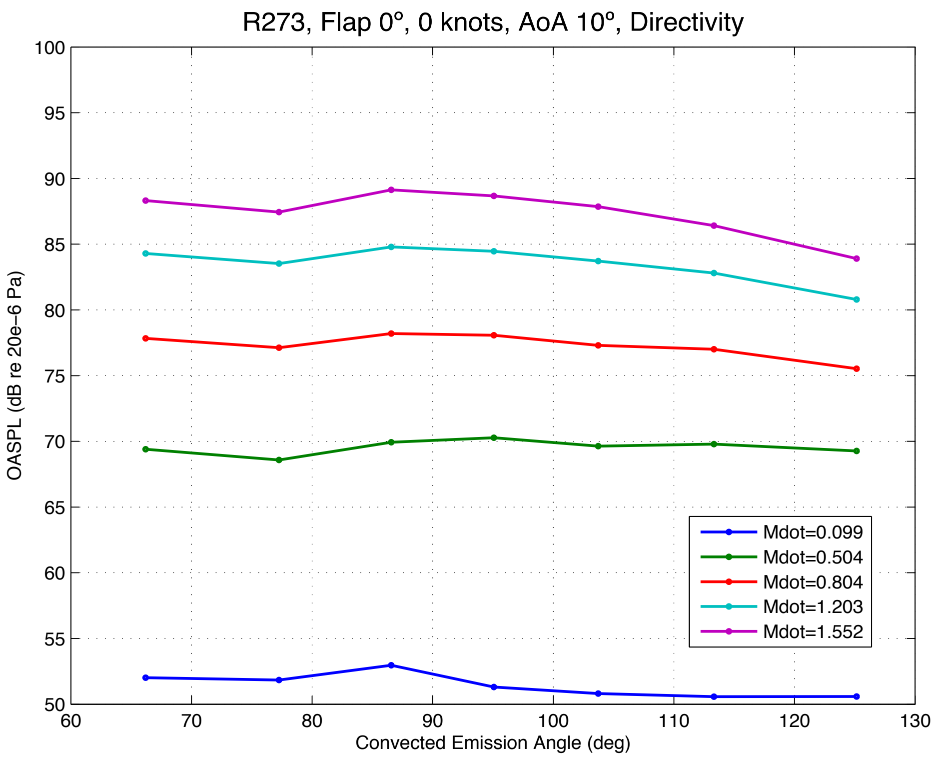

Figure 60. Directivity of trailing-edge only blowing Cμ sweep for α = 10°, 0° flap at 0 knots.

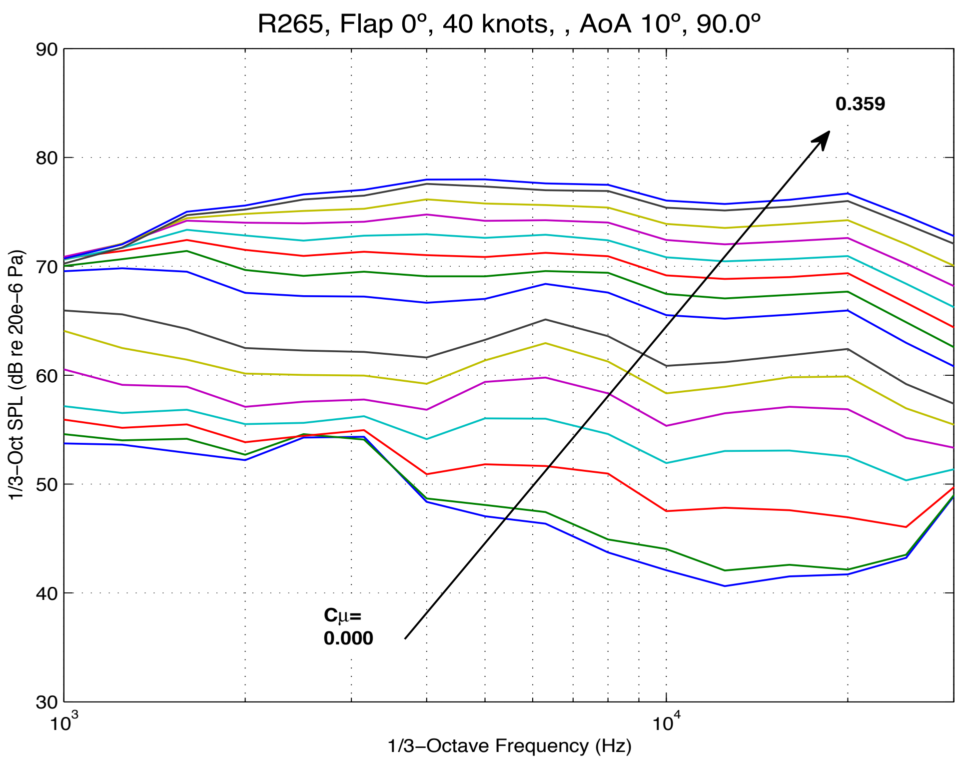

Figure 61. Trailing-edge only blowing Cμ sweep for α = 10°, 0° flap at 40 knots.

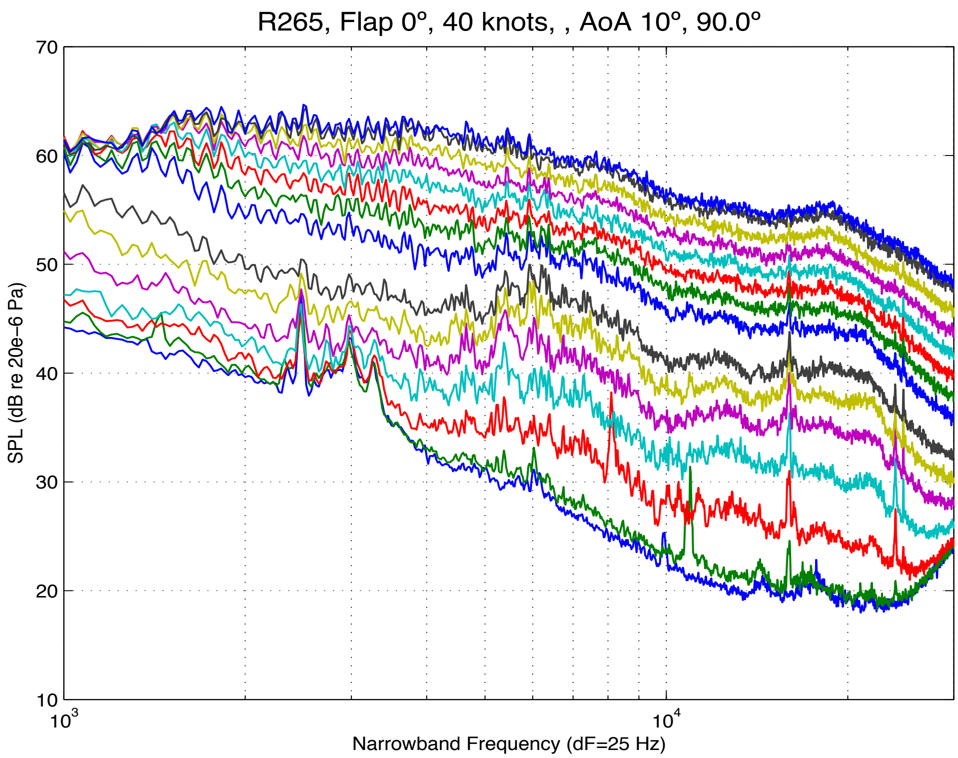

Figure 62. Narrowband plot of trailing-edge only blowing Cμ sweep for α = 10º, 0º flap at 40 knots.

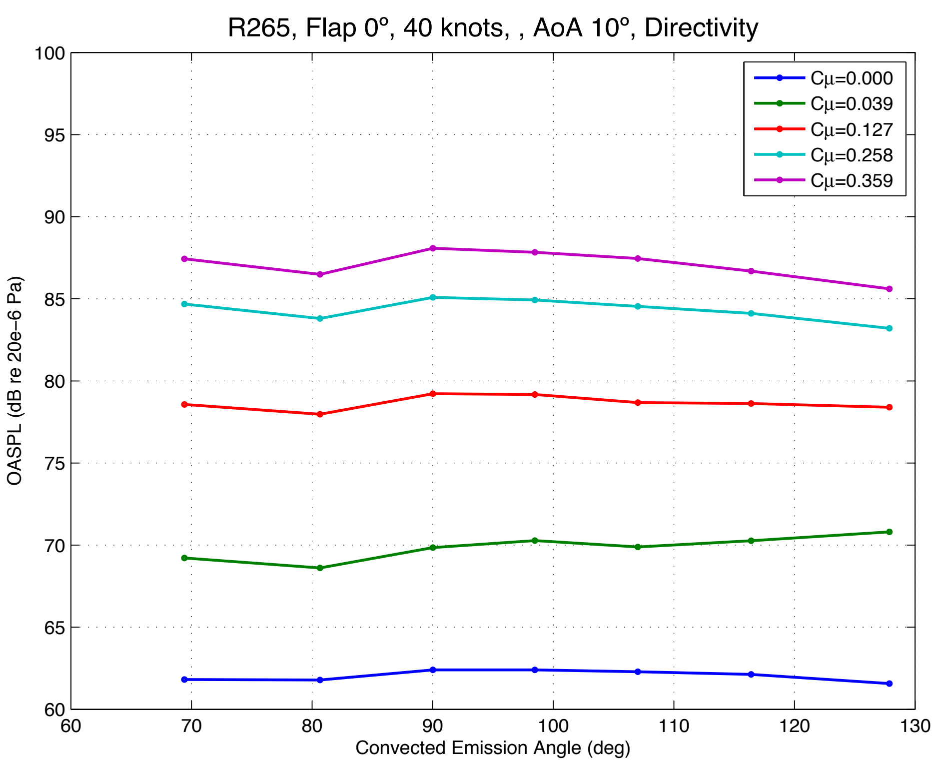

Figure 63. Directivity of trailing-edge only blowing Cμ sweep for α = 10º, 0º flap at 40 knots.

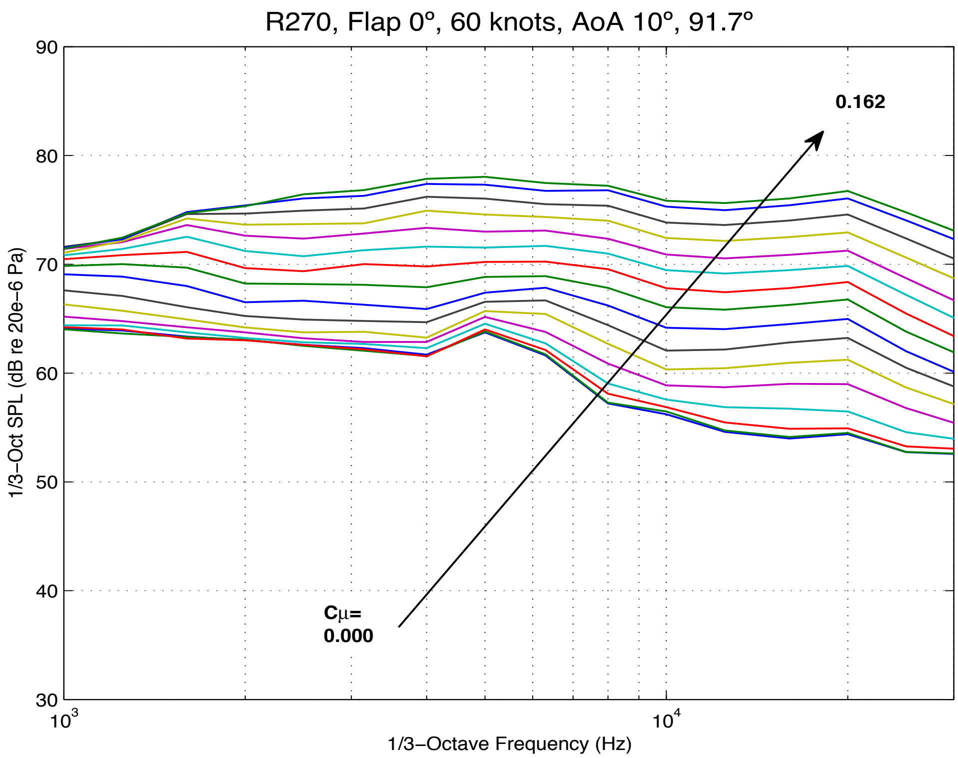

Figure 64. Trailing-edge only blowing Cμ sweep for α = 10º, 0º flap at 60 knots.

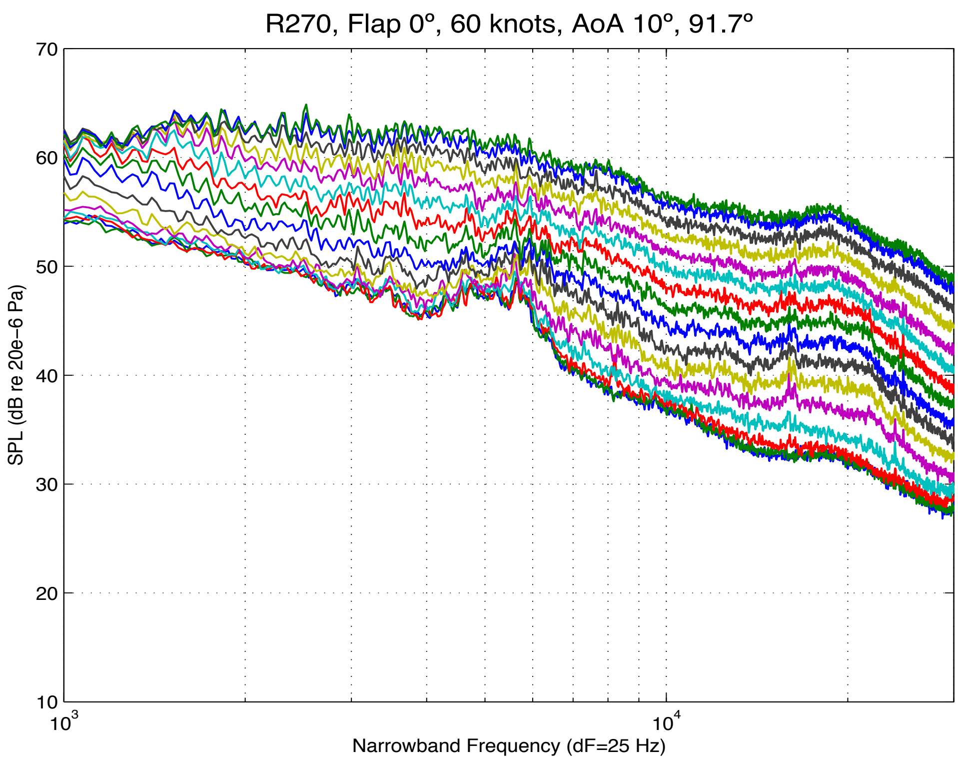

Figure 65. Narrowband plot of trailing-edge only blowing Cμ sweep for α = 10º, 0º flap at 60 knots.

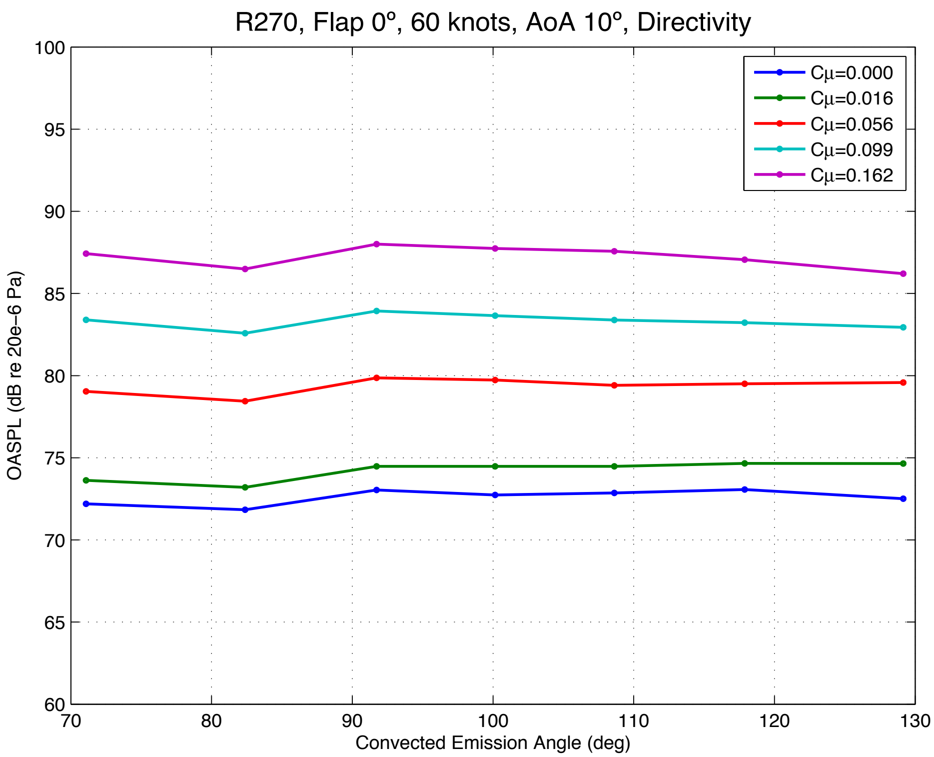

Figure 66. Directivity of trailing-edge only blowing Cμ sweep for α = 10°, 0° flap at 60 knots.

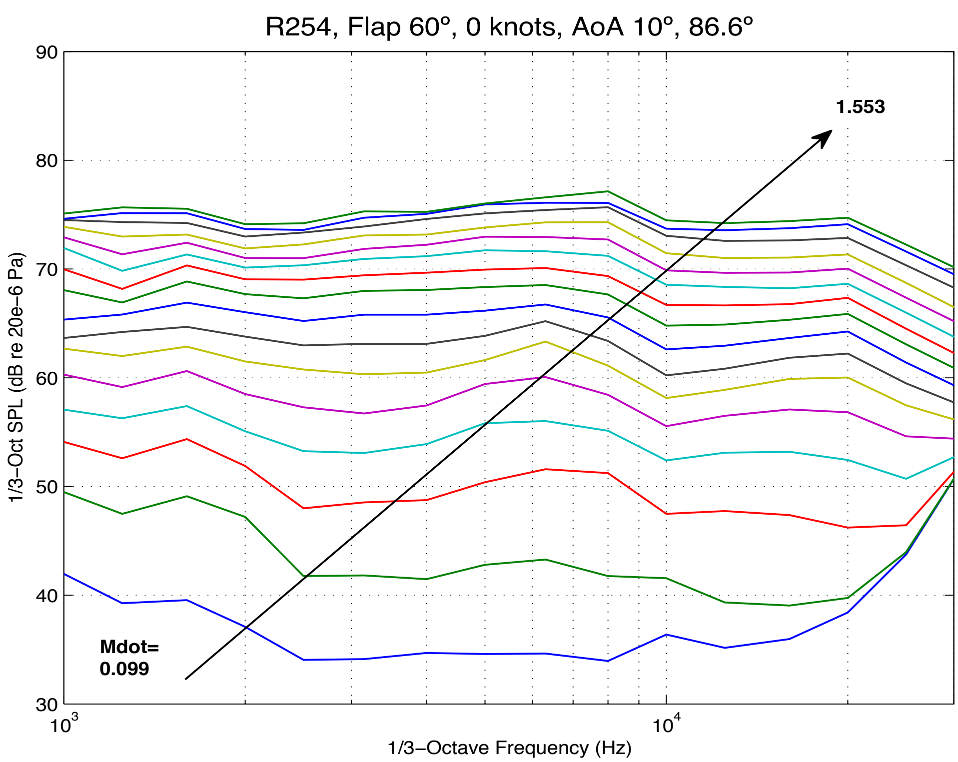

Figure 67. Trailing-edge only blowing Cμ sweep for α = 10°, 60° flap at 0 knots.

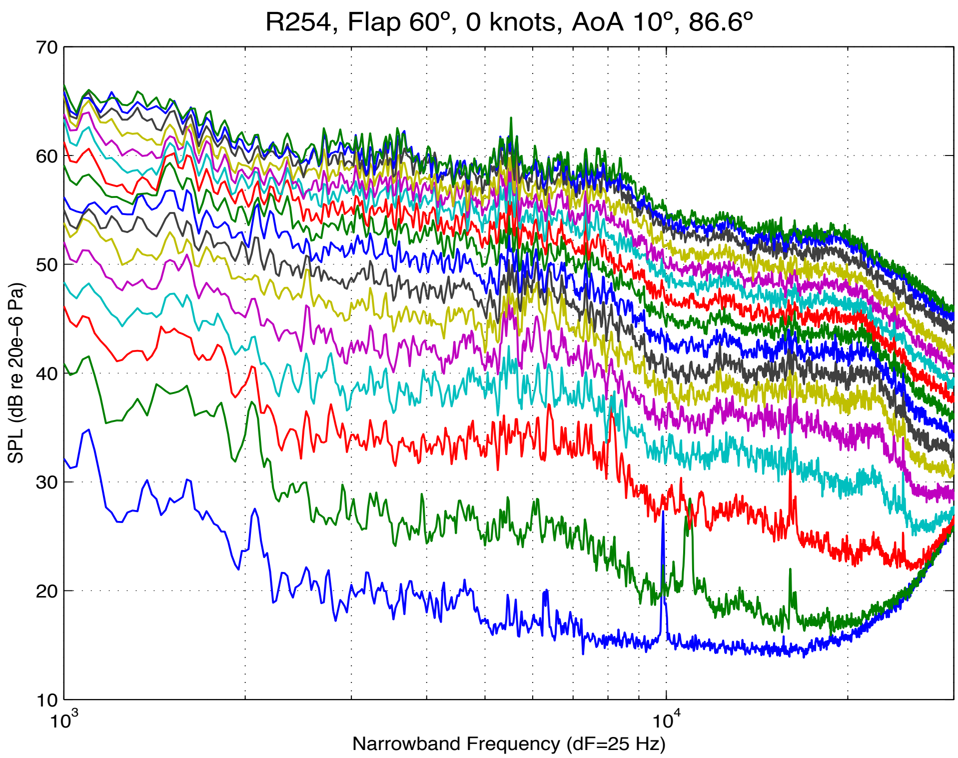

Figure 68. Narrowband plot of trailing-edge only blowing Cμ sweep for α = 10°, 60° flap at 0 knots.

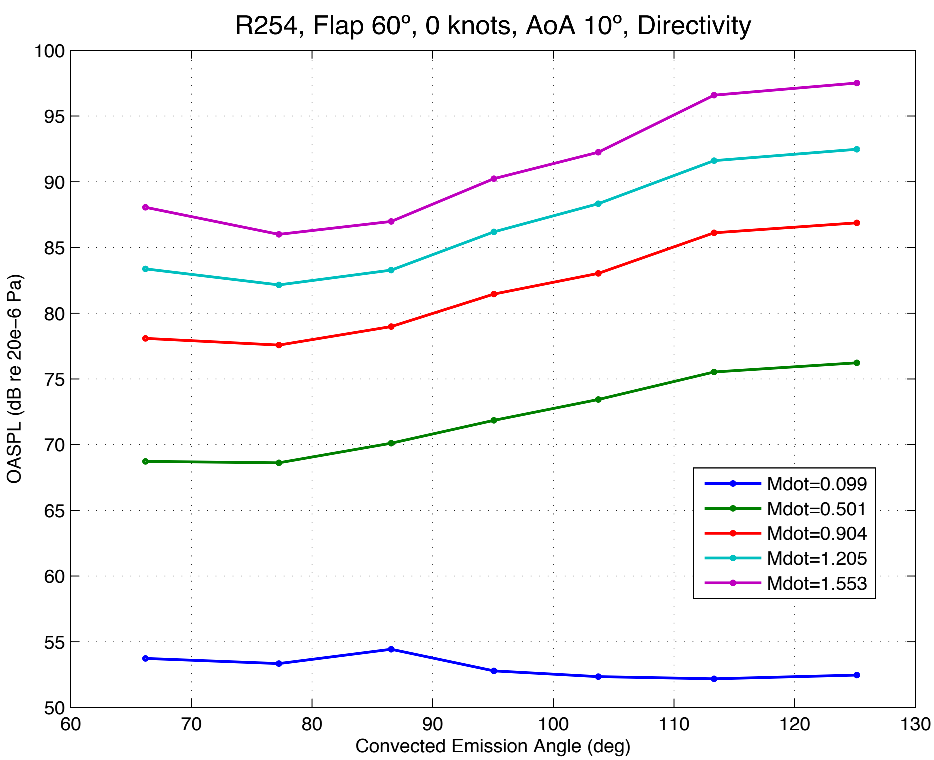

Figure 69. Directivity of trailing-edge only blowing Cμ sweep for α = 10°, 60° flap at 0 knots.

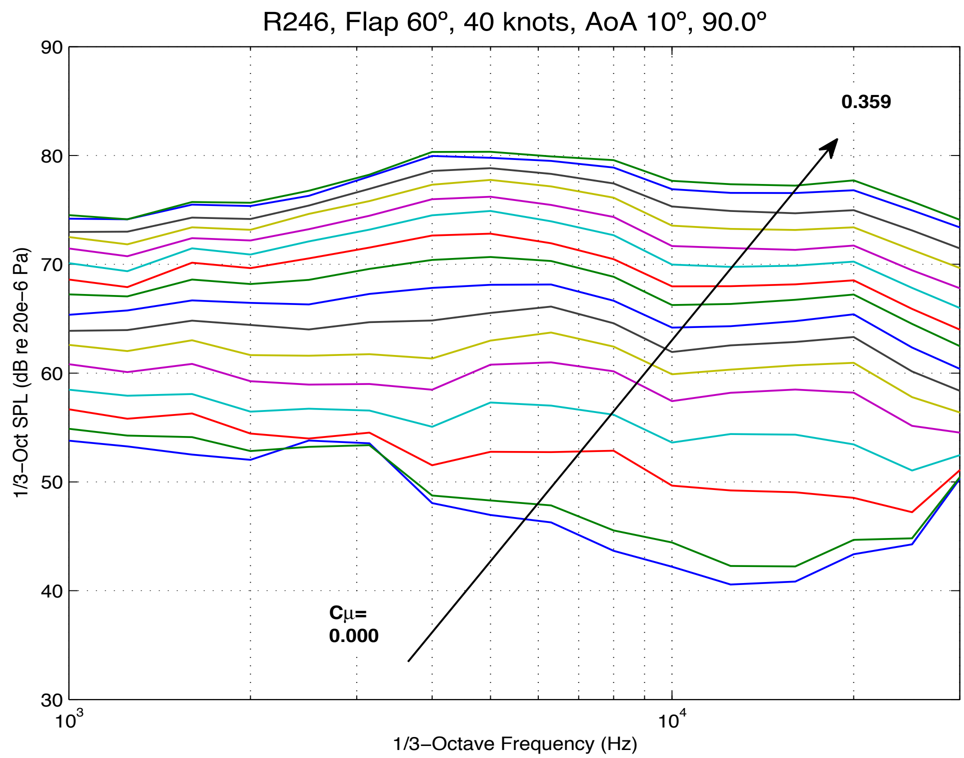

Figure 70. Trailing-edge only blowing Cμ sweep for α = 10º, 60º flap at 40 knots.

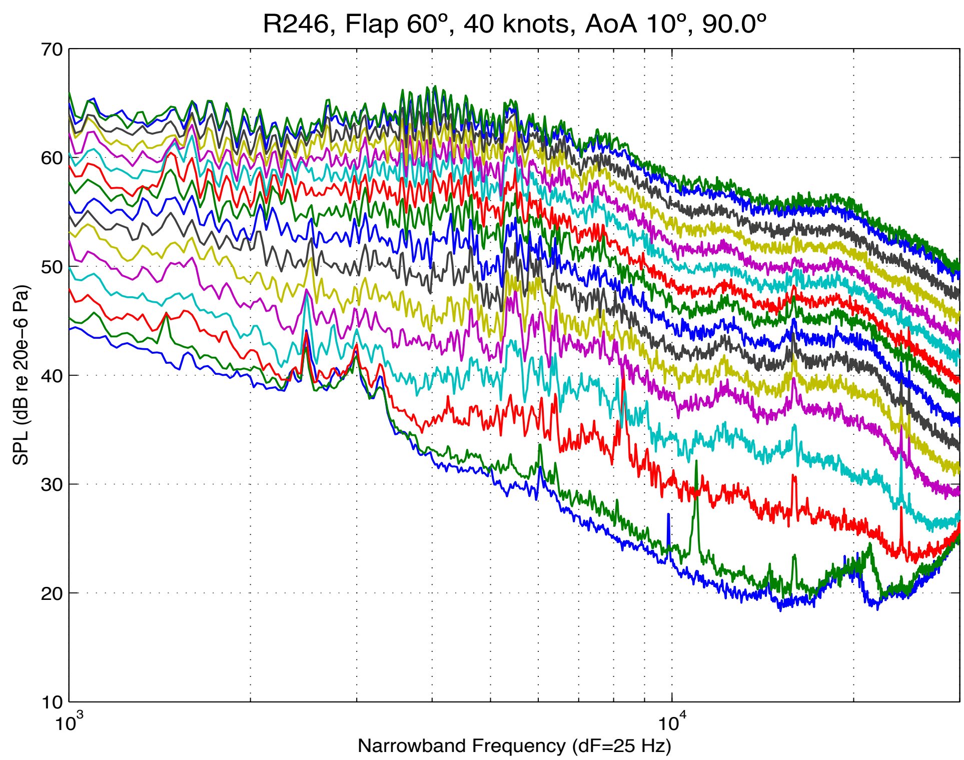

Figure 71. Narrowband plot of trailing-edge only blowing Cμ sweep for α = 10º, 60º flap at 40 knots.

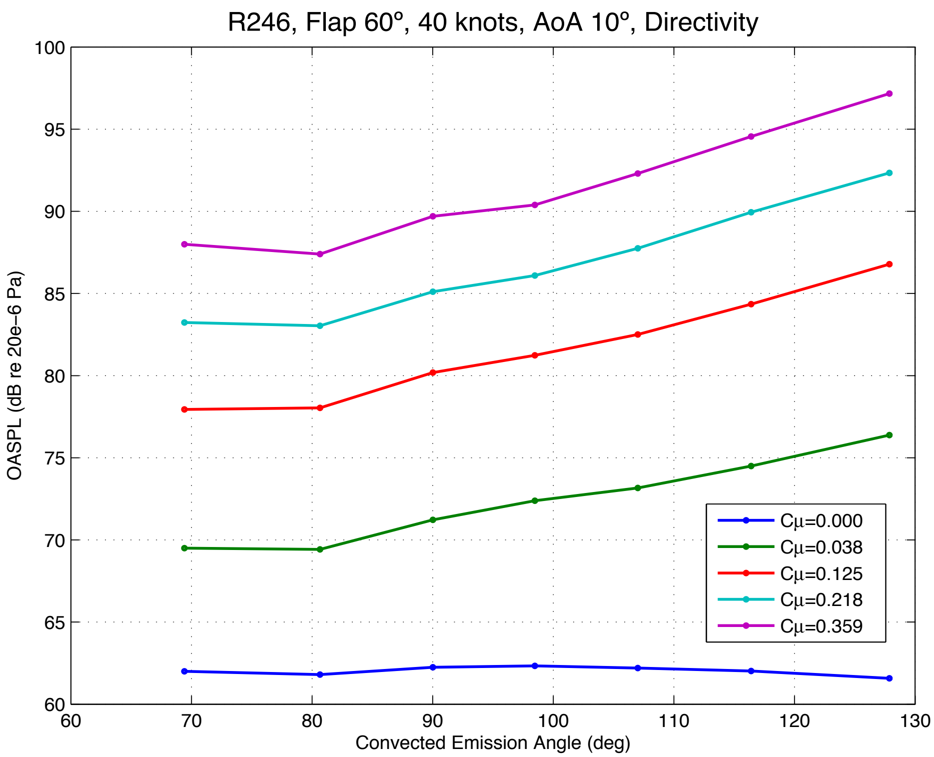

Figure 72. Directivity of trailing-edge only blowing Cμ sweep for α = 10º, 60º flap at 40 knots.

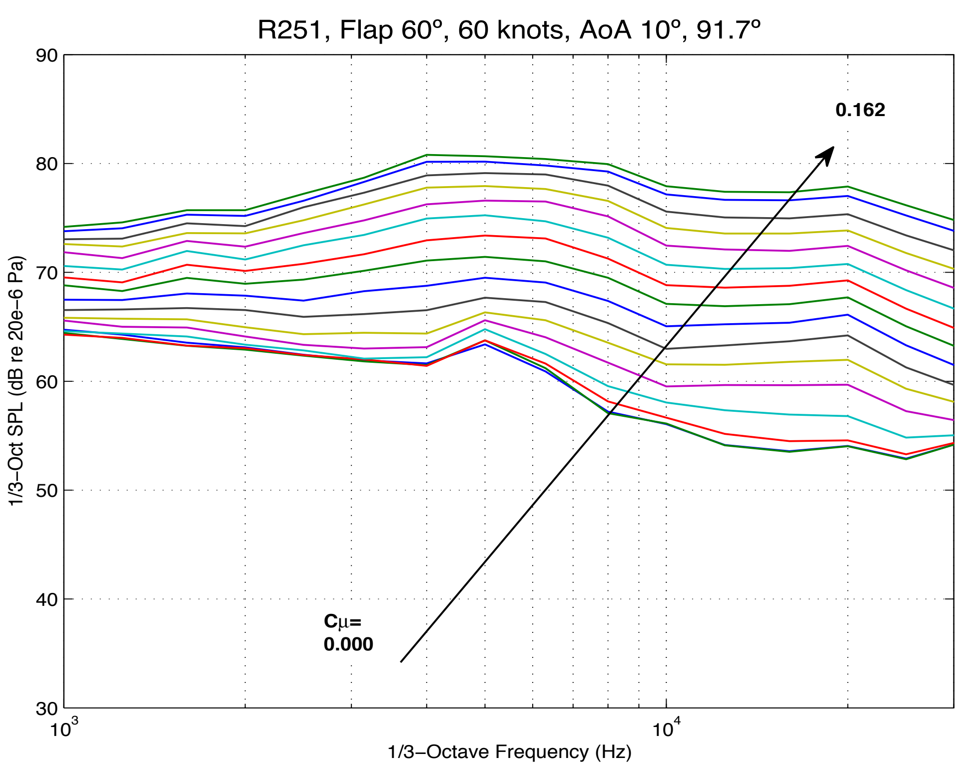

Figure 73. Trailing-edge only blowing Cμ sweep for α = 10º, 60º flap at 60 knots.

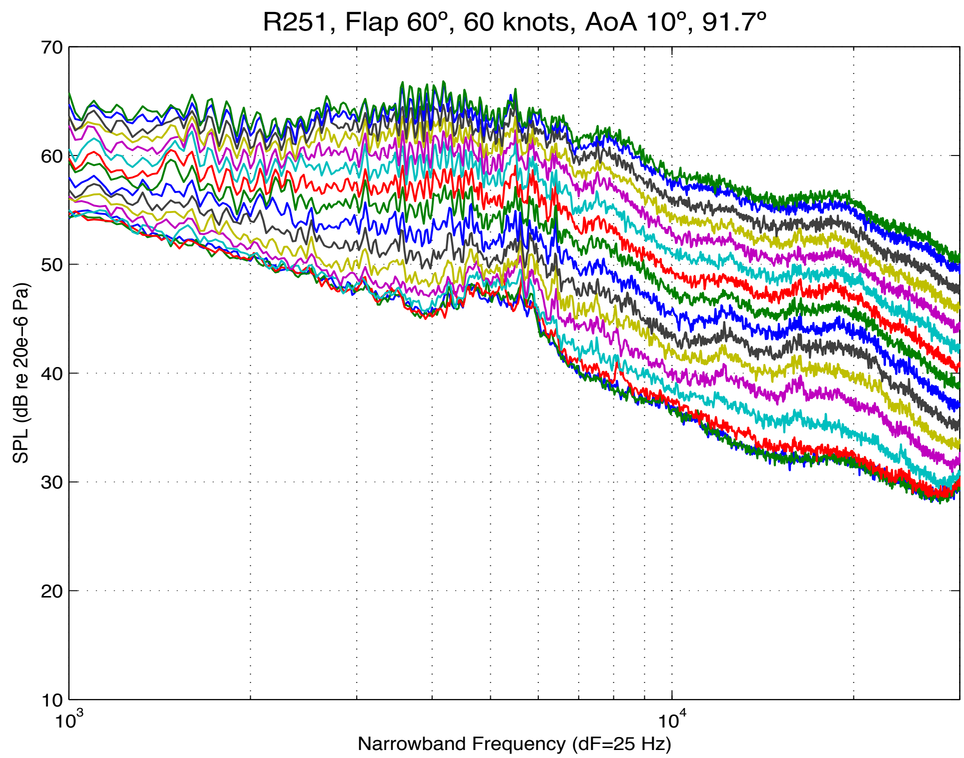

Figure 74. Narrowband plot of trailing-edge only blowing Cμ sweep for α = 10°, 60° flap at 60 knots.

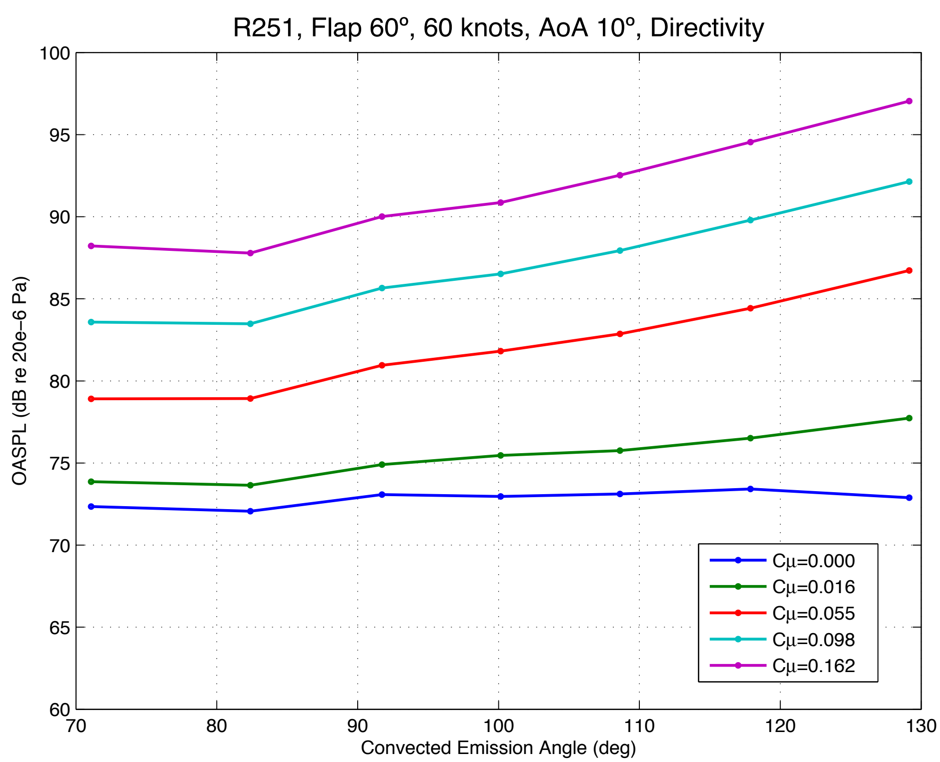

Figure 75. Directivity of trailing-edge only blowing Cμ sweep for α = 10°, 60° flap at 60 knots.

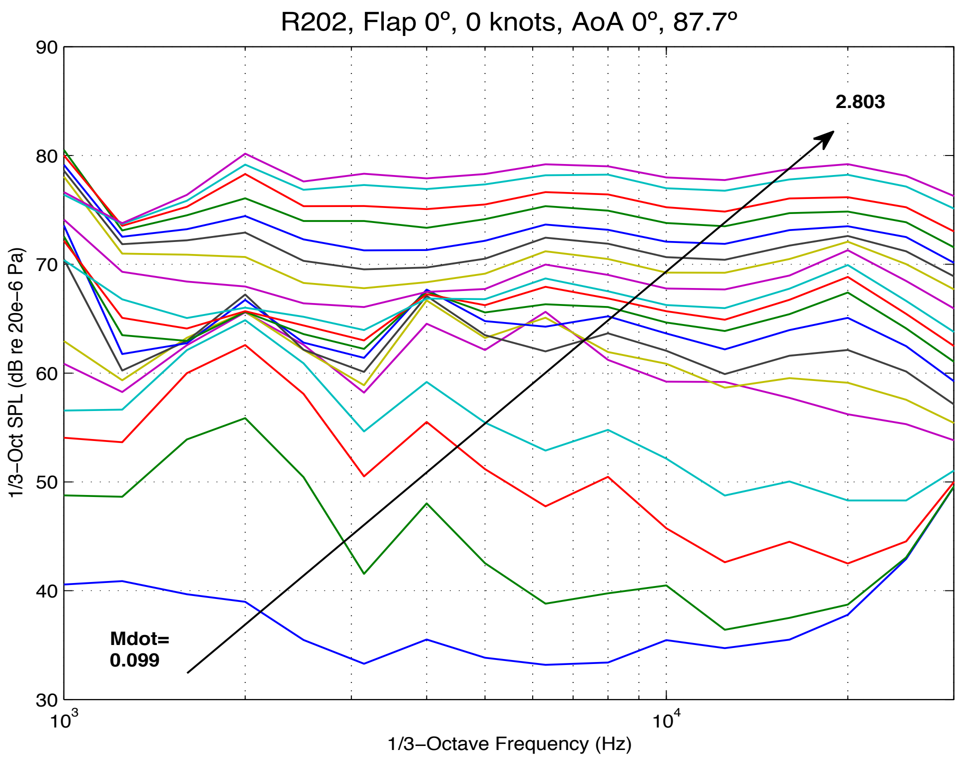

Figure 76. Trailing- and leading-edge Cμ sweep for α = 0º, 0º flap at 0 knots.

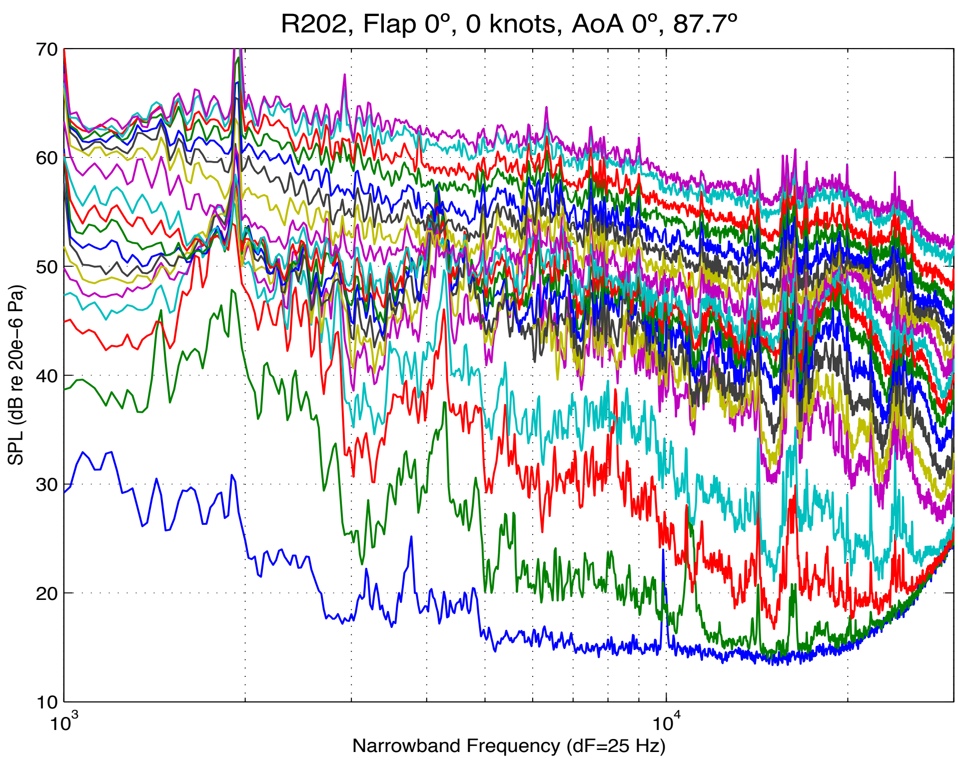

Figure 77. Narrowband plot of trailing- and leading-edge Cμ sweep for α = 0º, 0º flap at 0 knots.

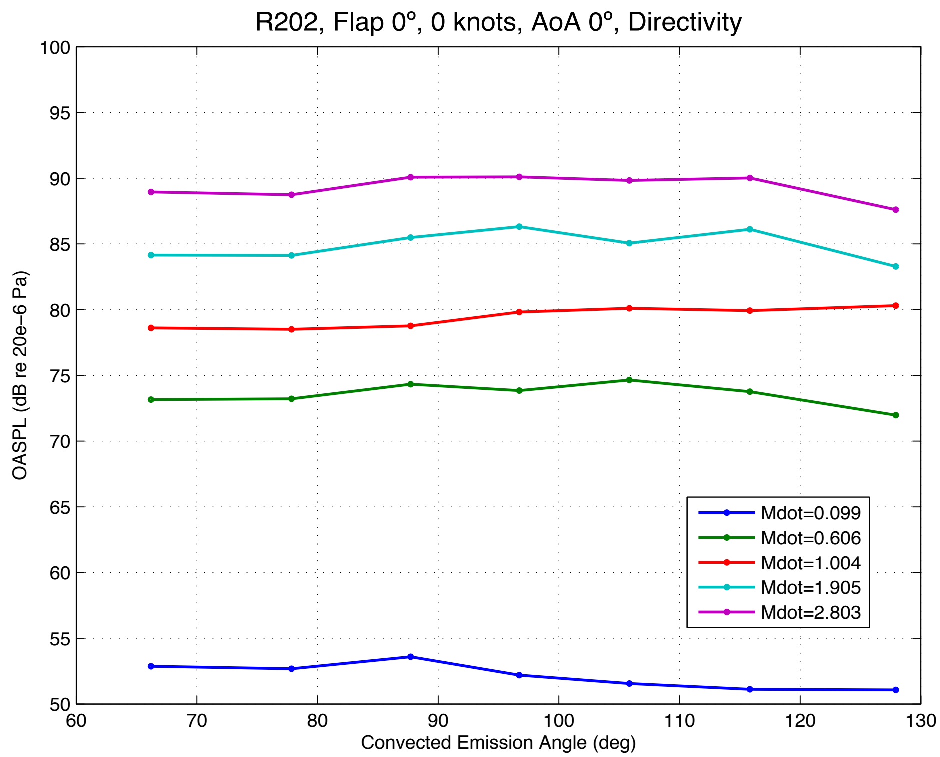

Figure 78. Directivity of trailing- and leading-edge Cμ sweep for α = 0º, 0º flap at 0 knots.

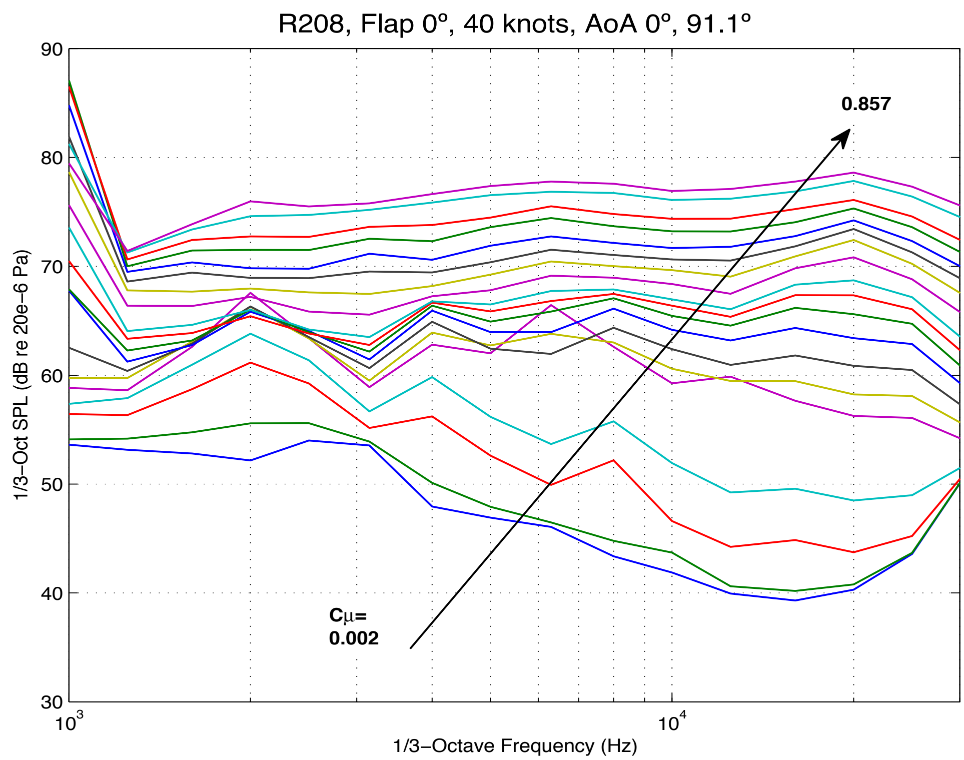

Figure 79. Trailing- and leading-edge e Cμ sweep for α = 0º, 0º flap at 40 knots.

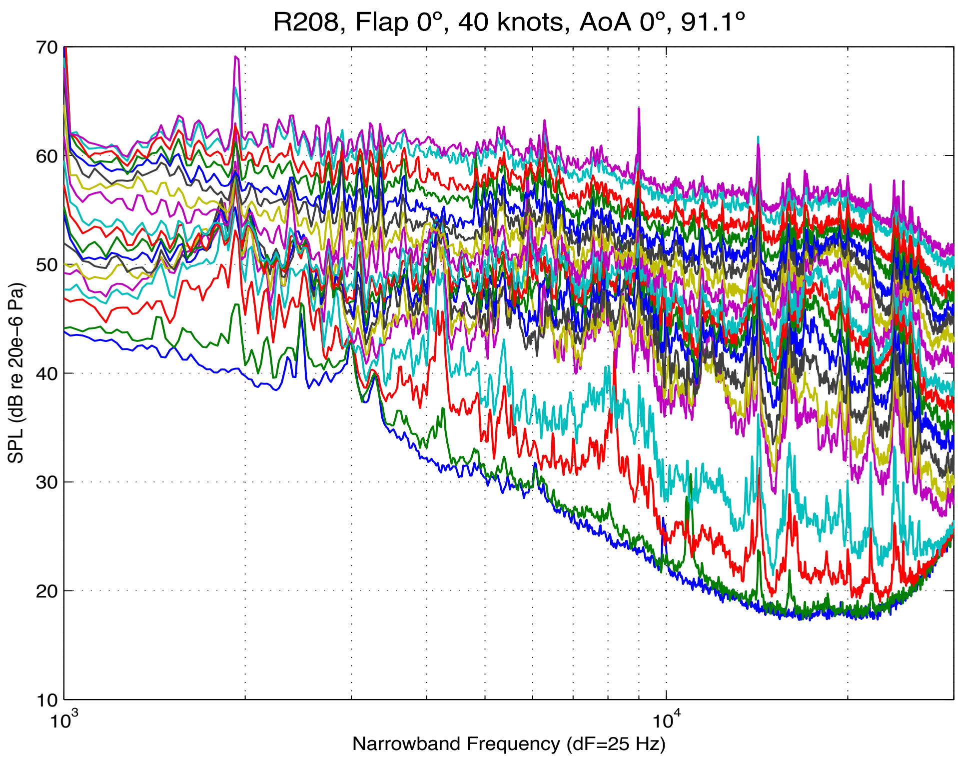

Figure 80. Narrowband plot of trailing- and leading-edge e Cμ sweep for α = 0º, 0º flap at 40 knots.

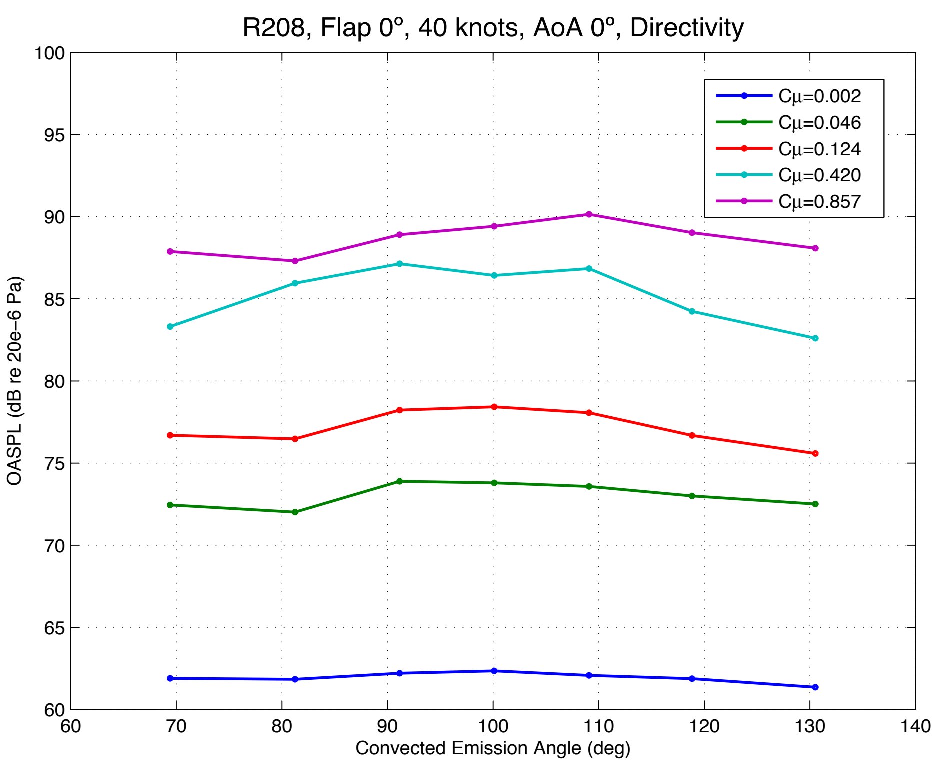

Figure 81. Directivity of trailing- and leading-edge e Cμ sweep for α = 0º, 0º flap at 40 knots.

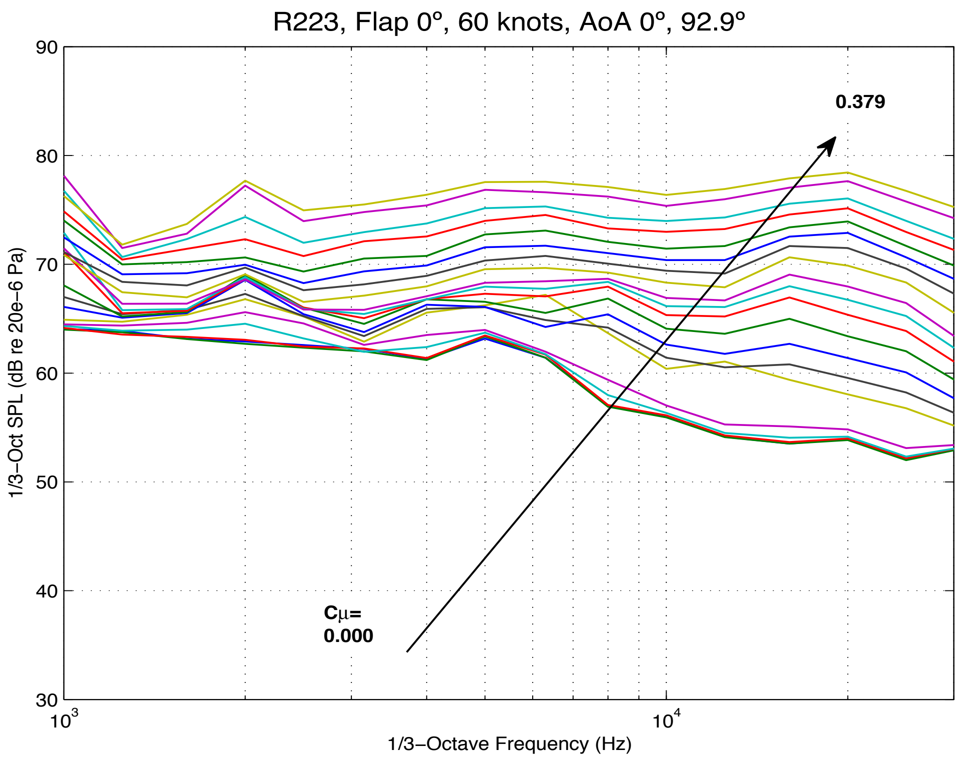

Figure 82. Trailing- and leading-edge Cμ sweep for α = 0º, 0º flap at 60 knots.

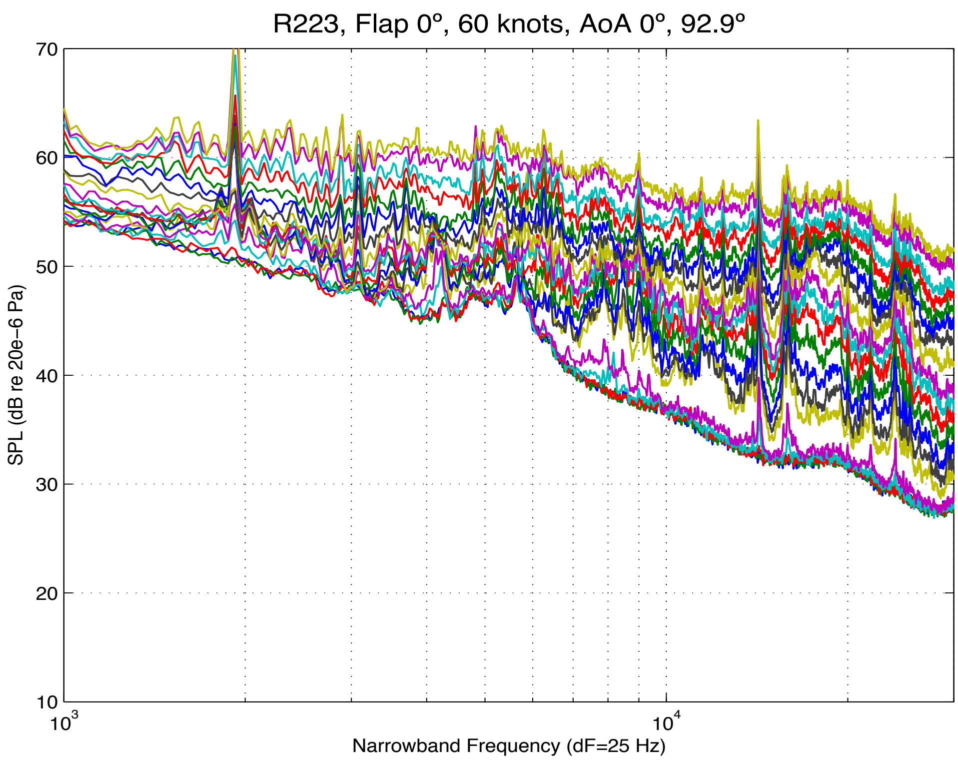

Figure 83. Narrowband plot of trailing- and leading-edge Cμ sweep for α = 0º, 0º flap at 60 knots.

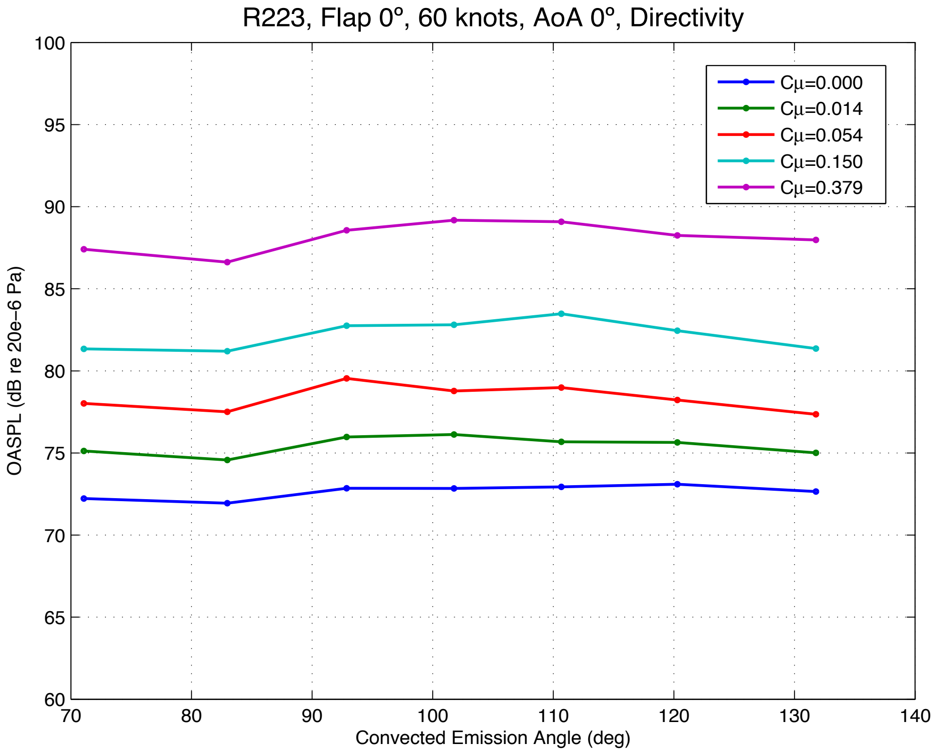

Figure 84. Directivity of trailing- and leading-edge Cμ sweep for α = 0°, 0° flap at 60 knots.

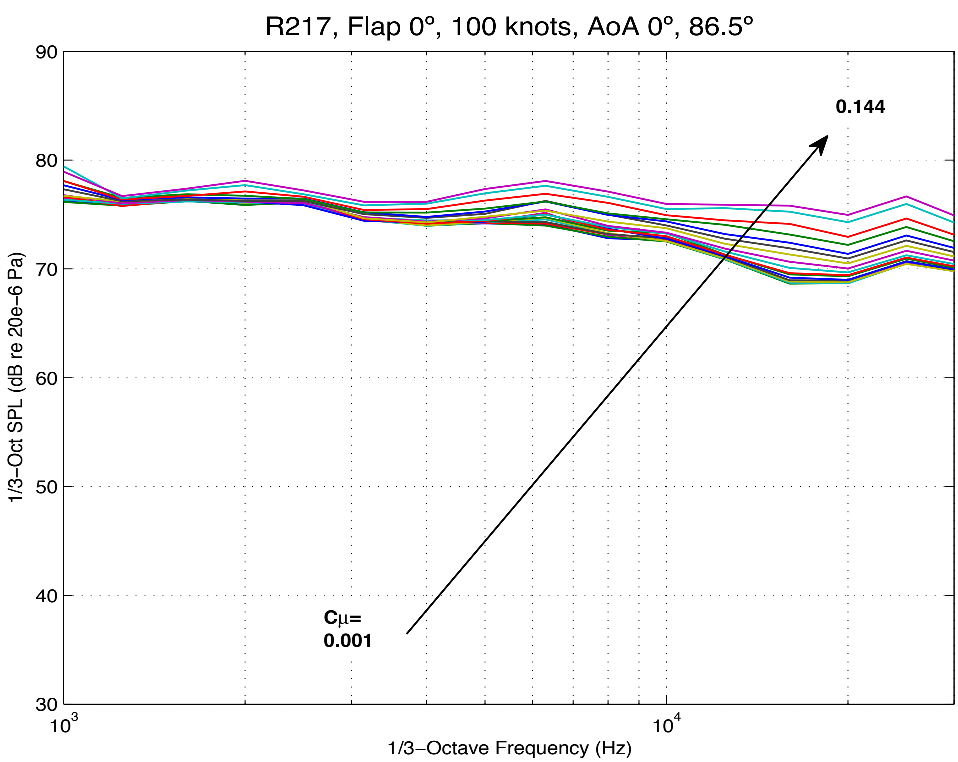

Figure 85. Trailing- and leading-edge Cμ sweep for α = 0°, 0° flap at 100 knots.

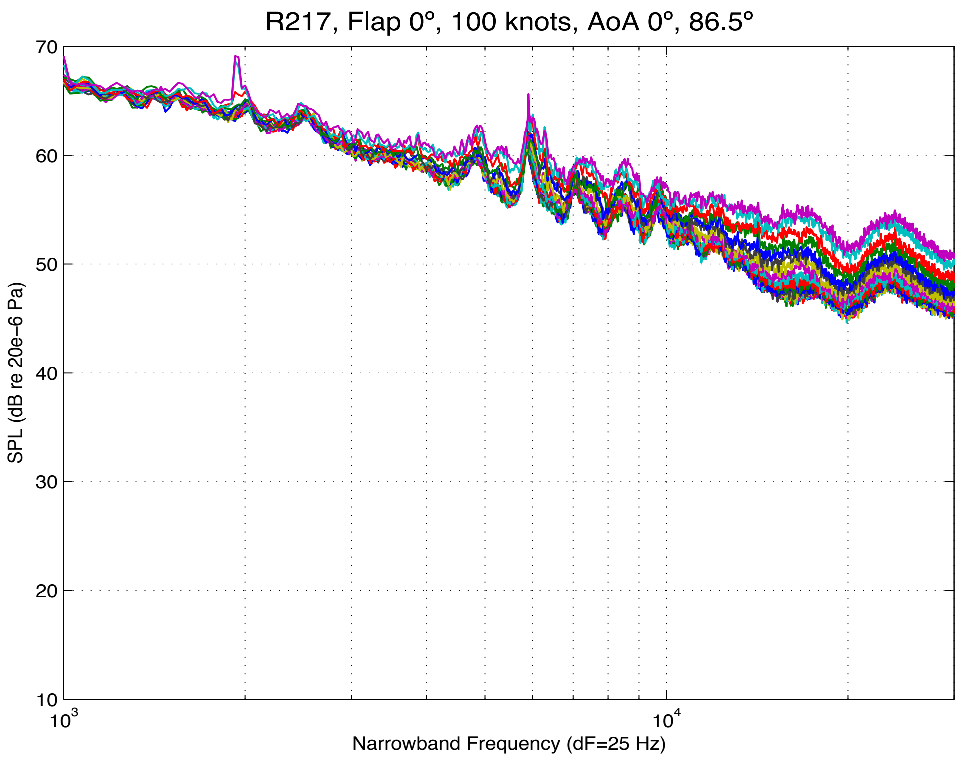

Figure 86. Narrowband plot of trailing- and leading-edge Cμ sweep for α = 0°, 0° flap at 100 knots.

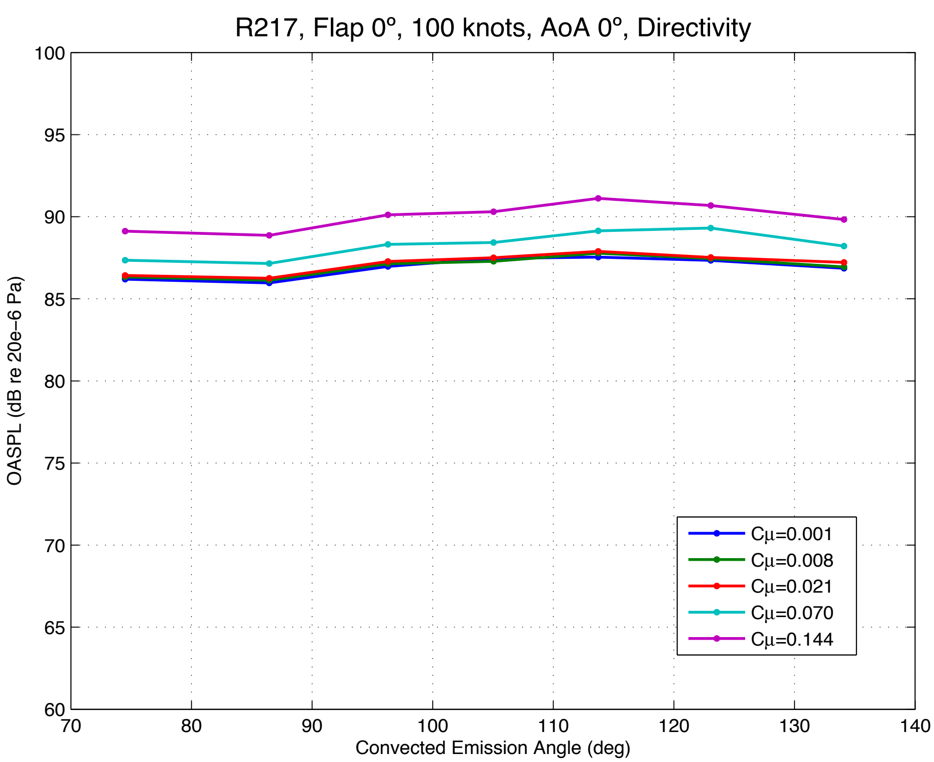

Figure 87. Directivity of trailing- and leading-edge Cμ sweep for α = 0°, 0° flap at 100 knots.

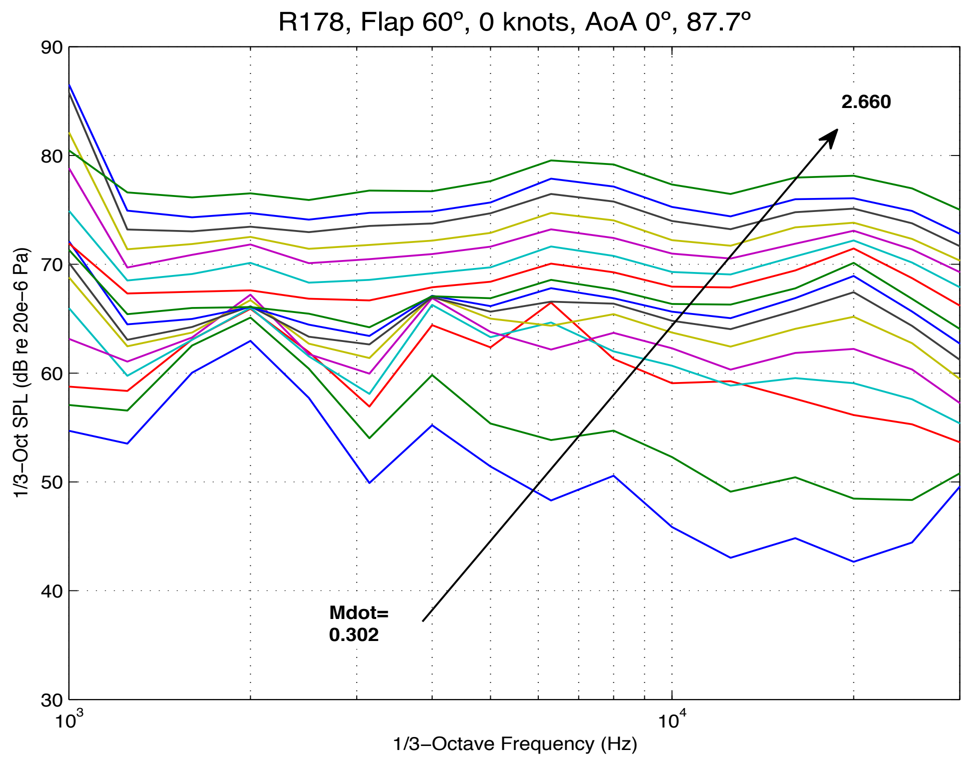

Figure 88. Trailing- and leading-edge Cμ sweep for α = 0º, 60º flap at 0 knots.

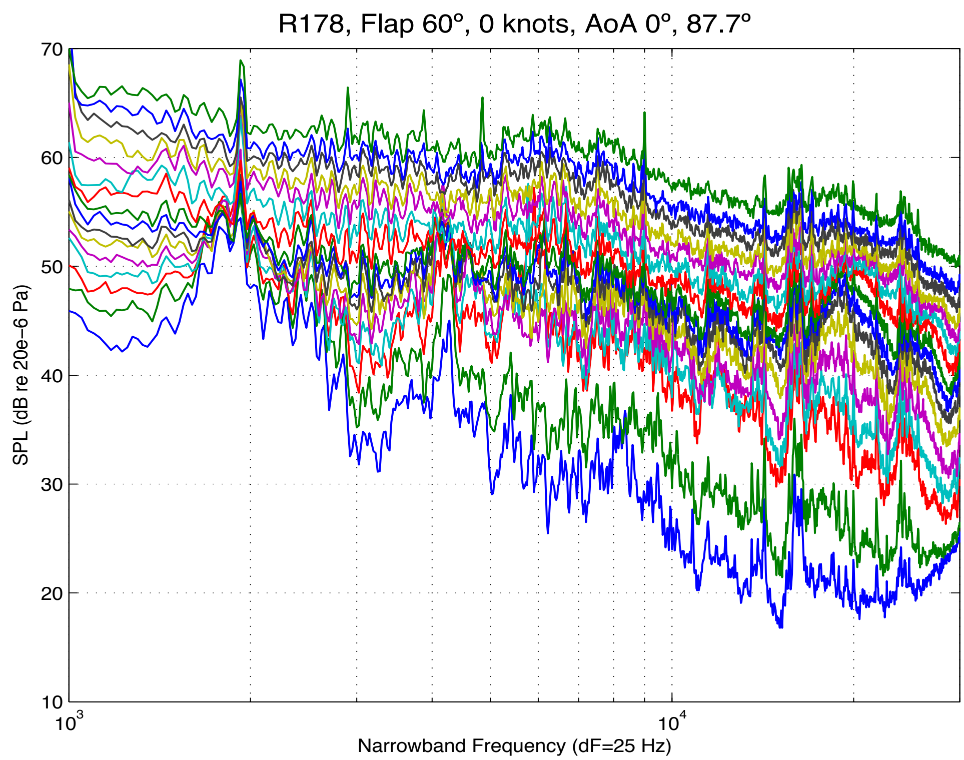

Figure 89. Narrowband plot of trailing- and leading-edge Cμ sweep for α = 0º, 60º flap at 0 knots.

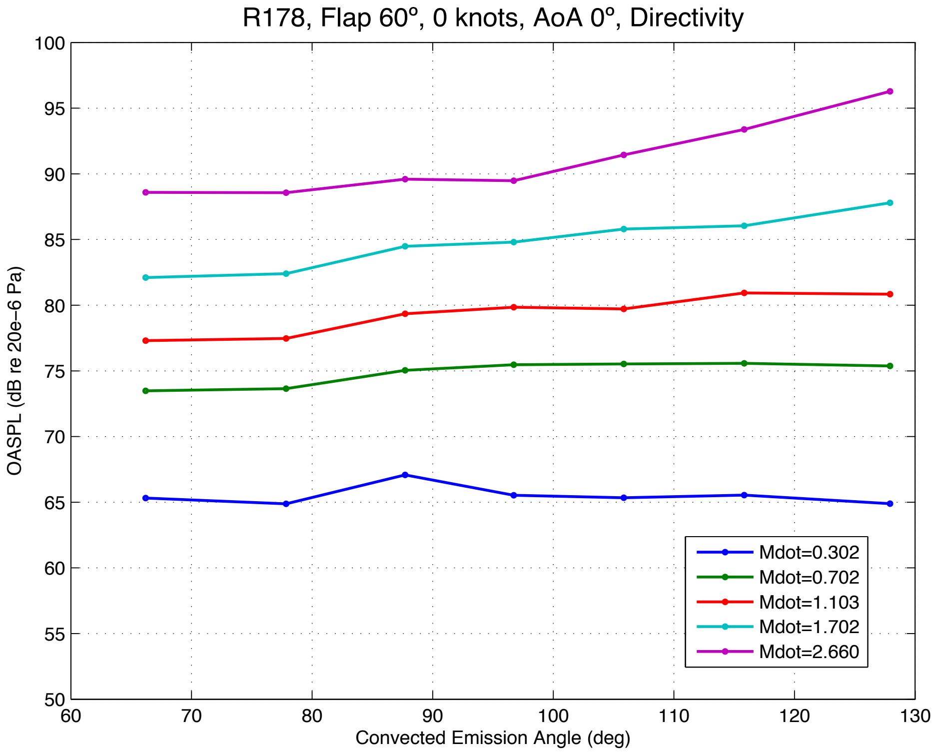

Figure 90. Directivity of trailing- and leading-edge Cμ sweep for α = 0°, 60° flap at 0 knots.

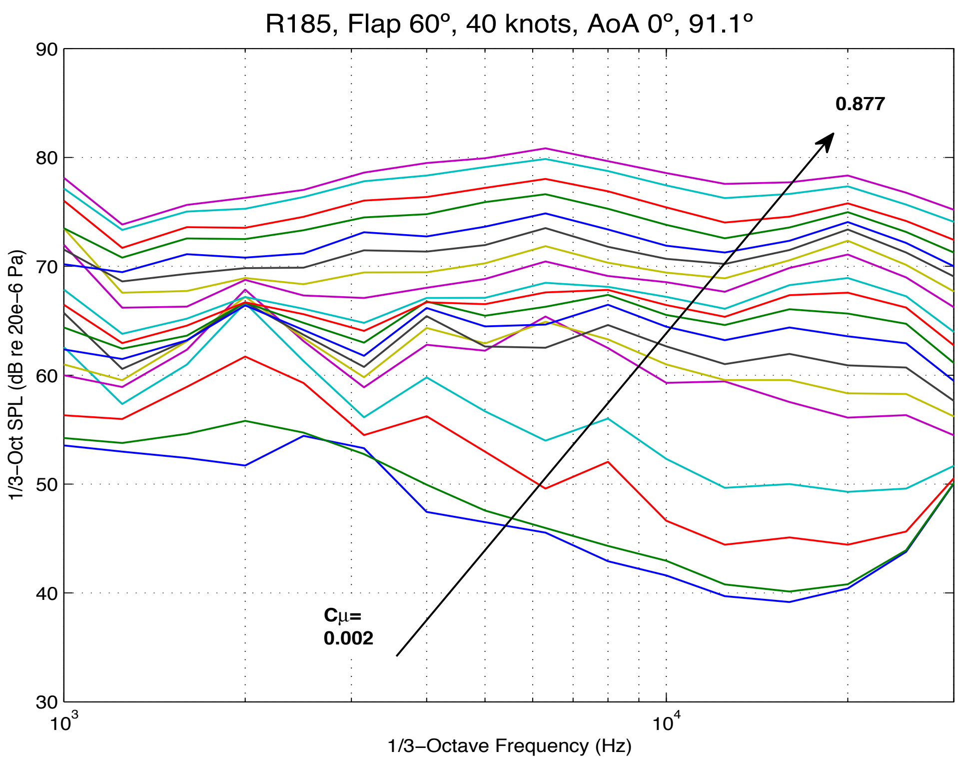

Figure 91. Trailing- and leading-edge Cμ sweep for α = 0°, 60° flap at 40 knots.

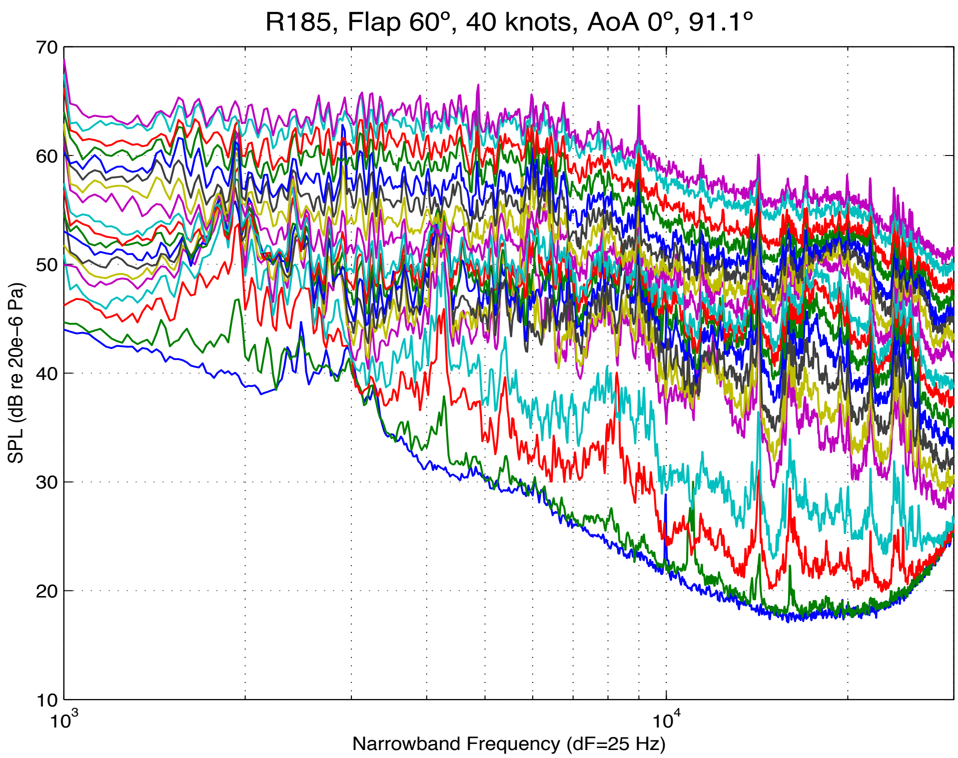

Figure 92. Narrowband plot of trailing- and leading-edge Cμ sweep for α = 0º, 60º flap at 40 knots.

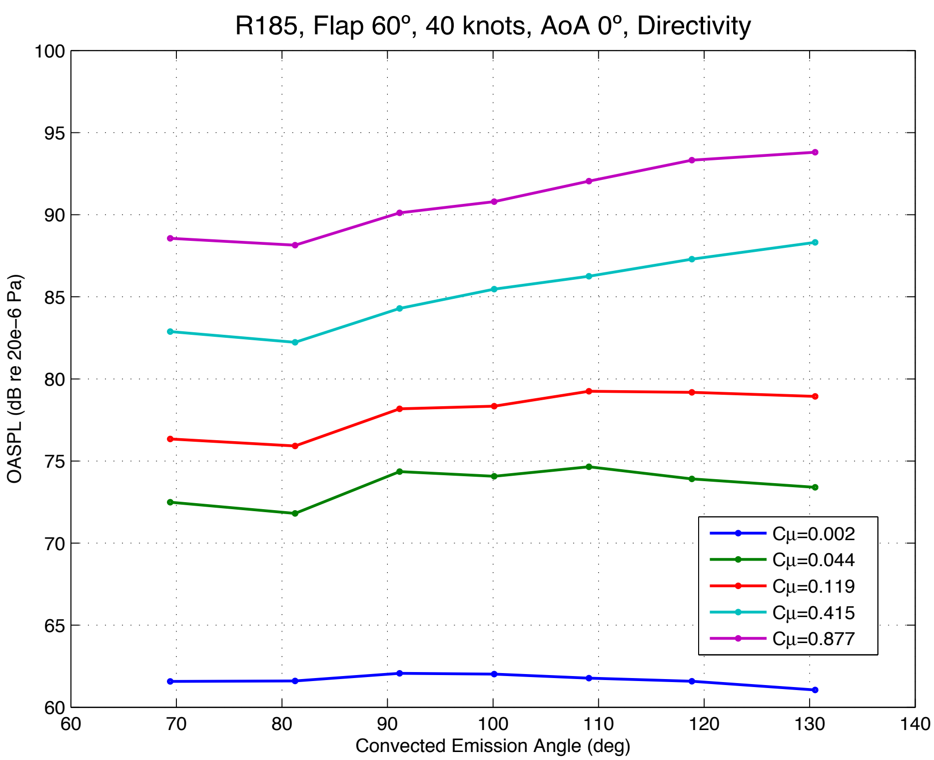

Figure 93. Directivity of trailing- and leading-edge Cμ sweep for α = 0º, 60º flap at 40 knots.

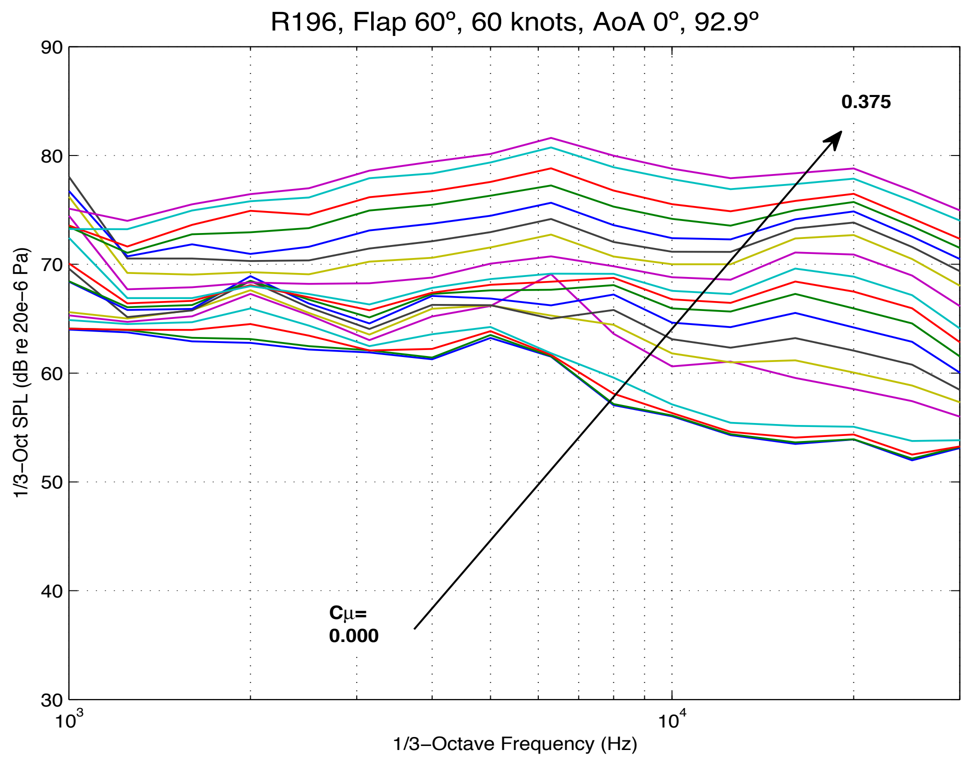

Figure 94. Trailing- and leading-edge Cμ sweep for α = 0º, 60º flap at 60 knots.

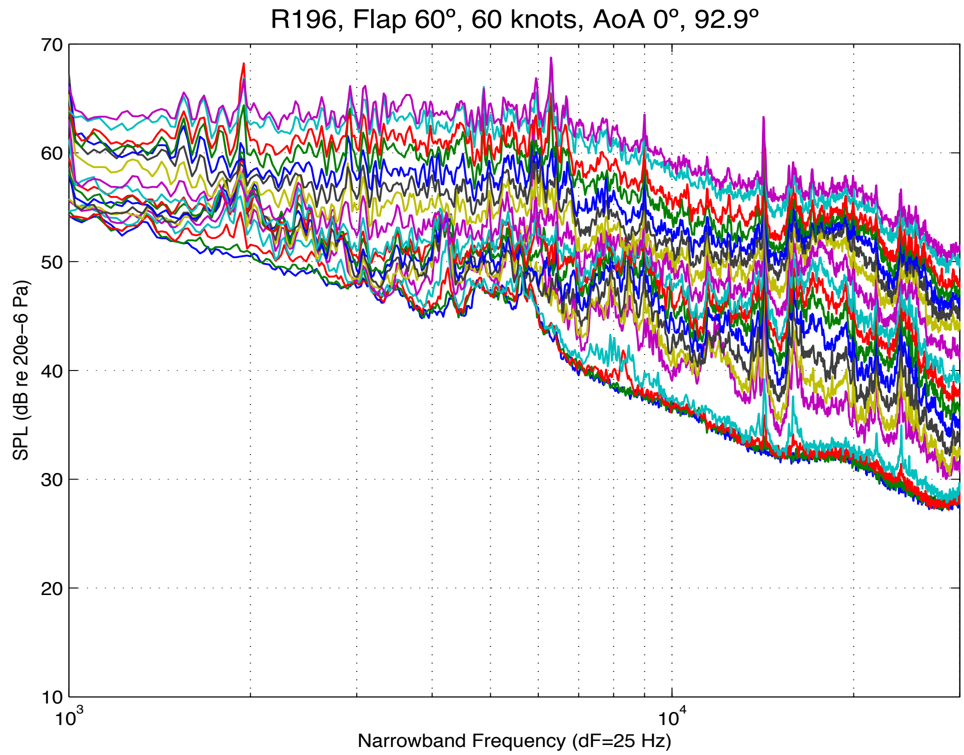

Figure 95. Narrowband plot of trailing- and leading-edge Cμ sweep for α = 0º, 60º flap at 60 knots.

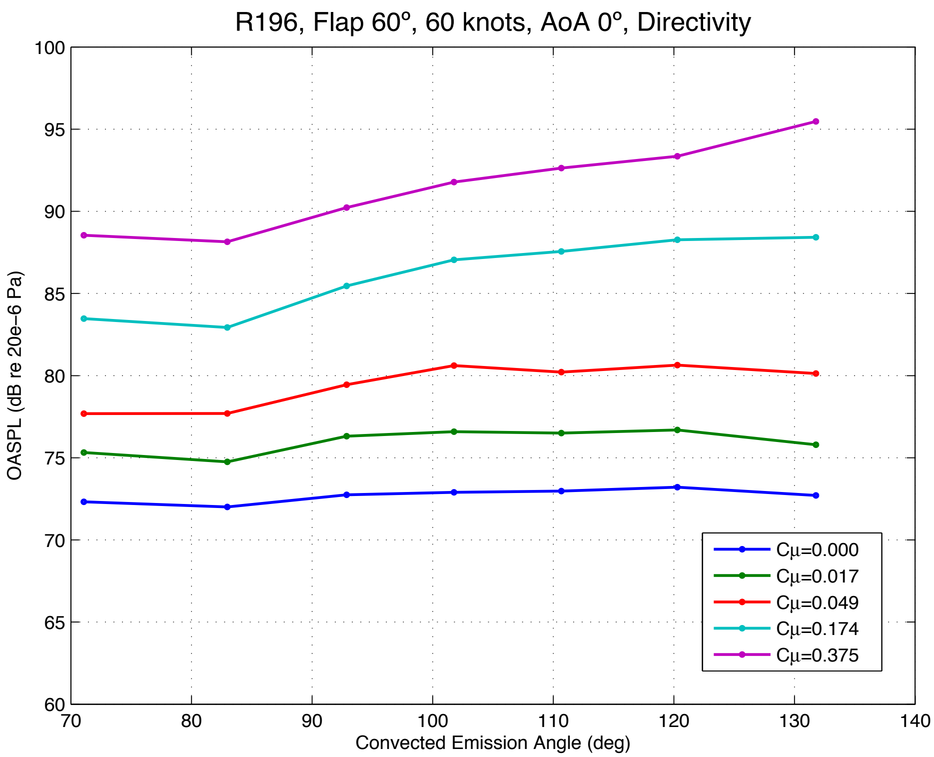

Figure 96. Directivity of trailing- and leading-edge Cμ sweep for α = 0°, 60° flap at 60 knots.

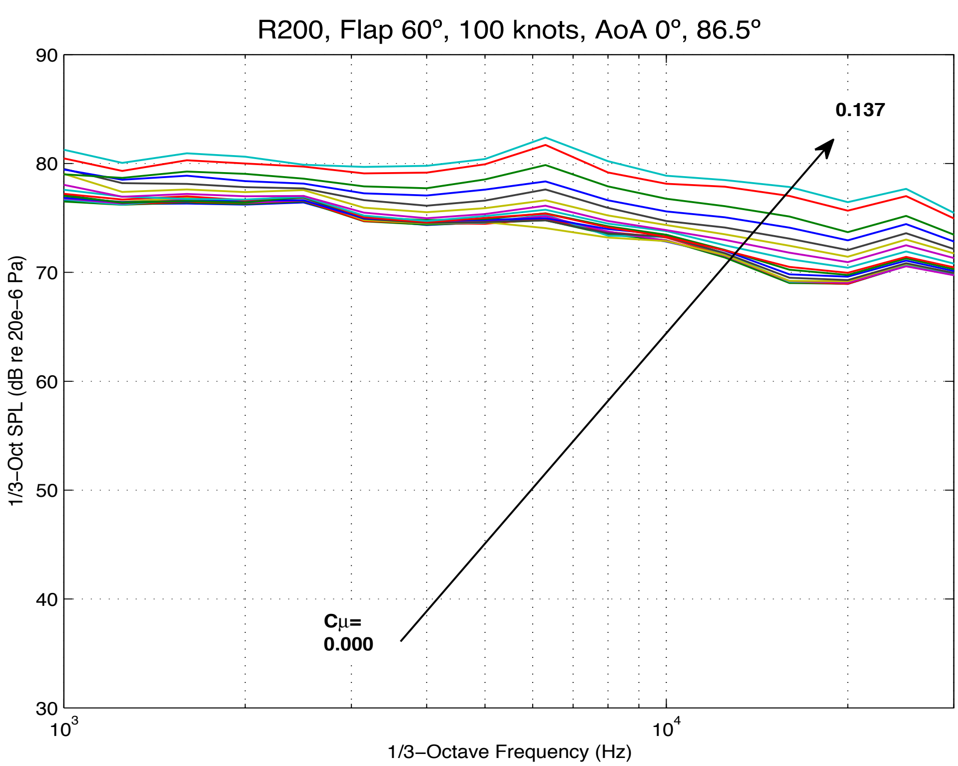

Figure 97. Trailing- and leading-edge Cμ sweep for α = 0°, 60° flap at 100 knots.

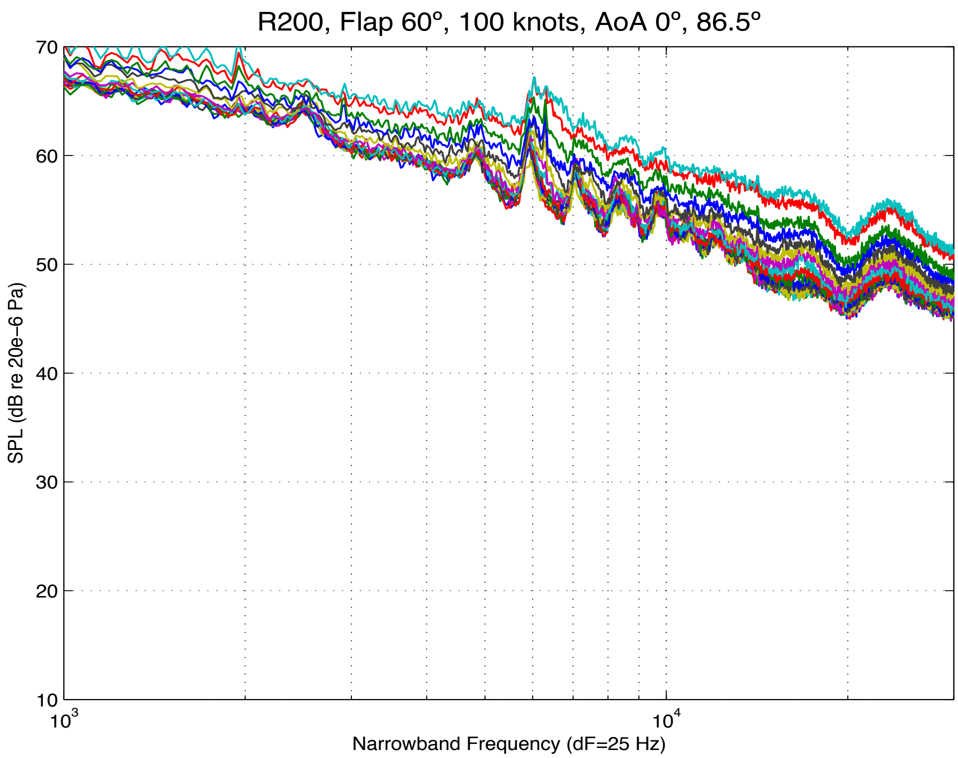

Figure 98. Narrowband plot of trailing- and leading-edge Cμ sweep for α = 0°, 60° flap at 100 knots.

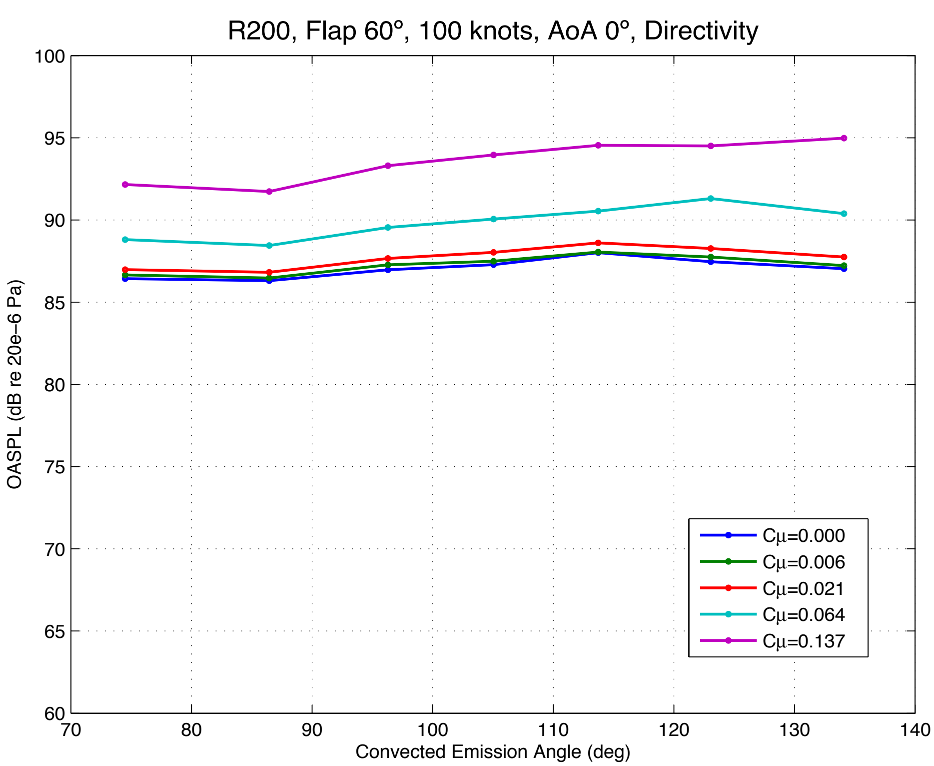

Figure 99. Directivity of trailing- and leading-edge Cμ sweep for α = 0°, 60° flap at 100 knots.

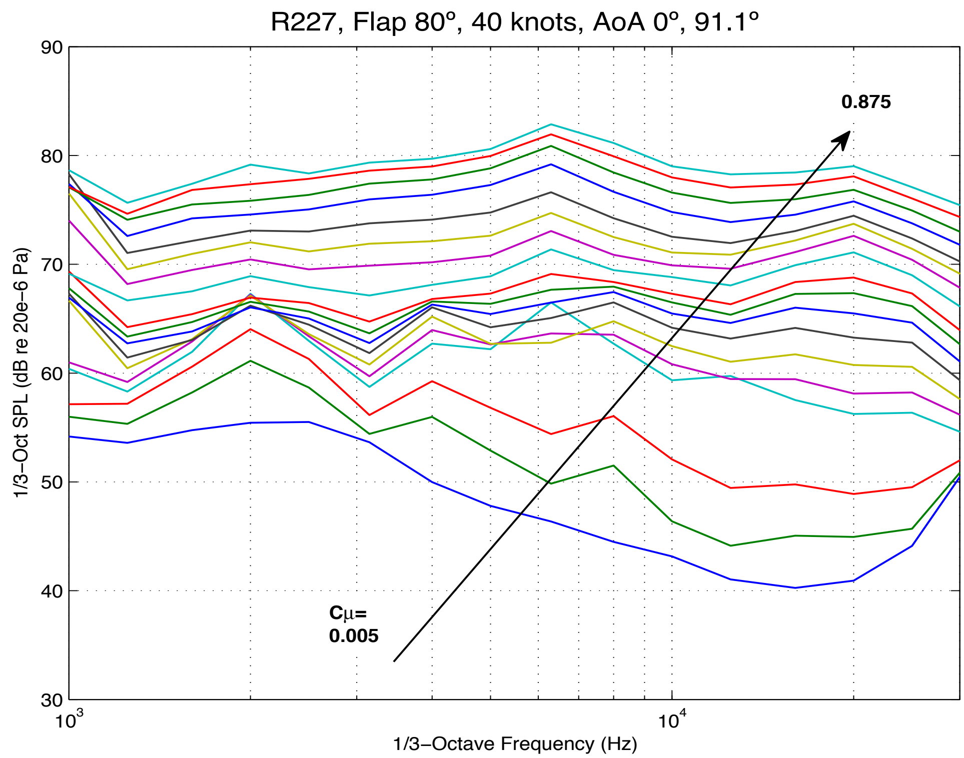

Figure 100. Trailing- and leading-edge Cμ sweep for α = 0º, 80º flap at 40 knots.

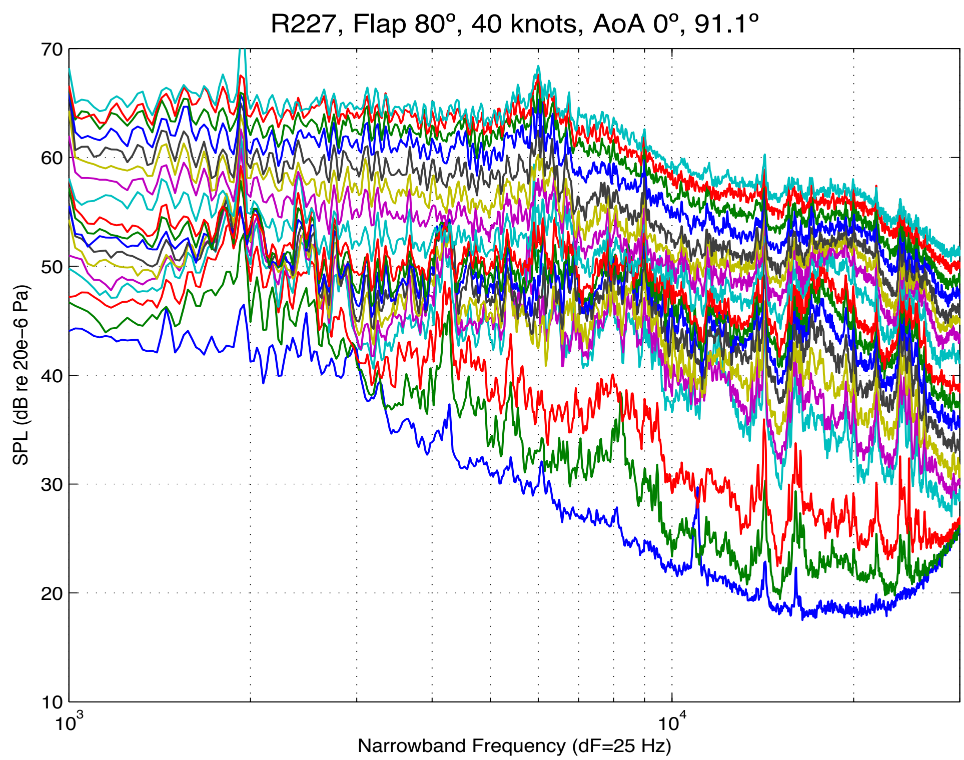

Figure 101. Narrowband plot of trailing- and leading-edge Cμ sweep for α = 0º, 80º flap at 40 knots.

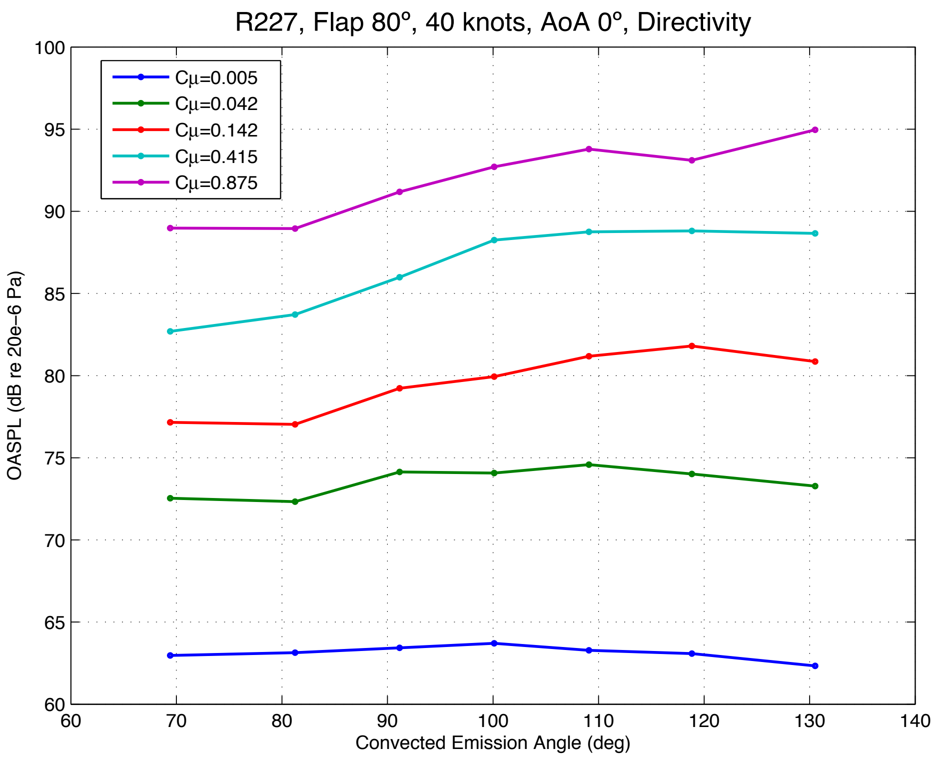

Figure 102. Directivity of trailing- and leading-edge Cμ sweep for α = 0º, 80º flap at 40 knots.

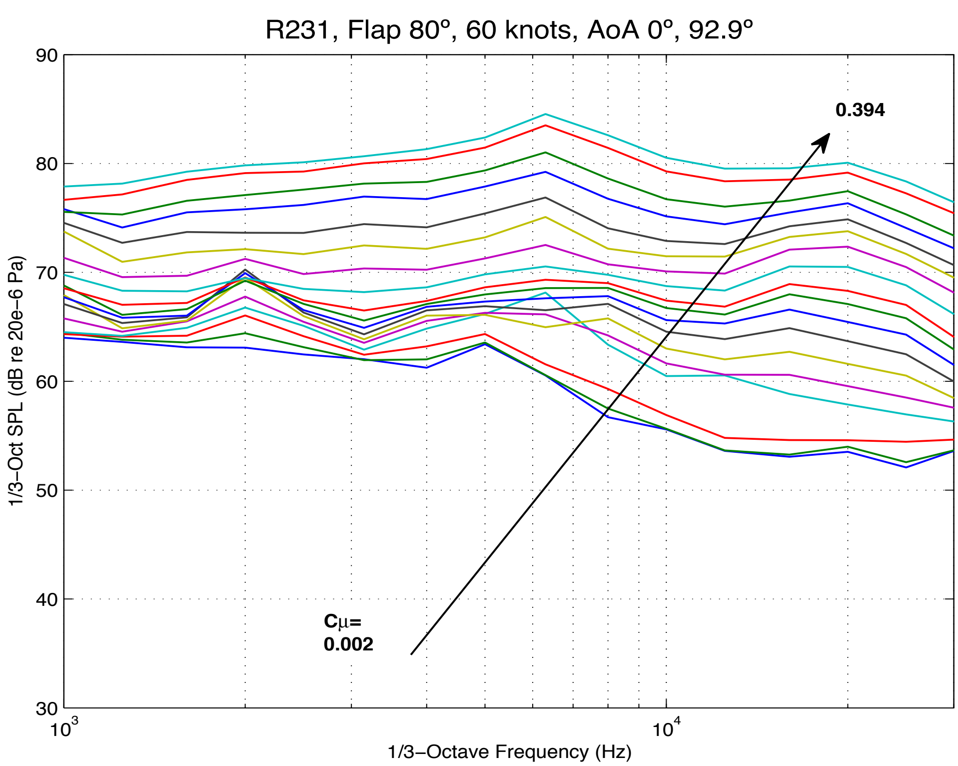

Figure 103. Trailing- and leading-edge Cμ sweep for α = 0º, 80º flap at 60 knots.

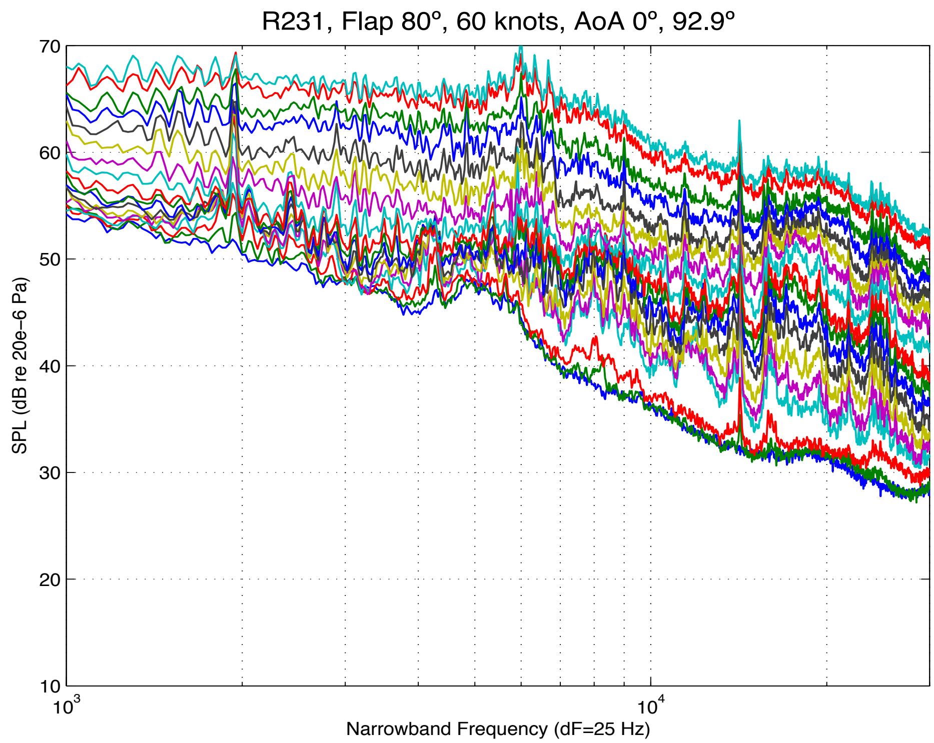

Figure 104. Narrowband plot of trailing- and leading-edge Cμ sweep for α = 0º, 80º flap at 60 knots.

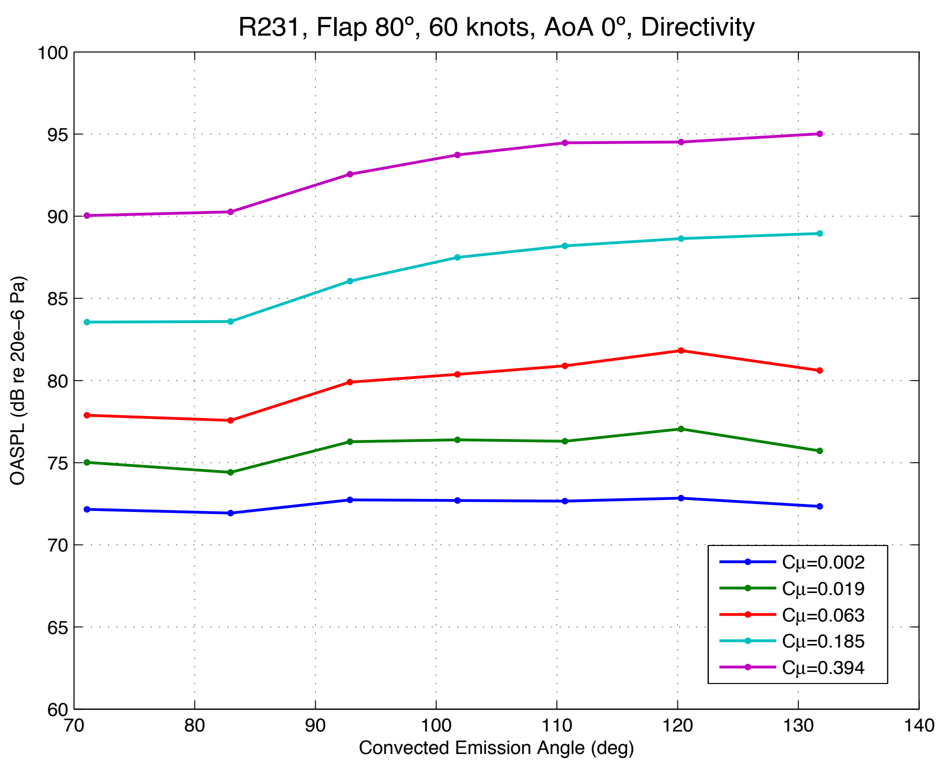

Figure 105. Directivity of trailing- and leading-edge Cμ sweep for α = 0º, 80º flap at 60 knots.

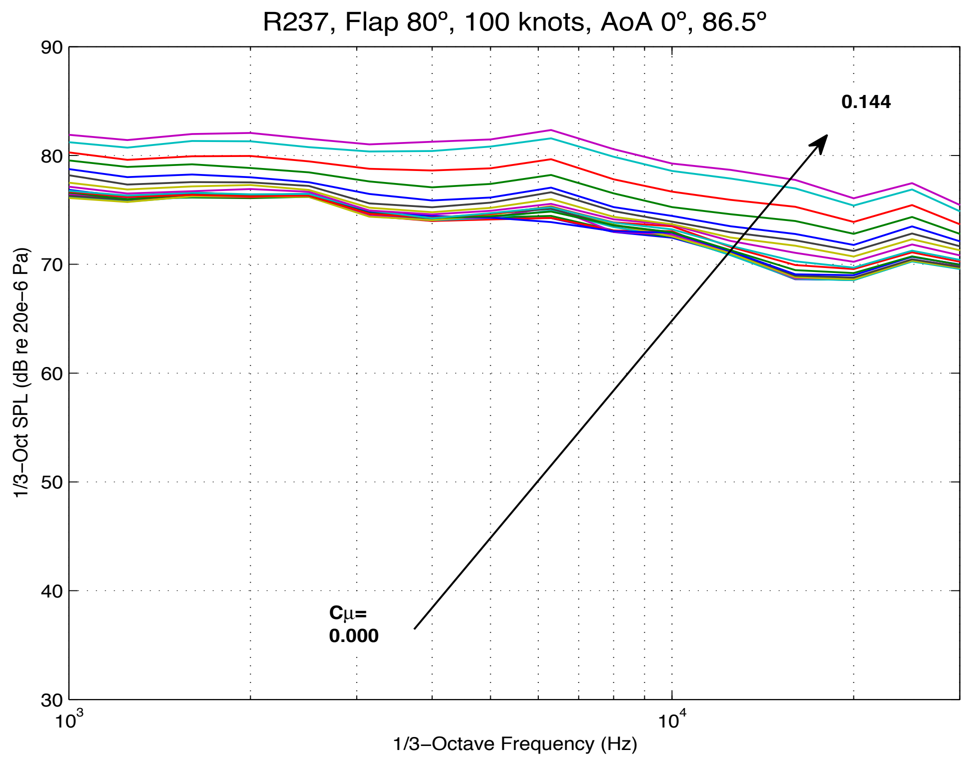

Figure 106. Trailing- and leading-edge Cμ sweep for α = 0º, 80º flap at 100 knots.

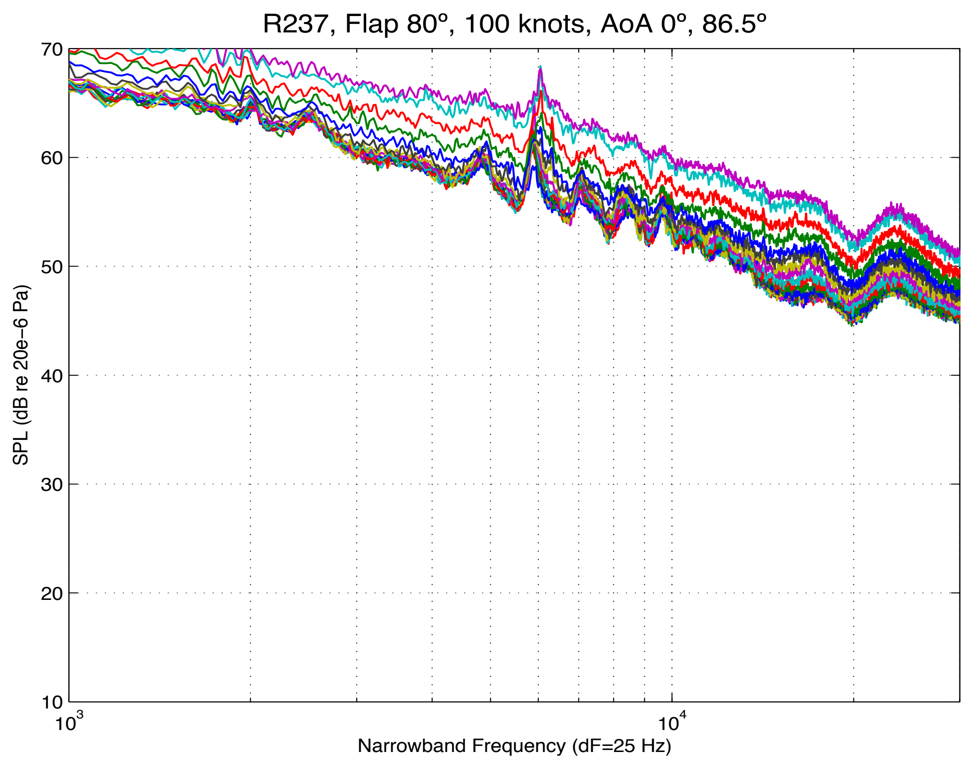

Figure 107. Narrowband plot of trailing- and leading-edge Cμ sweep for α = 0º, 80º flap at 100 knots.

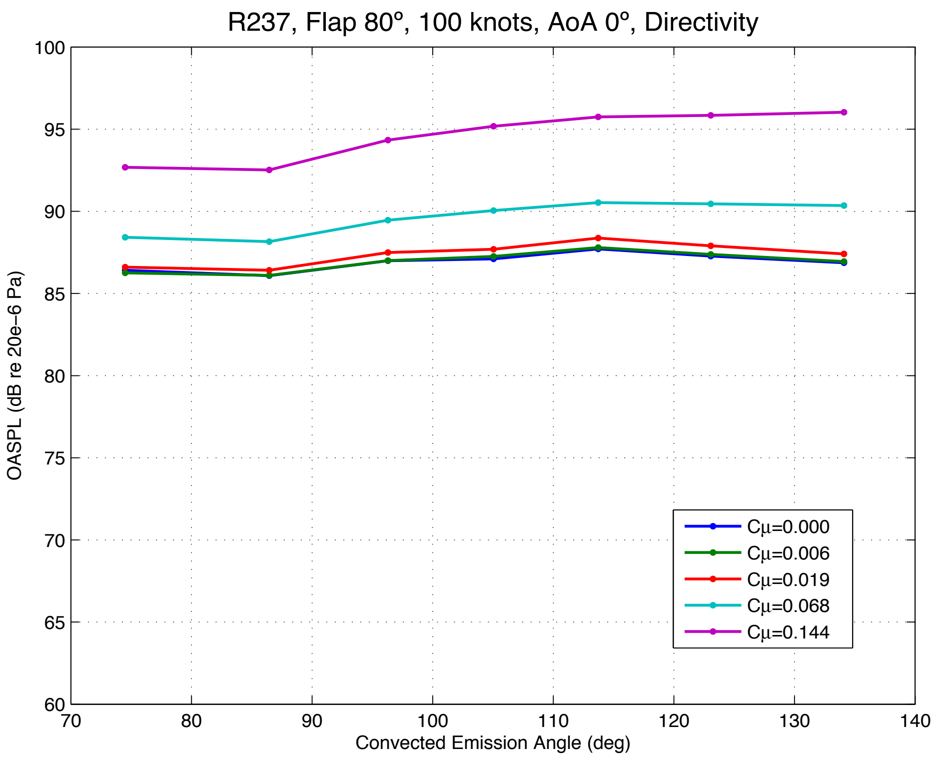

Figure 108. Directivity of trailing- and leading-edge Cμ sweep for α = 0º, 80º flap at 100 knots.

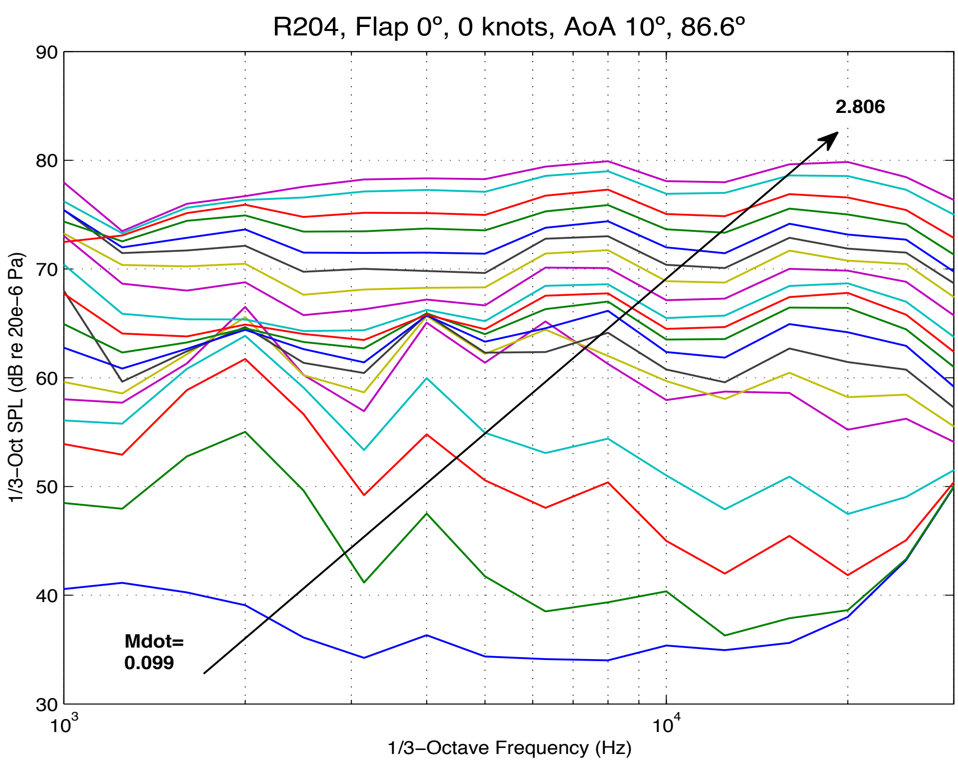

Figure 109. Trailing- and leading-edge Cμ sweep for α = 10º, 0º flap at 0 knots.

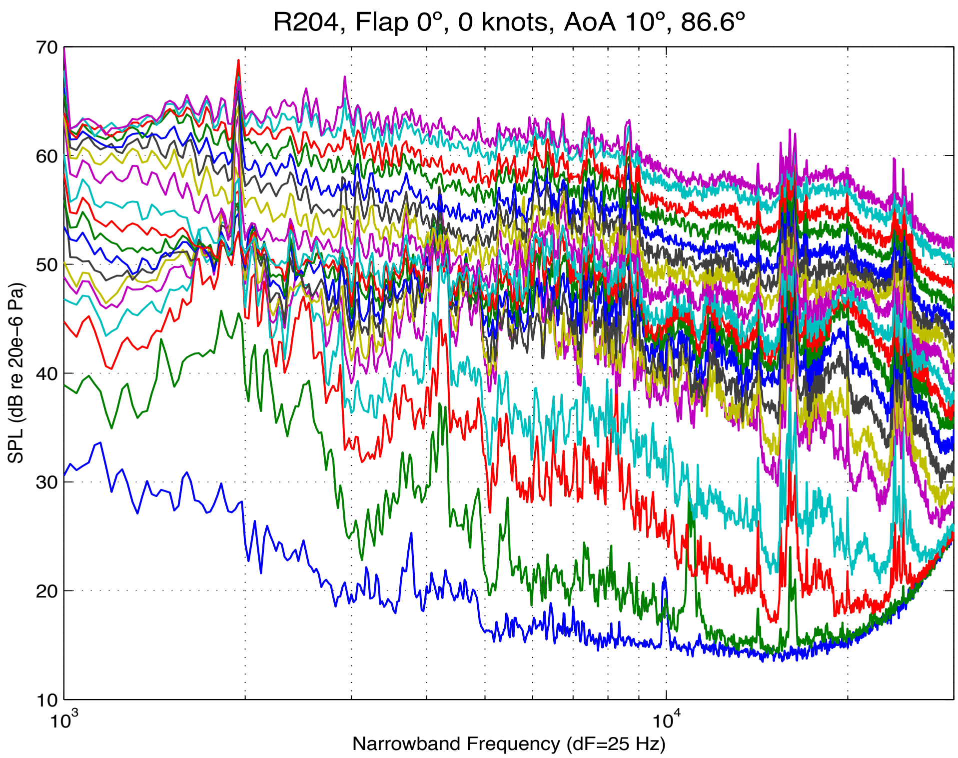

Figure 110. Narrowband plot of trailing- and leading-edge Cμ sweep for α = 10º, 0º flap at 0 knots.

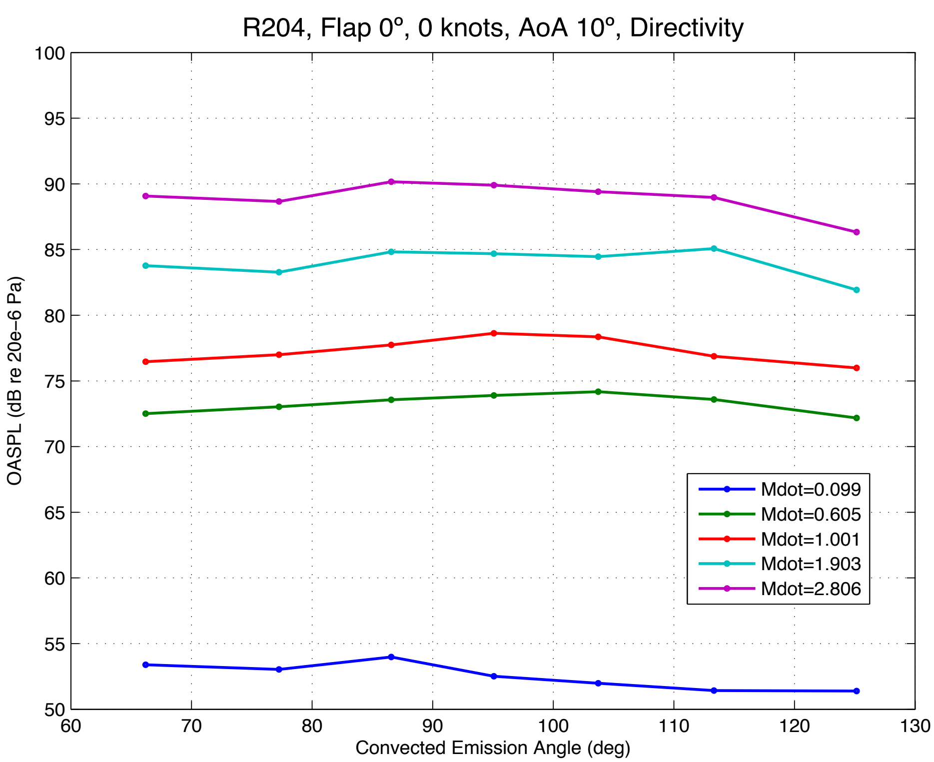

Figure 111. Directivity of trailing- and leading-edge Cμ sweep for α = 10º, 0º flap at 0 knots.

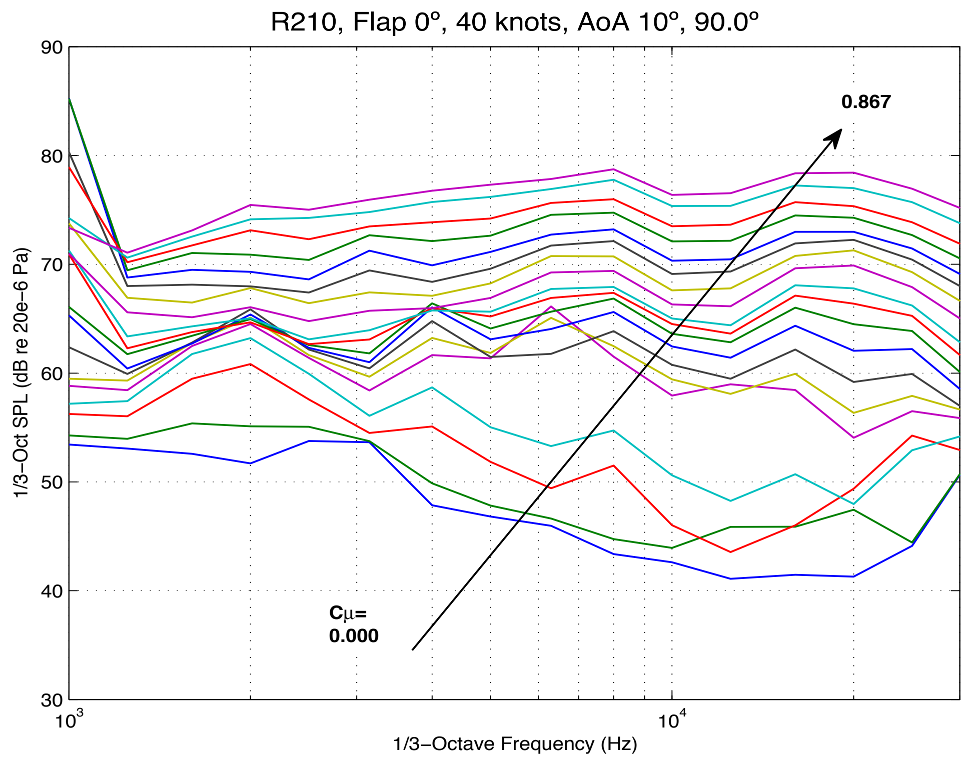

Figure 112. Trailing- and leading-edge Cμ sweep for α = 10º, 0º flap at 40 knots.

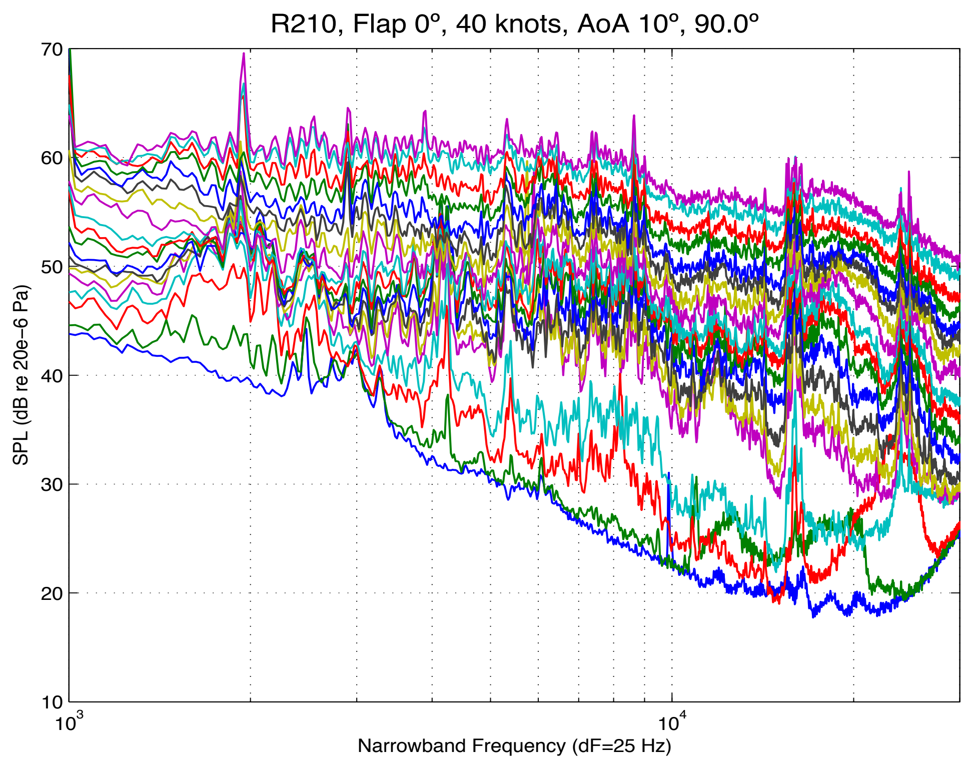

Figure 113. Narrowband plot of trailing- and leading-edge Cμ sweep for α = 10º, 0º flap at 40 knots.

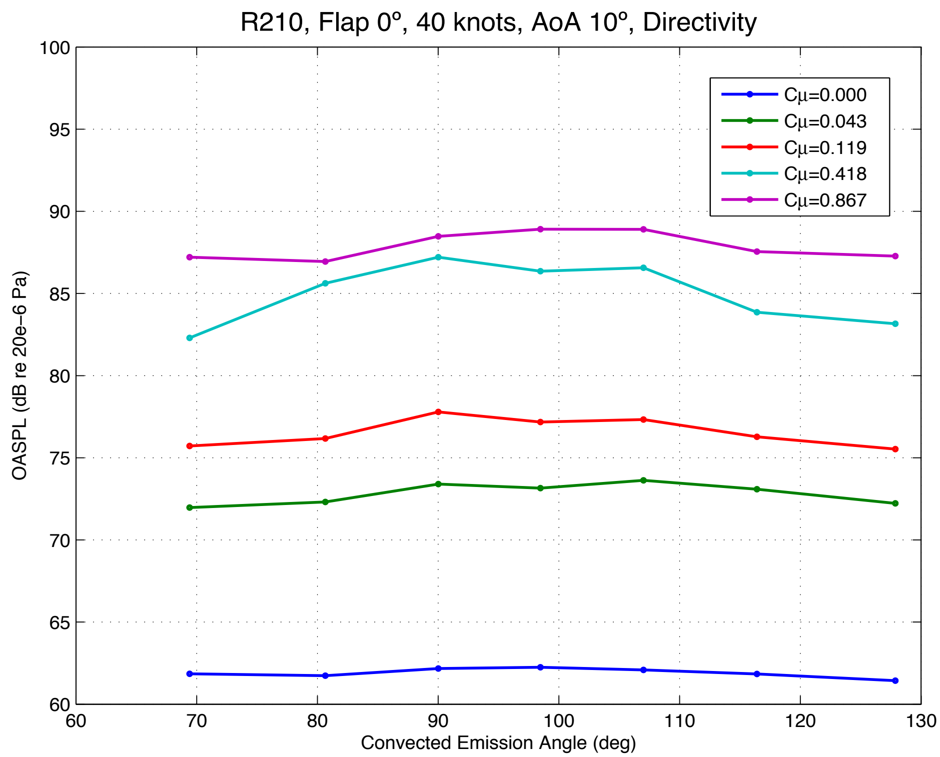

Figure 114. Directivity of trailing- and leading-edge Cμ sweep for α = 10º, 0º flap at 40 knots.

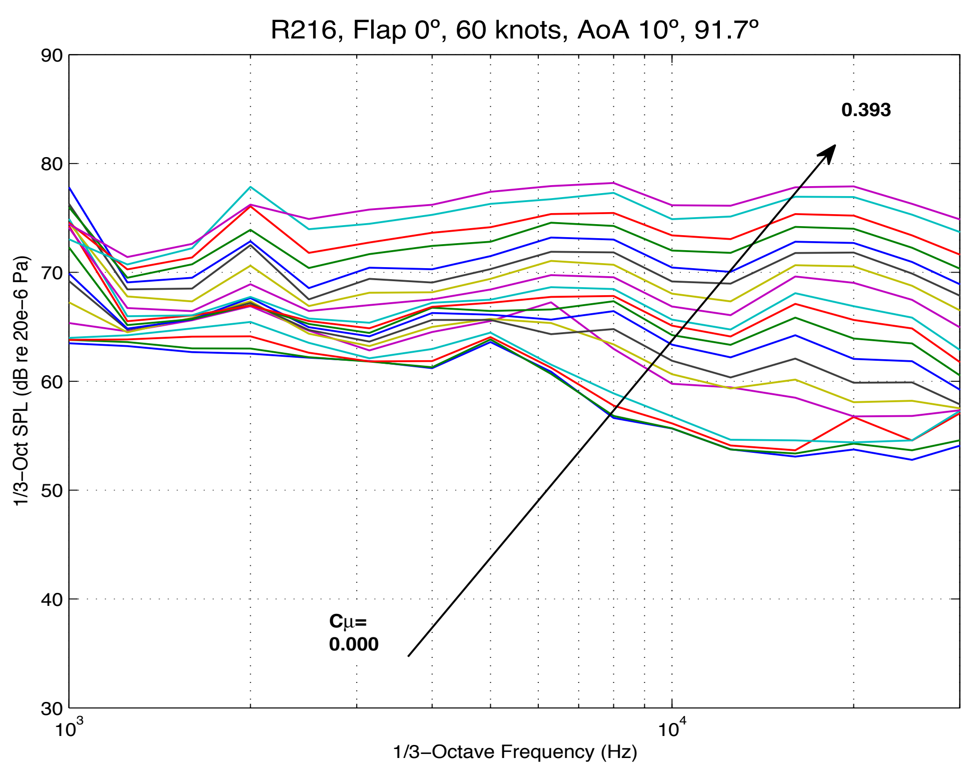

Figure 115. Trailing- and leading-edge Cμ sweep for α = 10º, 0º flap at 60 knots.

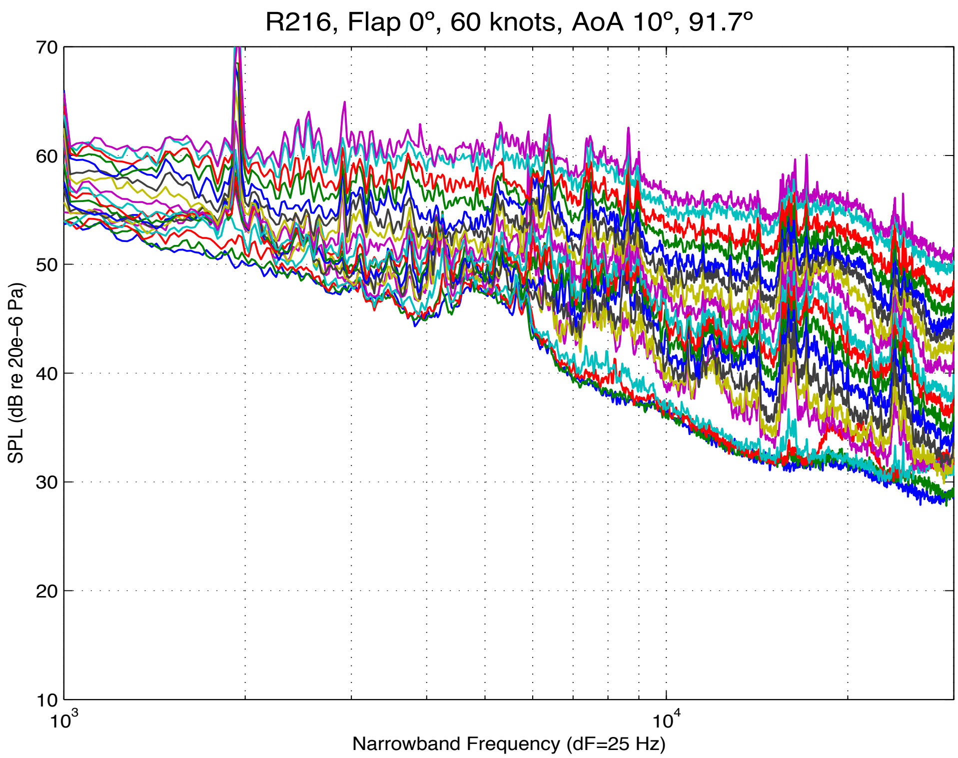

Figure 116. Narrowband plot of trailing- and leading-edge Cμ sweep for α = 10º, 0º flap at 60 knots.

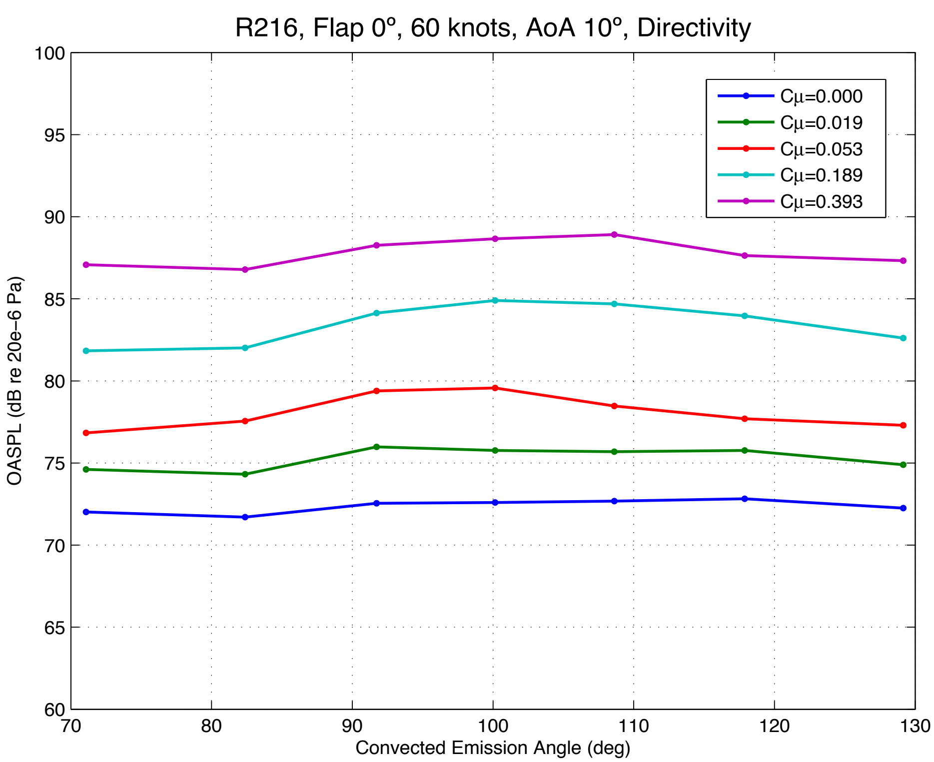

Figure 117. Directivity of trailing- and leading-edge Cμ sweep for α = 10º, 0º flap at 60 knots.

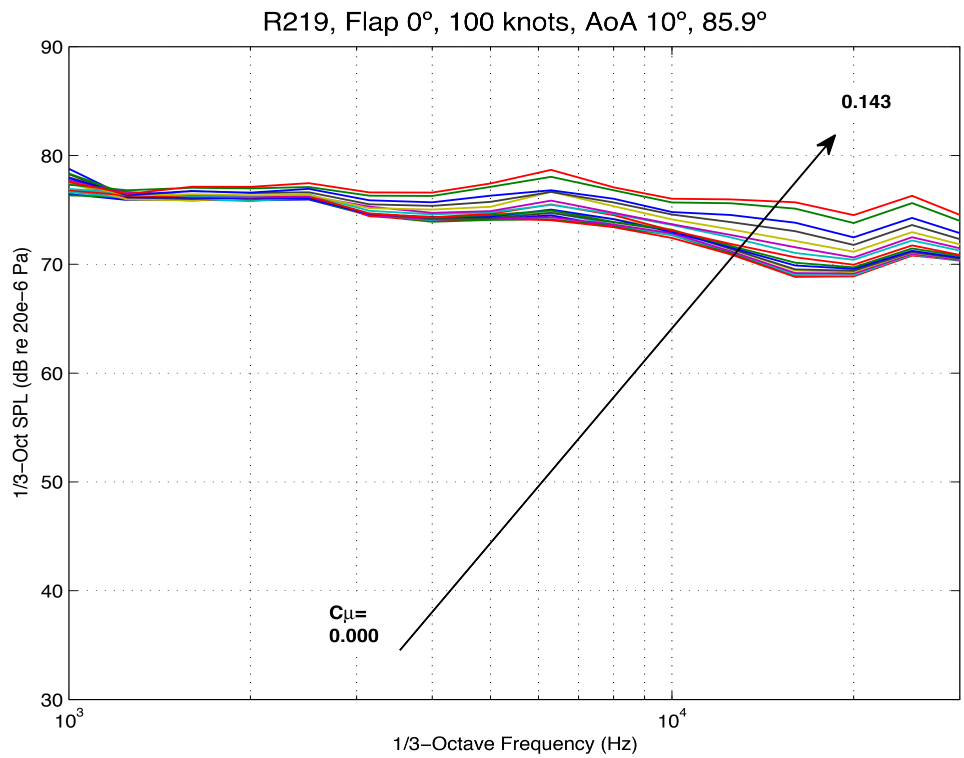

Figure 118. Trailing- and leading-edge Cμ sweep for α = 10º, 0º flap at 100 knots.

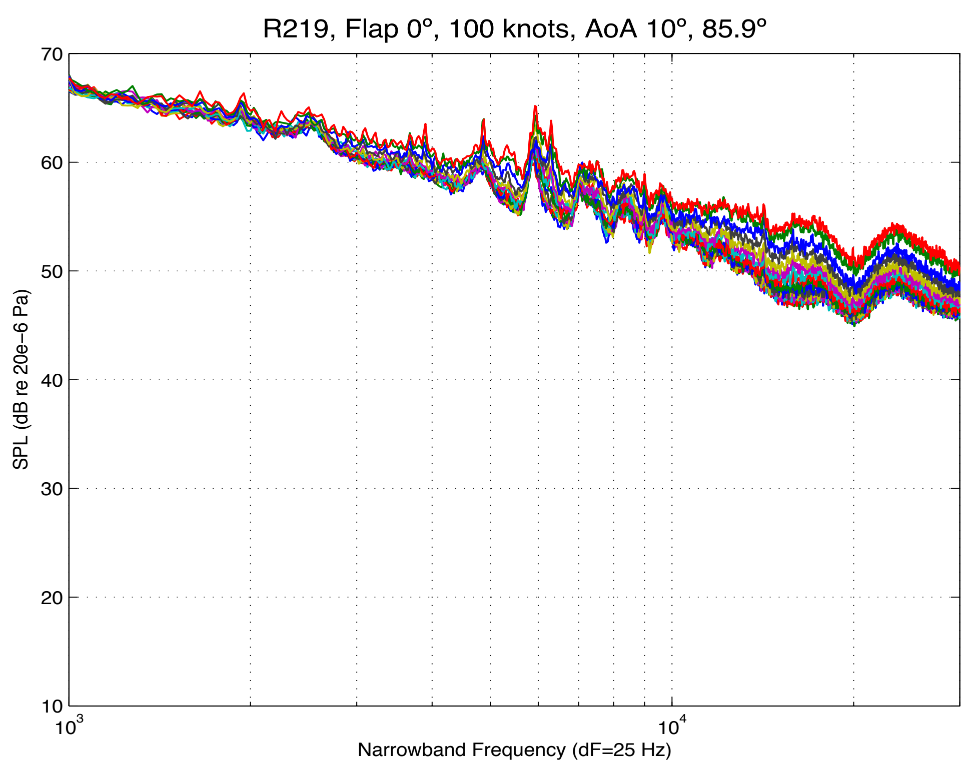

Figure 119. Narrowband plot of trailing- and leading-edge Cμ sweep for α = 10º, 0º flap at 100 knots.

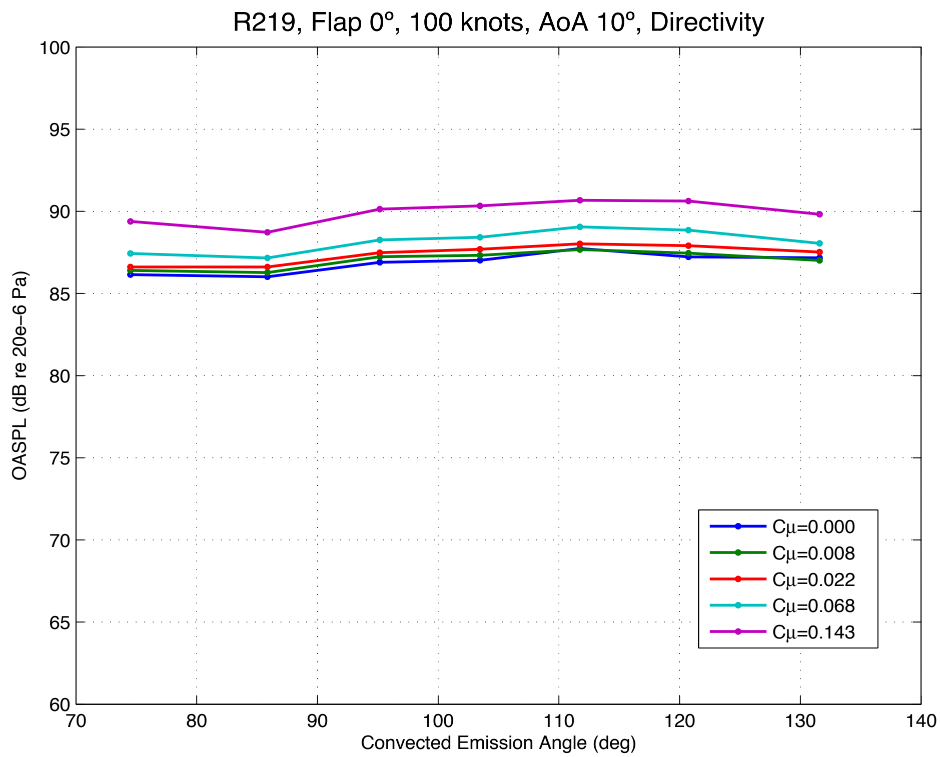

Figure 120. Directivity of trailing- and leading-edge Cμ sweep for α = 10º, 0º flap at 100 knots.

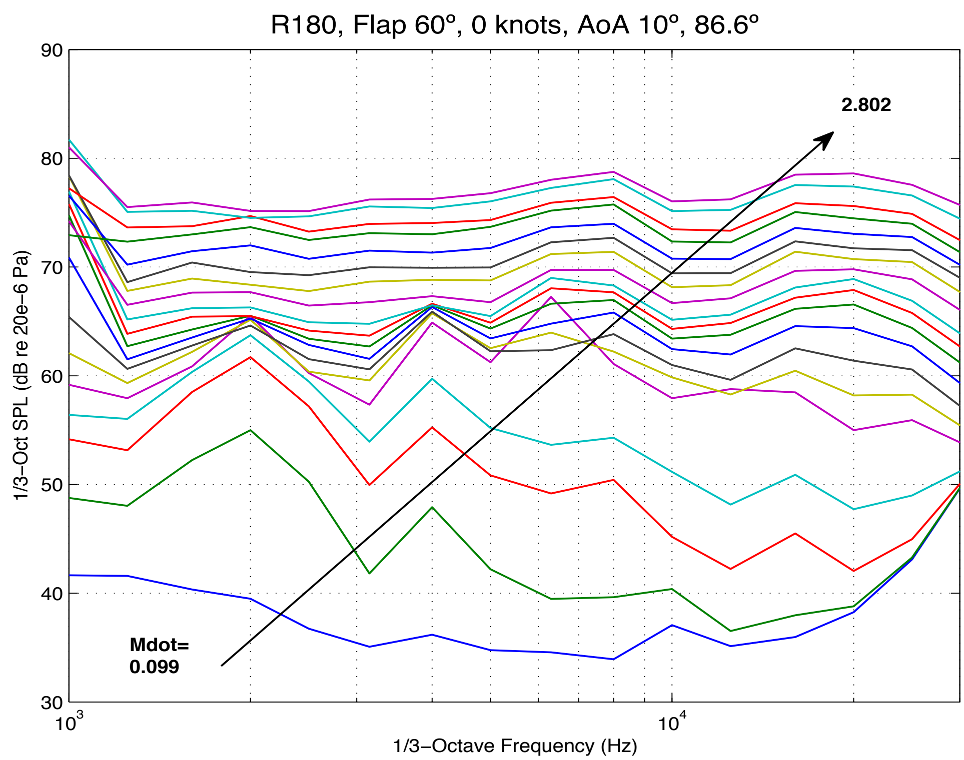

Figure 121. Trailing- and leading-edge Cμ sweep for α = 10º, 60º flap at 0 knots.

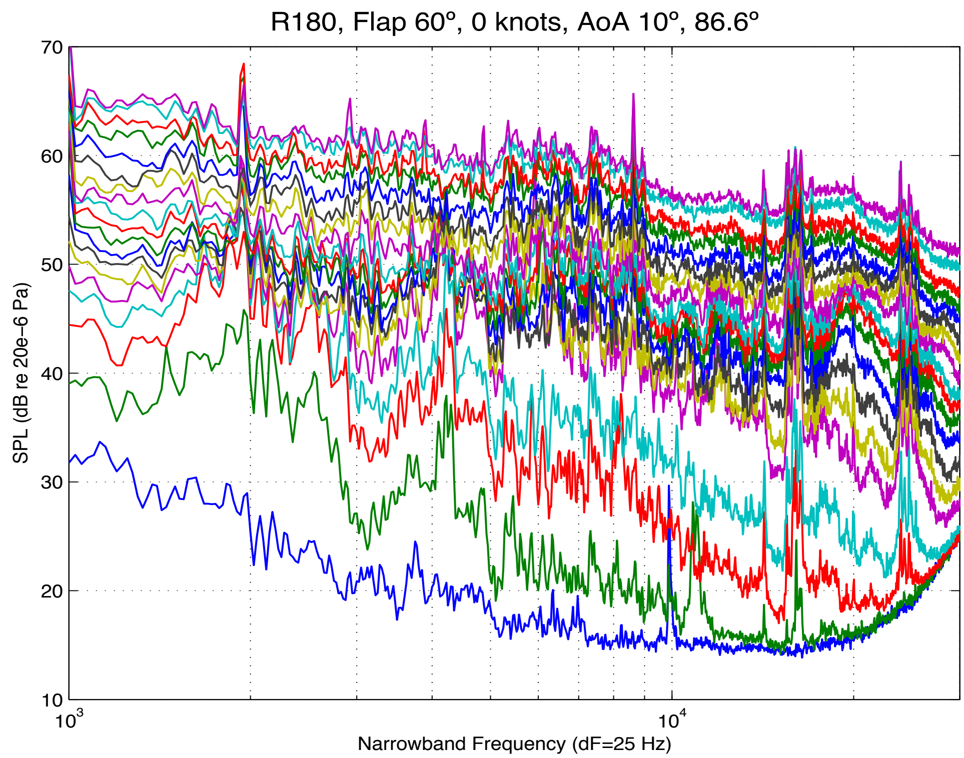

Figure 122. Narrowband plot of trailing- and leading-edge Cμ sweep for α = 10º, 60º flap at 0 knots.

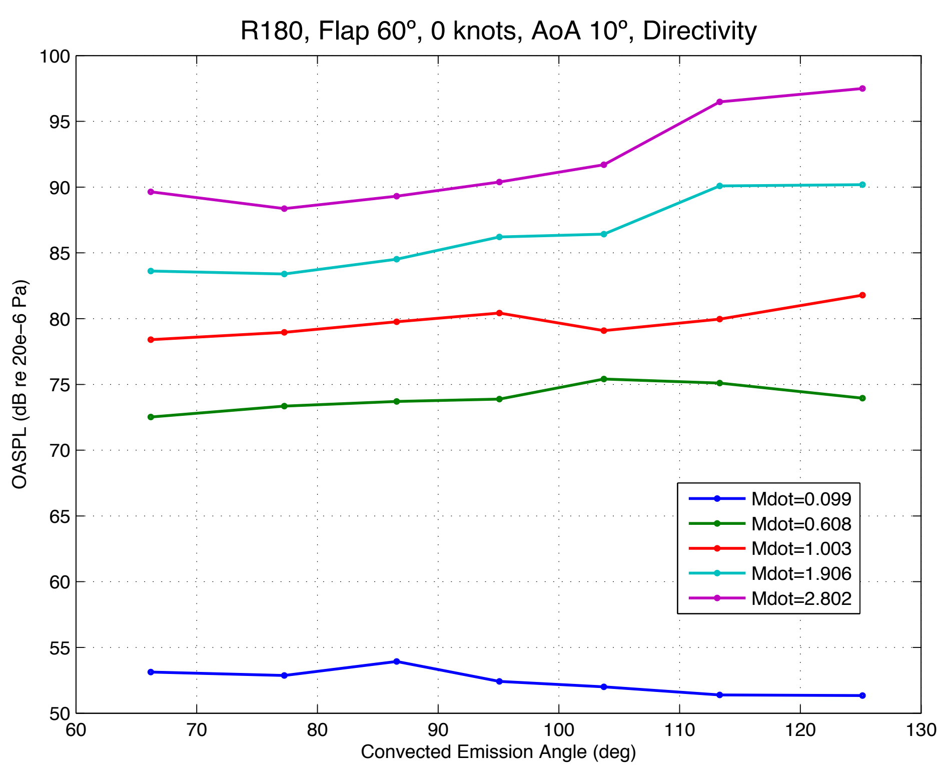

Figure 123. Directivity of trailing- and leading-edge Cμ sweep for α = 10º, 60º flap at 0 knots.

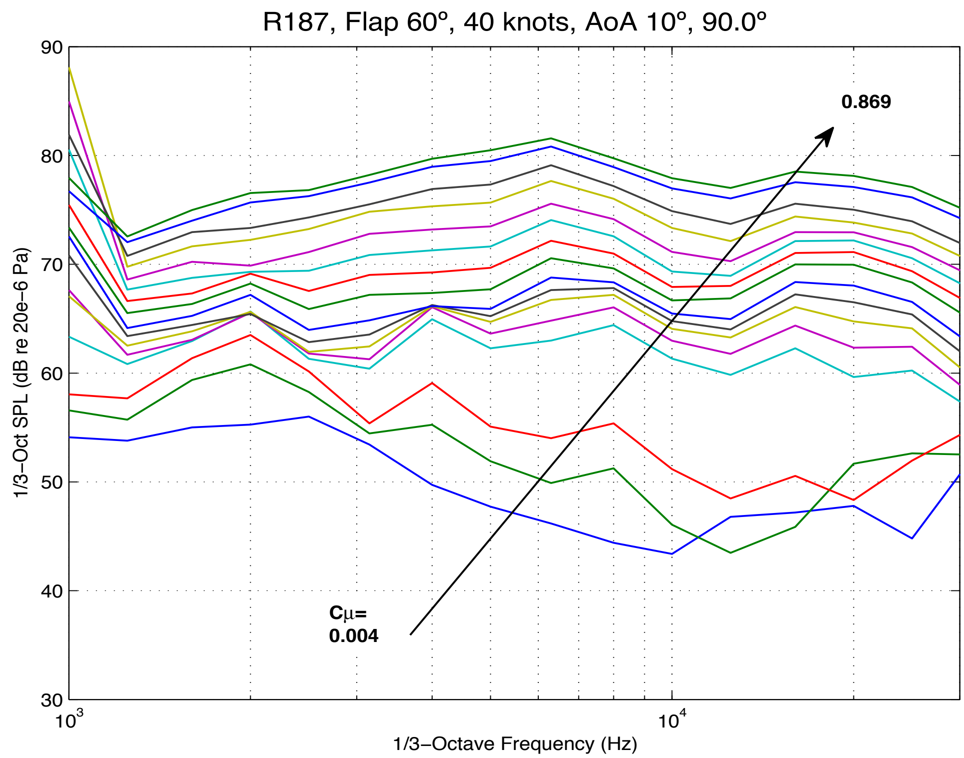

Figure 124. Trailing- and leading-edge Cμ sweep for α = 10º, 60º flap at 40 knots.

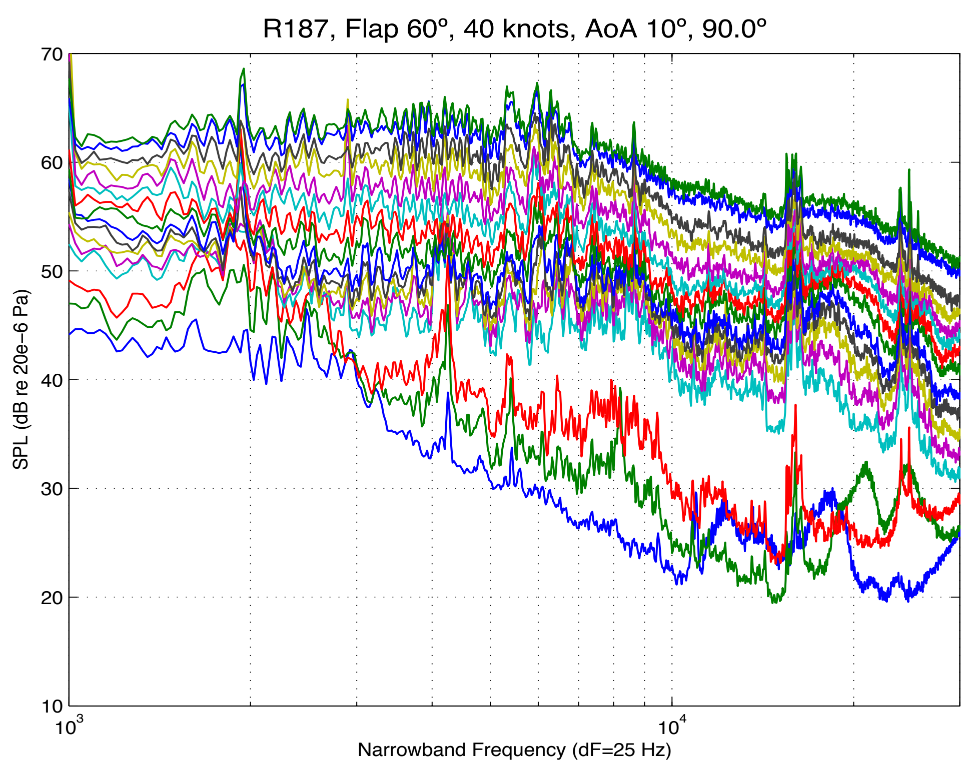

Figure 125. Narrowband plot of trailing- and leading-edge Cμ sweep for α = 10º, 60º flap at 40 knots.

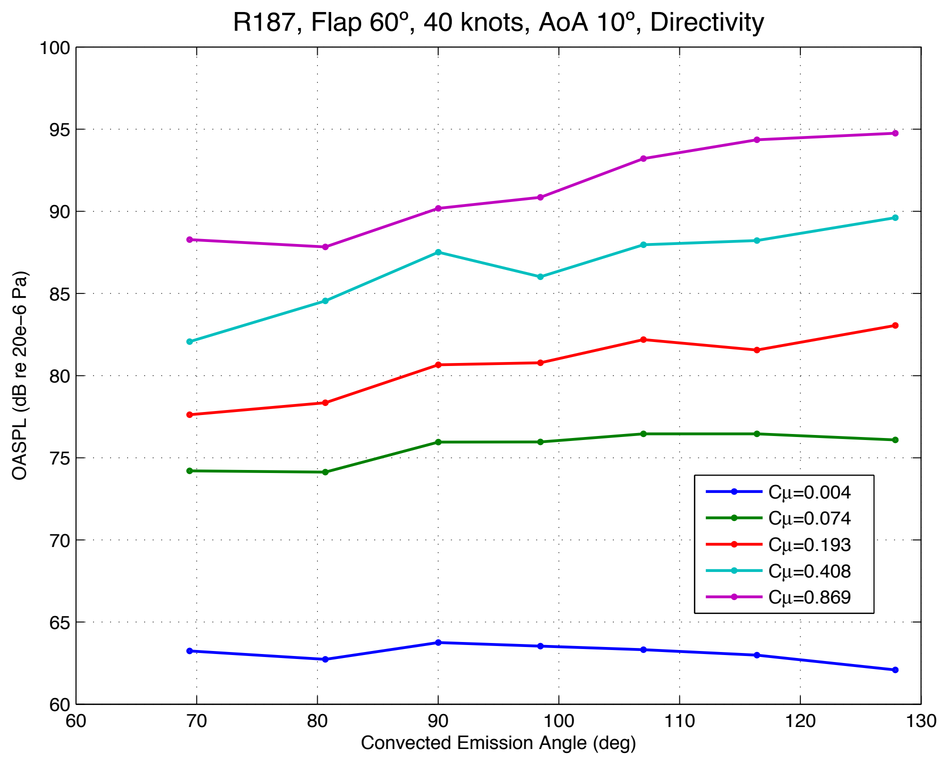

Figure 126. Directivity of trailing- and leading-edge Cμ sweep for α = 10º, 60º flap at 40 knots.

Appendix A

Table 1. Sensor locations relative to acoustic center for -10º sideslip. Rho is inches and theta and phi are in degrees.

AoA (deg)	Coordinate	Mic1	Mic2	Mic3	Mic4	Mic5	Mic6	Mic7	Array
-5	Rho	333.5	301.8	287.4	282.6	285.2	297.1	327.4	291.6
	Theta	66.0	77.7	87.7	96.8	106.0	116.2	128.4	114.3
	Phi	58.5	57.0	56.0	55.0	54.1	52.9	51.2	-50.7
-3	Rho	336.2	304.7	290.4	285.5	288.0	299.8	329.8	294.6
	Theta	66.1	77.7	87.6	96.6	105.8	115.8	128.0	113.9
	Phi	57.6	56.1	55.1	54.1	53.2	52.0	50.3	-49.8
-1	Rho	339.1	307.7	293.4	288.5	290.9	302.4	332.0	297.6
	Theta	66.2	77.7	87.5	96.4	105.5	115.4	127.5	113.5
	Phi	56.8	55.2	54.2	53.3	52.3	51.1	49.4	-49.0
0	Rho	340.5	309.2	294.9	290.0	292.3	303.7	333.1	299.1
	Theta	66.2	77.7	87.4	96.3	105.3	115.2	127.3	113.3
	Phi	56.3	54.8	53.8	52.8	51.8	50.7	48.9	-48.6
1	Rho	342.0	310.8	296.5	291.5	293.7	305.0	334.1	300.6
	Theta	66.2	77.7	87.3	96.2	105.1	115.0	127.1	113.1
	Phi	55.9	54.4	53.3	52.4	51.4	50.2	48.5	-48.2
3	Rho	345.0	313.9	299.6	294.5	296.5	307.5	336.2	303.6
	Theta	66.3	77.6	87.2	95.9	104.8	114.6	126.6	112.6
	Phi	55.1	53.6	52.5	51.6	50.6	49.4	47.6	-47.4
5	Rho	348.2	317.1	302.7	297.5	299.3	310.0	338.3	306.6
	Theta	66.3	77.5	87.0	95.6	104.4	114.1	126.0	112.1
	Phi	54.3	52.7	51.7	50.7	49.7	48.5	46.7	-46.6
7	Rho	351.4	320.3	305.8	300.5	302.1	312.4	340.2	309.6
	Theta	66.2	77.4	86.7	95.3	104.0	113.6	125.5	111.6
	Phi	53.5	52.0	50.9	49.9	48.9	47.7	45.9	-45.9
10	Rho	356.3	325.2	310.6	304.9	306.1	316.0	343.0	314.0
	Theta	66.2	77.1	86.3	94.7	103.3	112.9	124.7	110.8
	Phi	52.4	50.8	49.7	48.8	47.7	46.5	44.7	-44.9
12	Rho	359.7	328.6	313.7	307.9	308.8	318.3	344.7	317.0
	Theta	66.1	76.9	86.0	94.3	102.8	112.3	124.1	110.2
	Phi	51.7	50.1	49.0	48.0	47.0	45.8	44.0	-44.3
15	Rho	364.8	333.6	318.5	312.3	312.8	321.6	347.2	321.4
	Theta	65.9	76.5	85.5	93.7	102.1	111.5	123.2	109.4
	Phi	50.6	49.0	47.9	46.9	45.9	44.7	42.9	-43.3
17	Rho	368.3	337.0	321.7	315.2	315.4	323.8	348.7	324.2
	Theta	65.7	76.3	85.1	93.2	101.6	110.9	122.6	108.8
	Phi	49.9	48.3	47.2	46.2	45.2	44.0	42.2	-42.8
20	Rho	373.7	342.1	326.4	319.6	319.2	326.9	350.9	328.5
	Theta	65.5	75.8	84.5	92.5	100.7	110.0	121.6	107.8

AoA (deg)	Coordinate	Mic1	Mic2	Mic3	Mic4	Mic5	Mic6	Mic7	Array
	Phi	48.9	47.3	46.2	45.2	44.2	42.9	41.1	-42.0
22	Rho	377.3	345.5	329.6	322.4	321.7	329.0	352.2	331.3
	Theta	65.3	75.5	84.1	92.0	100.2	109.3	121.0	107.2
	Phi	48.3	46.7	45.5	44.6	43.5	42.3	40.5	-41.5
25	Rho	382.7	350.6	334.3	326.6	325.3	331.9	354.1	335.5
	Theta	64.9	75.0	83.5	91.2	99.3	108.4	120.0	106.2
	Phi	47.3	45.7	44.6	43.6	42.6	41.4	39.6	-40.8

Table 2. Sensor locations relative to acoustic center for -5º sideslip. Rho is inches and theta and phi are in degrees.

AoA (deg)	Coordinate	Mic1	Mic2	Mic3	Mic4	Mic5	Mic6	Mic7	Array
-5	Rho	331.0	299.4	285.2	280.6	283.4	295.7	326.5	293.9
	Theta	66.0	77.8	87.8	97.0	106.4	116.5	128.8	114.3
	Phi	58.2	56.7	55.7	54.7	53.8	52.6	50.8	-51.1
-3	Rho	333.8	302.4	288.2	283.6	286.3	298.4	328.8	296.8
	Theta	66.1	77.8	87.8	96.9	106.1	116.2	128.3	113.9
	Phi	57.4	55.8	54.8	53.8	52.9	51.7	49.9	-50.2
-1	Rho	336.8	305.5	291.3	286.6	289.2	301.1	331.1	299.7
	Theta	66.2	77.8	87.7	96.6	105.8	115.8	127.9	113.5
	Phi	56.5	55.0	53.9	53.0	52.0	50.8	49.0	-49.3
0	Rho	338.3	307.1	292.9	288.2	290.7	302.4	332.2	301.2
	Theta	66.2	77.8	87.6	96.5	105.6	115.5	127.6	113.3
	Phi	56.1	54.5	53.5	52.5	51.5	50.3	48.6	-48.9
1	Rho	339.8	308.7	294.5	289.7	292.1	303.7	333.3	302.7
	Theta	66.3	77.8	87.5	96.4	105.4	115.3	127.4	113.1
	Phi	55.7	54.1	53.1	52.1	51.1	49.9	48.1	-48.5
3	Rho	342.9	311.9	297.7	292.8	295.0	306.3	335.4	305.6
	Theta	66.3	77.7	87.3	96.1	105.0	114.9	126.9	112.6
	Phi	54.9	53.3	52.2	51.3	50.3	49.0	47.3	-47.7
5	Rho	346.1	315.2	300.9	295.9	297.9	308.9	337.5	308.5
	Theta	66.3	77.6	87.1	95.8	104.6	114.4	126.3	112.2
	Phi	54.1	52.5	51.4	50.5	49.4	48.2	46.4	-46.9
7	Rho	349.5	318.5	304.2	299.0	300.8	311.4	339.5	311.3
	Theta	66.3	77.5	86.9	95.5	104.2	113.9	125.8	111.7
	Phi	53.3	51.7	50.6	49.7	48.6	47.4	45.6	-46.2
10	Rho	354.6	323.6	309.1	303.6	305.0	315.1	342.4	315.6
	Theta	66.2	77.2	86.5	94.9	103.5	113.1	124.9	110.9
	Phi	52.2	50.6	49.5	48.5	47.5	46.3	44.5	-45.2
12	Rho	358.1	327.1	312.4	306.7	307.8	317.5	344.2	318.4
	Theta	66.1	77.0	86.1	94.5	103.0	112.5	124.3	110.3
	Phi	51.5	49.9	48.8	47.8	46.8	45.5	43.7	-44.5

AoA (deg)	Coordinate	Mic1	Mic2	Mic3	Mic4	Mic5	Mic6	Mic7	Array
15	Rho	363.5	332.4	317.4	311.3	312.0	321.0	346.8	322.6
	Theta	65.9	76.6	85.6	93.9	102.3	111.7	123.4	109.4
	Phi	50.4	48.8	47.7	46.7	45.7	44.5	42.7	-43.5
17	Rho	367.2	335.9	320.7	314.4	314.7	323.3	348.4	325.3
	Theta	65.8	76.4	85.3	93.4	101.7	111.1	122.8	108.8
	Phi	49.8	48.2	47.0	46.1	45.0	43.8	42.0	-42.9
20	Rho	372.8	341.3	325.7	319.0	318.7	326.6	350.8	329.3
	Theta	65.5	75.9	84.7	92.7	100.9	110.1	121.8	107.9
	Phi	48.8	47.2	46.1	45.1	44.1	42.8	41.0	-42.1
22	Rho	376.5	344.8	329.0	322.0	321.4	328.8	352.2	332.0
	Theta	65.3	75.6	84.2	92.1	100.3	109.5	121.1	107.3
	Phi	48.2	46.6	45.5	44.5	43.4	42.2	40.4	-41.6
25	Rho	382.3	350.3	334.0	326.5	325.3	331.9	354.3	335.8
	Theta	65.0	75.1	83.6	91.3	99.4	108.5	120.1	106.3
	Phi	47.3	45.7	44.6	43.6	42.6	41.3	39.5	-40.8

Table 3. Sensor locations relative to acoustic center for 0º sideslip. Rho is inches and theta and phi are in degrees.

AoA (deg)	Coordinate	Mic1	Mic2	Mic3	Mic4	Mic5	Mic6	Mic7	Array
-5	Rho	328.7	297.1	283.0	278.5	281.6	294.1	325.3	296.1
	Theta	65.9	77.8	88.0	97.3	106.6	116.8	129.1	114.2
	Phi	58.0	56.4	55.4	54.4	53.4	52.2	50.5	-51.4
-3	Rho	331.5	300.2	286.1	281.6	284.5	296.9	327.7	298.9
	Theta	66.1	77.9	87.9	97.1	106.3	116.5	128.6	113.9
	Phi	57.1	55.5	54.5	53.5	52.5	51.3	49.5	-50.5
-1	Rho	334.5	303.3	289.2	284.7	287.5	299.6	330.0	301.8
	Theta	66.2	77.9	87.8	96.8	106.0	116.0	128.2	113.5
	Phi	56.2	54.7	53.6	52.6	51.6	50.4	48.6	-49.7
0	Rho	336.1	304.9	290.9	286.3	289.0	301.0	331.2	303.2
	Theta	66.2	77.8	87.7	96.7	105.8	115.8	127.9	113.3
	Phi	55.8	54.2	53.2	52.2	51.2	50.0	48.2	-49.3
1	Rho	337.6	306.6	292.5	287.8	290.5	302.3	332.3	304.7
	Theta	66.2	77.8	87.6	96.6	105.7	115.6	127.7	113.1
	Phi	55.4	53.8	52.8	51.8	50.8	49.6	47.8	-48.8
3	Rho	340.8	309.9	295.8	291.0	293.4	305.0	334.5	307.5
	Theta	66.3	77.7	87.4	96.3	105.3	115.1	127.1	112.6
	Phi	54.6	53.0	51.9	51.0	50.0	48.7	46.9	-48.0
5	Rho	344.2	313.3	299.1	294.2	296.4	307.6	336.6	310.3
	Theta	66.3	77.6	87.2	96.0	104.9	114.7	126.6	112.2
	Phi	53.8	52.2	51.1	50.2	49.1	47.9	46.1	-47.3
7	Rho	347.6	316.7	302.5	297.4	299.4	310.2	338.7	313.0

AoA (deg)	Coordinate	Mic1	Mic2	Mic3	Mic4	Mic5	Mic6	Mic7	Array
	Theta	66.3	77.5	87.0	95.6	104.4	114.1	126.0	111.7
	Phi	53.1	51.5	50.4	49.4	48.4	47.1	45.3	-46.5
10	Rho	352.9	322.0	307.6	302.2	303.8	314.1	341.7	317.1
	Theta	66.2	77.3	86.6	95.1	103.7	113.3	125.1	110.9
	Phi	52.0	50.4	49.3	48.3	47.2	46.0	44.2	-45.4
12	Rho	356.6	325.6	311.0	305.4	306.7	316.6	343.6	319.8
	Theta	66.1	77.1	86.3	94.7	103.2	112.8	124.5	110.4
	Phi	51.3	49.7	48.6	47.6	46.5	45.3	43.5	-44.7
15	Rho	362.2	331.1	316.2	310.3	311.1	320.3	346.3	323.8
	Theta	66.0	76.7	85.7	94.0	102.4	111.9	123.6	109.5
	Phi	50.3	48.7	47.5	46.5	45.5	44.3	42.4	-43.7
17	Rho	366.0	334.8	319.7	313.5	313.9	322.7	348.1	326.3
	Theta	65.8	76.5	85.4	93.5	101.9	111.2	122.9	108.9
	Phi	49.6	48.0	46.9	45.9	44.9	43.6	41.8	-43.1
20	Rho	371.8	340.4	325.0	318.3	318.2	326.3	350.6	330.1
	Theta	65.6	76.0	84.8	92.8	101.0	110.3	121.9	108.0
	Phi	48.7	47.1	46.0	45.0	43.9	42.7	40.9	-42.2
22	Rho	375.8	344.2	328.5	321.5	321.0	328.5	352.2	332.6
	Theta	65.4	75.7	84.3	92.3	100.4	109.6	121.3	107.3
	Phi	48.1	46.5	45.4	44.4	43.3	42.1	40.3	-41.7
25	Rho	381.8	349.9	333.7	326.3	325.2	331.9	354.4	336.2
	Theta	65.1	75.2	83.7	91.5	99.5	108.6	120.2	106.4
	Phi	47.3	45.7	44.5	43.5	42.5	41.3	39.5	-40.9

Table 4. Sensor locations relative to acoustic center for 5º sideslip. Rho is inches and theta and phi are in degrees.

AoA (deg)	Coordinate	Mic1	Mic2	Mic3	Mic4	Mic5	Mic6	Mic7	Array
-5	Rho	326.4	294.8	280.7	276.4	279.6	292.5	324.0	298.2
	Theta	65.9	77.8	88.1	97.4	106.8	117.1	129.4	114.2
	Phi	57.7	56.1	55.0	54.1	53.1	51.9	50.1	-51.8
-3	Rho	329.3	297.9	283.9	279.5	282.6	295.3	326.4	301.0
	Theta	66.0	77.9	88.0	97.2	106.6	116.7	128.9	113.8
	Phi	56.8	55.2	54.2	53.2	52.2	51.0	49.1	-50.9
-1	Rho	332.3	301.1	287.1	282.7	285.7	298.0	328.8	303.8
	Theta	66.1	77.9	87.9	97.0	106.2	116.3	128.4	113.4
	Phi	56.0	54.4	53.3	52.3	51.3	50.1	48.2	-50.0
0	Rho	333.9	302.8	288.8	284.3	287.2	299.4	330.0	305.2
	Theta	66.1	77.9	87.8	96.9	106.0	116.1	128.2	113.2
	Phi	55.6	54.0	52.9	51.9	50.9	49.6	47.8	-49.6
1	Rho	335.5	304.5	290.4	285.9	288.7	300.8	331.1	306.6
	Theta	66.2	77.8	87.7	96.7	105.9	115.9	127.9	113.0

AoA (deg)	Coordinate	Mic1	Mic2	Mic3	Mic4	Mic5	Mic6	Mic7	Array
	Phi	55.2	53.5	52.5	51.5	50.5	49.2	47.4	-49.2
3	Rho	338.8	307.9	293.8	289.2	291.8	303.5	333.4	309.4
	Theta	66.2	77.8	87.5	96.4	105.5	115.4	127.4	112.6
	Phi	54.4	52.7	51.6	50.7	49.6	48.4	46.6	-48.4
5	Rho	342.2	311.4	297.3	292.5	294.8	306.3	335.6	312.1
	Theta	66.2	77.7	87.3	96.1	105.1	114.9	126.8	112.1
	Phi	53.6	52.0	50.9	49.9	48.8	47.6	45.8	-47.6
7	Rho	345.8	314.9	300.7	295.8	297.9	309.0	337.7	314.7
	Theta	66.2	77.5	87.1	95.8	104.6	114.3	126.3	111.7
	Phi	52.8	51.2	50.1	49.1	48.1	46.8	45.0	-46.8
10	Rho	351.3	320.4	306.0	300.8	302.5	313.0	340.9	318.6
	Theta	66.2	77.3	86.7	95.2	103.9	113.5	125.4	110.9
	Phi	51.8	50.1	49.0	48.0	47.0	45.7	43.9	-45.7
12	Rho	355.0	324.2	309.6	304.2	305.6	315.6	342.9	321.2
	Theta	66.1	77.1	86.3	94.8	103.4	112.9	124.7	110.4
	Phi	51.1	49.5	48.3	47.3	46.3	45.0	43.2	-45.0
15	Rho	360.9	329.9	315.0	309.2	310.1	319.5	345.8	324.9
	Theta	66.0	76.8	85.8	94.1	102.6	112.0	123.8	109.5
	Phi	50.1	48.5	47.4	46.3	45.3	44.1	42.2	-44.0
17	Rho	364.8	333.7	318.7	312.6	313.1	322.1	347.7	327.4
	Theta	65.8	76.5	85.5	93.6	102.0	111.4	123.1	108.9
	Phi	49.5	47.8	46.7	45.7	44.7	43.4	41.6	-43.3
20	Rho	370.9	339.6	324.2	317.6	317.6	325.8	350.3	331.0
	Theta	65.6	76.1	84.9	92.9	101.2	110.4	122.1	108.0
	Phi	48.6	47.0	45.8	44.8	43.8	42.6	40.7	-42.4
22	Rho	375.0	343.5	327.9	321.0	320.6	328.3	352.0	333.3
	Theta	65.4	75.8	84.4	92.4	100.5	109.8	121.4	107.4
	Phi	48.0	46.4	45.3	44.3	43.2	42.0	40.2	-41.8
25	Rho	381.3	349.4	333.4	326.0	325.0	331.9	354.5	336.6
	Theta	65.2	75.3	83.8	91.6	99.6	108.7	120.3	106.5
	Phi	47.2	45.6	44.5	43.5	42.5	41.2	39.4	-40.9

Table 5. Sensor locations relative to acoustic center for 10º sideslip. Rho is inches and theta and phi are in degrees.

AoA (deg)	Coordinate	Mic1	Mic2	Mic3	Mic4	Mic5	Mic6	Mic7	Array
-5	Rho	324.1	292.5	278.4	274.2	277.6	290.7	322.6	300.3
	Theta	65.7	77.8	88.1	97.5	107.0	117.4	129.7	114.0
	Phi	57.4	55.8	54.7	53.7	52.7	51.5	49.7	-52.1
-3	Rho	327.1	295.7	281.7	277.4	280.7	293.5	325.0	303.1
	Theta	65.9	77.8	88.0	97.3	106.7	117.0	129.2	113.7
	Phi	56.5	54.9	53.8	52.9	51.8	50.6	48.7	-51.2

AoA (deg)	Coordinate	Mic1	Mic2	Mic3	Mic4	Mic5	Mic6	Mic7	Array
-1	Rho	330.2	299.0	285.0	280.7	283.8	296.3	327.4	305.8
	Theta	66.0	77.8	87.9	97.1	106.4	116.5	128.7	113.3
	Phi	55.7	54.1	53.0	52.0	51.0	49.7	47.8	-50.4
0	Rho	331.8	300.7	286.7	282.3	285.3	297.8	328.6	307.2
	Theta	66.0	77.8	87.8	97.0	106.2	116.3	128.4	113.1
	Phi	55.3	53.7	52.6	51.6	50.5	49.3	47.4	-49.9
1	Rho	333.5	302.4	288.4	284.0	286.9	299.2	329.8	308.5
	Theta	66.1	77.8	87.8	96.8	106.0	116.1	128.2	112.9
	Phi	54.9	53.2	52.1	51.2	50.1	48.9	47.0	-49.5
3	Rho	336.9	305.9	291.9	287.3	290.1	302.0	332.1	311.2
	Theta	66.1	77.7	87.6	96.5	105.6	115.6	127.6	112.5
	Phi	54.1	52.5	51.3	50.3	49.3	48.0	46.2	-48.7
5	Rho	340.4	309.5	295.4	290.7	293.2	304.8	334.4	313.8
	Theta	66.2	77.6	87.4	96.2	105.2	115.1	127.1	112.1
	Phi	53.3	51.7	50.6	49.6	48.5	47.3	45.4	-47.9
7	Rho	344.0	313.2	299.0	294.1	296.4	307.6	336.7	316.4
	Theta	66.2	77.5	87.1	95.9	104.7	114.5	126.5	111.6
	Phi	52.6	51.0	49.8	48.8	47.8	46.5	44.6	-47.1
10	Rho	349.7	318.8	304.5	299.3	301.2	311.8	339.9	320.1
	Theta	66.1	77.3	86.7	95.3	104.0	113.7	125.5	110.9
	Phi	51.5	49.9	48.8	47.8	46.7	45.4	43.6	-46.0
12	Rho	353.6	322.7	308.2	302.8	304.3	314.6	342.1	322.6
	Theta	66.1	77.1	86.4	94.9	103.5	113.1	124.9	110.4
	Phi	50.9	49.2	48.1	47.1	46.0	44.8	42.9	-45.2
15	Rho	359.6	328.6	313.9	308.1	309.1	318.6	345.1	326.1
	Theta	66.0	76.8	85.9	94.2	102.7	112.2	123.9	109.5
	Phi	49.9	48.3	47.2	46.1	45.1	43.8	42.0	-44.2
17	Rho	363.7	332.6	317.7	311.6	312.3	321.3	347.1	328.4
	Theta	65.8	76.5	85.5	93.7	102.1	111.5	123.2	109.0
	Phi	49.3	47.7	46.6	45.5	44.5	43.2	41.4	-43.5
20	Rho	370.0	338.7	323.4	316.9	317.0	325.3	350.0	331.8
	Theta	65.6	76.1	84.9	93.0	101.3	110.5	122.2	108.1
	Phi	48.5	46.8	45.7	44.7	43.7	42.4	40.6	-42.5
22	Rho	374.3	342.8	327.2	320.4	320.1	327.9	351.9	333.9
	Theta	65.5	75.8	84.5	92.5	100.7	109.9	121.5	107.5
	Phi	47.9	46.3	45.2	44.2	43.1	41.9	40.1	-41.9
25	Rho	380.8	349.0	333.0	325.7	324.8	331.8	354.5	337.1
	Theta	65.2	75.4	83.9	91.7	99.7	108.8	120.4	106.5
	Phi	47.2	45.6	44.4	43.4	42.4	41.2	39.4	-41.0

Appendix B

All run and sequence numbers are referenced to the acoustic test matrix and not the NFAC run and sequence numbers. Steady state NFAC condition files have been updated to reflect acoustic numbering and also truncated to include only acoustic points.

There are nominally 6 files for each data point and 1 for each run; all are text files. '*R*', is used for indicate run number and '*S*' is used to indicate sequence number.

1: CESTOL*R*_NFACsteady.tab: Steady state file from the NFAC. Recorded by NFAC data system roughly simultaneously with the acoustic data. The most comprehensive file for tunnel conditions and model parameters. All sequences within a run are included in one file.

2: CESTOL*R*p*S*_CB_BNS*R*p*S*_NB.csv: Narrowband array data with peak beamforming levels after background noise subtraction. Note that the background noise point used for subtraction is included in the naming convention.

3: CESTOL*R*p*S*_CB_BNS*R*p*S*_NB_corrections.csv: Corrections added to the array peak levels. The header information includes the propagation distance and convection angles used for the corrections. Frequency dependent corrections include: atmospheric corrections, Kevlar corrections, freefield microphone response in a plate, and a 6 dB pressure doubling.

4: CESTOL*R*p*S*_CB_BNS*R*p*S*_NB_correctedData.csv: Peak array data with corrections added. Format is the same as the uncorrected data file.

5: CESTOL*R*p*S*_narrow.txt: Narrowband data from the 7 freefield microphones and 8 surface mounted Kulites. Each channel is listed by column.

6: CESTOL*R*p*S*_narrow_corrections.txt: Corrections applied to the single microphone data. Header information includes the propagation distance and convection angle for each microphone for a given point. Corrections for atmospheric attenuation and nosecone response are included.

7: CESTOL*R*p*S*_narrow_correctedData.txt: Narrowband data with corrections added. Note that unsteady surface pressure data is not included in the corrected data file.